

Changes in Retinal Mitochondrial Function in Ocular Diseases and a Potential Treatment
Using Near-Infrared Light

by

Woo Hyun Han

A thesis submitted in partial fulfillment of the requirements for the degree of

Master of Science

Medical Sciences – Ophthalmology and Visual Sciences
University of Alberta

© Woo Hyun Han, 2018

ABSTRACT

Mitochondria are both prominent target and source of reactive oxygen species (ROS). Their role in a wide range of diseases has been gaining a substantial amount of interest, including a number of high-profile ocular diseases. In the present thesis, we investigated the mitochondrial functional changes in animal models of Diabetic Retinopathy (DR) and Stargardt-like Disease (STGD3). Subsequently, we examined a non-invasive therapy, photobiomodulation (PBM), which uses near-infrared light to reportedly increase mitochondrial complex IV (CIV) function and produce positive therapeutic effects.

We demonstrate that the OROBOROS Oxygraph-2k high-resolution respirometer can be successfully utilized to study the ocular mitochondrial function in rodent models. Furthermore, we report an early change in retinal mitochondria function in Nile grass rat model of DR; in 2mo – almost a full year before any vascular or functional changes and 4mo before the development of systemic hyperglycemia – the retinal mitochondria showed diminished outer membrane integrity and upregulated NADH-pathway respiration. In contrast, the RPE mitochondria studied in ELOVL4 transgenic model of C57 mice showed preserved mitochondrial function until 10mo after the onset of photoreceptor cell death. These results suggest that in DR, the retinal mitochondria likely play causal role whereas in STGD3, they take the role of a target.

Lastly, we report decreased CIV function and increased chemical background respiration in response to a single application of 670nm light. To explain our result, we propose a model of PBM's mechanisms involving increased nitric oxide release, increased CIV inhibitor resistance, and decreased non-mitochondrial oxygen consumption. In light of this preliminary data, we present a rationale for possible application of PBM in the treatment of DR and STGD3.

PREFACE

This thesis is an original work by Ted (Woo Hyun) Han. The research project on which this thesis is based received ethics approval from the University of Alberta Research Ethics Board, AUP#00000328, January 2016.

Chapter 3 of this thesis has been published as Han, W. H., Gotzmann, J., Kuny, S., Huang, H., Chan, C. B., Lemieux, H., & Sauvé, Y. (2017). Modifications in Retinal Mitochondrial Respiration Precede Type 2 Diabetes and Protracted Microvascular Retinopathy. *Investigative Ophthalmology & Visual Science*, 58(10), 3826¹. The research here was part of collaboration with C. Chan, Department of Physiology, University of Alberta. I was responsible for tissue collection, animal care, establishing experimental protocol, equipment maintenance, performing experiments and data analysis of mitochondrial functional studies. Figure 3.1, 3.2, and 3.3 and table 1 and 2 were generated with the data I collected. Figure 3.4, 3.5, 3.6, 3.7, and 3.8 were generated with data Gotzmann, J. collected. I also contributed to the manuscript composition with assistance from J. Kuny and Y. Sauve.

Chapter 4 of this thesis has been published as Dejos, C., Kuny, S., Han, W. H., Capel, H., Lemieux, H., & Sauvé, Y. (2018). Photoreceptor-induced RPE phagolysosomal maturation defects in Stargardt-like Maculopathy (STGD3). *Scientific Reports*, 8(1), 5944². I was responsible for tissue collection, data collection and analysis for respirometer and secondary experiments. Figure 4.4 was generated with data I collected. Figure 4.6 was generated

ACKNOWLEDGEMENT

For Dr. Yves Sauve, the kind guidance, inspiration, and mentoring in not just the research but in wide aspects of life.

For Dr. Helene Lemieux, the guidance through the wonderful world of mitochondria science.

For Sharee Kuny and Jill Schneider, day to day support in the lab.

For Hui Huang, Rachel Bryant, Julia Lawler, and Sara Kluthe for helping with animal handling.

And for Zhining Zhu, for maintenance of animal colony.

CONTENTS

Abstract.....	ii
Preface.....	iii
Acknowledgement	iv
List of Tables	x
List of Figures.....	xi
1 Background.....	1
1.1 Mitochondrial Physiology.....	1
1.1.1 Oxidative Phosphorylation (OXPHOS).....	1
1.1.2 Oxidative Stress and Mitochondria	3
1.1.3 Mitochondrial Functional Study.....	5
1.1.4 Mitochondrial Respiration States	7
1.2 Retina Metabolism and Mitochondria	8
1.3 Mitochondrial Involvement of Retinal Diseases.....	11
1.3.1 Primary Mitochondrial Disorders.....	11
1.3.2 Diabetic Retinopathy.....	12
1.3.3 Nile Rat Model of T2DM and Diabetic Retinopathy	15
1.3.4 Stargardt-Like Macular Degeneration and Transgenic Mice Model.....	18
1.4 Photobiomodulation as Mitochondria Targeting Therapy of Ocular Diseases.....	20
1.4.1 Overview of Mitochondria Targeting Therapies	20
1.4.2 Photobiomodulation.....	22

1.4.3	PBM in Treatment of Ocular Diseases	24
2	Experimental Rationale.....	29
2.1	Overview.....	29
2.2	Hypothesis.....	29
2.3	Aims.....	30
3	Modifications in Retinal Mitochondrial Respiration Precede Type 2 Diabetes and Protracted Microvascular Retinopathy.....	31
3.1.1	Introduction	31
3.2	Methods.....	34
3.2.1	Animals and Diets	34
3.2.2	Fasting blood glucose, glycated hemoglobin and plasma insulin	34
3.2.3	Funduscopy.....	35
3.2.4	Trypsin digestion of retinal vasculature	36
3.2.5	Immunohistochemistry	37
3.2.6	ERG recordings	39
3.2.7	High-resolution respirometry	40
3.3	Results.....	44
3.3.1	Changes in retinal mitochondrial respiration precede T2D.....	44
3.3.2	Type 2 diabetes.....	47
3.3.3	Early diabetic retinopathy.....	48
3.3.4	Cataracts of increasing severity.....	55

3.4	Discussion	55
3.5	Conclusion	62
4	Photoreceptor-induced RPE Phagolysosomal Maturation Defects in Stargardt-like Maculopathy	64
4.1	Introduction.....	64
4.2	Methods.....	66
4.2.1	Animals.....	66
4.2.2	Cell culture	66
4.2.3	Isolation of photoreceptor outer segments.....	67
4.2.4	Phagocytosis assay	68
4.2.5	Live imaging of LysoTracker-labelled phagolysosomes.....	69
4.2.6	Nuclear and cytoplasmic TFEB localization by western blotting.	69
4.2.7	RPE flatmounts and immunohistochemistry	71
4.2.8	cDNA synthesis and quantitative RT-PCR.	71
4.2.9	RPE cell protein preparation and western blotting.....	72
4.2.10	Mass spectrometry.....	73
4.2.11	High-resolution respirometry	75
4.3	Results.....	77
4.3.1	Processing of POS isolated from TG mice is delayed <i>in vitro</i>	77
4.3.2	Acidified phagolysosome maturation is impaired.	79
4.3.3	Preserved activation of autophagy-lysosomal pathway components	80

4.3.4	Members of the crystallin protein family are upregulated in RPE.	82
4.3.5	RPE cells conserve their mitochondrial respiration capacity and show no sign of oxidative stress.	85
4.3.6	Microglia/macrophages infiltrate the subretinal space.	90
4.4	Discussion.....	91
5	CIV Effect of Photobiomodulation.....	96
5.1	Intro.....	96
5.2	Methods.....	98
5.2.1	Cell Culture.....	98
5.2.2	NIR light Exposure.....	99
5.2.3	Mitochondrial Functional Assessment with O2k	100
5.3	Results.....	102
5.3.1	Intermittent changes in ROUTINE Respiration	102
5.3.2	NIR Light exposure did not increase CIV activity	102
5.3.3	PBM increased chemical background	104
5.4	Discussion.....	106
5.5	Conclusion	112
6	Discussion.....	114
6.1	Viability of Respirometer for Ocular Tissues.....	114
6.2	Tissue-Specific Mitochondrial Responses.....	117
6.3	Mitochondrial Involvement in Ocular Diseases	120
6.4	Commenting on the Efficacy of PBM	123
7	Conclusion	127

7.1	Significance.....	127
7.2	Limitations	128
7.3	Future Directions	129
8	Supporting Information.....	131
8.1	Additional Nile Rat Mitochondrial Data.....	131
8.2	Additional ELOVL4 Mice Mitochondrial Data.....	132
	References.....	134

LIST OF TABLES

Table 1.1 Summaries of Photobiomodulation Studies in Ocular Context	26-7
Table 3.1 Retinal Mitochondrial Function Expressed in Flux Per Mass	45
Table 3.2 Metabolic Phenotype of Nile Rat	47
Table 3.3 Central and Peripheral Retina Outer And Inner Nuclear Layer Thickness Measures And Chat-Immunoreactive Amacrine Cell Counts	51
Table 4.1 Variation in Protein Levels in Transgenic Eyecups At One Month.	86-7
Table 5.1 Light Characteristics of Near Infrared Light	98

LIST OF FIGURES

Figure 1.1 A Simplified Schema of Mitochondrial Electron Transport System and Oxidative Phosphorylation Process.	2
Figure 1.2 Regions of High Mitochondrial Concentration as Reported By Stone Et Al. ⁴¹	10
Figure 1.3 Nile Rats Phenotypes During Type 2 Diabetes Mellitus Progression.	16
Figure 3.1 Representative Trace of High-Resolution Respirometry Using A Multiple Substrate-Inhibitor-Titration Protocol in Retinas from A Single Nile Rat.	41
Figure 3.2 Mitochondrial Oxidative Phosphorylation Capacity and Mitochondrial Content In Retina Homogenates.	44
Figure 3.3 Indicators of Coupling and Mitochondrial Outer Membrane Integrity.	46
Figure 3.4 Retinal Digest Preparations of Diabetic and Control Nile Rat Retinas.	49
Figure 3.5 Oscillatory Potential Timing At 18 Months, Expressed as A Function Of Stimulus (Flash) Strength.	50
Figure 3.6 Cross Sections Of Central Retina, Immunostained For Cholinergic Amacrine Cells (Chat) In Red With DAPI-Stained Nuclei In Blue.	52
Figure 3.7 Retinal Flatmounts Of Blood Vessels (2 Months, Top; 12 Months, Bottom) Stained For Oxidative (4-Hydroxynonenal) And Nitrative (Nitrotyrosine) Stress In Green.	53
Figure 3.8 Example of Cataractogenesis in 18-Month Hyperglycemic Nile Rats.	54
Figure 3.9 Timeline of Events as A Function Of Age And Type 2 Diabetes And Associated Retinopathy Progression In Nile Rats.	57
Figure 4.1 Degradation of Transgenic Photoreceptor Outer Segment Is Delayed. Numbers Of Phagolysosomes Are Reduced.	77
Figure 4.2 Autophagy-Lysosomal Pathway Genes and Proteins Have Normal Expression Levels.	80
Figure 4.3 Crystallin Genes and Proteins Are Differentially Expressed.	83
Figure 4.4 Mitochondrial Oxidative Phosphorylation and Mitochondrial Content Are Preserved.	88
Figure 4.5 Microglia/Macrophages Infiltrate the Subretinal Space.	90
Figure 4.6 Summary of Events Occurring Prior To Photoreceptor Death.	92
Figure 5.1 Changes in Complex IV Single Step Respiration In Response To Near Infrared Light Exposure.	102
Figure 5.2 Changes in Chemical Background In Response To Near Infrared Light Exposure. Sodium Azide (Azd) Titration Was Carried Out After Titration Of TMPD.	104
Figure 5.3 Proposed Break-Down Of TMPD-Induced Respiration.	109

Figure 5.4 Proposed Mechanism of Photobiomodulation's Effect on Mitochondria.	111
Figure 6.1 A Simplified Schema of Mitochondrial Role in Non-Primary Mitochondrial Diseases.	121
Figure 8.1 Mitochondrial Oxidative Phosphorylation Capacity, Mitochondrial Content, And Indicators of Coupling and Mitochondrial Outer Membrane Integrity in Retinal Pigment Epithelium Homogenates.	129
Figure 8.2 Mitochondrial Oxidative Phosphorylation and Mitochondrial Content In 1mo Retina, And 12mo Retina and Retinal Pigment Epithelium.	130

1 BACKGROUND

1.1 MITOCHONDRIAL PHYSIOLOGY

1.1.1 Oxidative Phosphorylation (OXPHOS)

Mitochondria are double membrane-bound organelles that serve essential roles in eukaryotic cellular physiology. They are an important part of apoptosis pathway³, redox signaling⁴, production of heme groups^{5,6} and steroid hormones⁷, calcium homeostasis⁸, and are involved in a number of bioenergetics pathways⁹ such as Krebs cycle, ketogenesis, and gluconeogenesis¹⁰. However, as the canonical *powerhouse of the cell*, they are most well known for their respiration complexes that allow efficient utilization of nutrients to produce ATP (adenosine triphosphate), the currency of cellular energy.

Mitochondria employ multiple redox centers arranged as electron transport system (ETS) that performs step-wise transfer of electrons from electron sources to the final electron acceptor, molecular oxygen. Redox centers are held by multi-protein complexes: respiratory complex I (CI, NADH dehydrogenase), II (CII, succinate dehydrogenase), III (CIII, coenzyme Q : cytochrome *c* – oxidoreductase), and IV (CIV, cytochrome *c* oxidase). Of note, the ETS is commonly referred to as electron transport chain, but the term *system* is more accurate as electron transport is not a linear process. How the respiratory complexes are organized in mitochondria is still not completely understood. A historically prevailing fluid-state model theory explains that the individual complexes move laterally in the inner mitochondrial membrane and step-wise transfer electrons occur when two complexes collide¹¹. Newer data support solid-state model where the complexes exist in a supercomplex called respirasome¹².

Both carbohydrate and lipids can be used as sources of electrons for mitochondrial ETS. Electrons may enter ETS through number of different paths. For example, NADH enters the ETS through CI, succinate through CII, flavin adenine dinucleotide (FADH₂) through electron transferring flavoprotein complex (CETF), and glycerophosphate (Gp) through glycerophosphate dehydrogenase complex (CGpDH). After entering the ETS, the electrons converge at the Q-junction and proceed linearly to CIII and then to CIV via cytochrome *c*, a mobile electron carrier loosely associated with the outer side of the inner mitochondrial membrane. At CIV, the final site of ETS, an oxygen molecule is reduced to water.

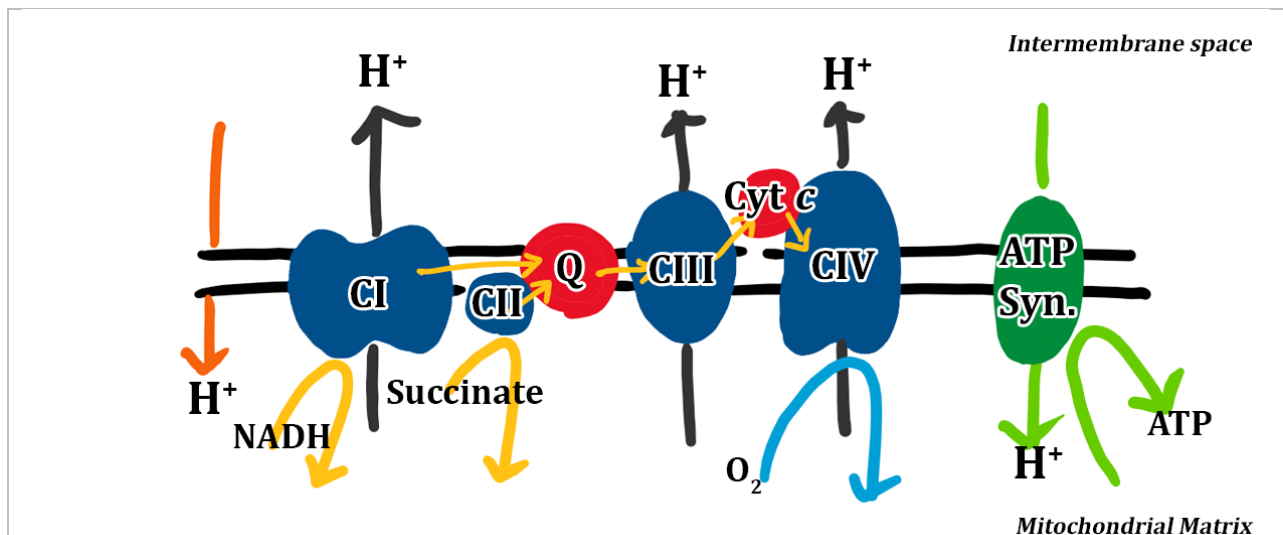


Figure 1.1 A simplified Schema of Mitochondrial ETS and OXPHOS process. Electrons entering the ETS from CI and CII converge on Q junction, and then proceed linearly to next destinations. CI, CIII, and CIV displaces proton to intermembrane space, creating a proton gradient. This gradient is used by ATP synthase for phosphorylation of ATP. There is inherent leak of proton back into mitochondrial matrix, which accounts for LEAK respiration (orange).

The energy given off by electrons moving through the CI, CIII, and CIV power the proton pumping activities from the mitochondrial matrix into intermembrane space (summarized in *Fig 1*) against its chemical concentration gradient. This movement generates the proton motive force

(PMF) consisting of electrical membrane potential ($\Delta\Psi$) and the pH gradient (pH), with $\Delta\Psi$ contributing the majority of PMF in physiological condition. In order to generate ATP, PMF is utilized mainly by the phosphorylation system, which is composed of an adenine nucleotide translocator, a phosphate carrier, and complex V (CV, ATP synthase). PMF is also used by mitochondrial ion and substrate transport. The process of PMF generation by ETS and its utilization by CV for ATP synthesis are collectively known as oxidative phosphorylation (OXPHOS). The term *coupling* refers to how much ETS and phosphorylation system varies between organism/tissue/cell and impacts heat generation and redox regulation^{9,13}.

1.1.2 Oxidative Stress and Mitochondria

ROS are highly reactive oxygen-derived oxidants that include non-radicals as well as unstable free radical species that by definition have unpaired valence electrons. Prominent biological ROS include superoxide ($O_2^{\cdot-}$), hydrogen peroxide (H_2O_2), and hydroxyl radical (OH^{\cdot})¹⁴. ROS can oxidize lipids, nucleic acids, and proteins, disturbing normal cell functions and even causing cell death. They are produced from a multitude of cellular sources including mitochondria, peroxisome, endoplasmic reticulum, cytosolic enzymes such as nitric oxide synthase, lipoxygenase, and prostaglandin-endoperoxide synthase¹⁵.

The interest in mitochondria as a research and clinical targets have increased considerably in past years. Diverse topics such as diabetes¹⁶, diabetes-induced complications¹⁷, neurodegenerative diseases such as Parkinson's¹⁸ and Alzheimer's¹⁹ as well as aging²⁰. This is in part due to a recent focus on metabolism as a central figure in both physiology and pathophysiology, but many of studies also often focus on mitochondrial generation of reactive ROS and their contribution to overall disease mechanism.

In mitochondria, electrons pass through the ETS redox centers as a single electron – that is, redox centers essentially act as free radicals. Inevitably, redox centers participate in side-reactions with molecular oxygen and produce ROS^{13,21}. This inherent production of ROS from CI and CIII during mitochondrial respiration are detected in experimental setting²². More recently, CII also inherently produces ROS during regular respiration²³. Furthermore, if the flow of electrons in ETS is disturbed by a pharmacological inhibition of CIII or by abnormally high mitochondrial membrane potential (that makes the displacement of proton difficult), the electrons at Q-junction will travel back into CI and CII in a condition known as *reverse electron flow* which greatly enhances ROS production²¹.

Despite the frequent mentions of mitochondria as the principal source of oxidative stress in various disease conditions, the production of ROS is not significant under physiological conditions and the emission of ROS from mitochondria is much smaller than their production²⁴. This is explained by the extensive set of antioxidative defense mechanism in play both at mitochondrial and cytosolic locations. Examples of antioxidative enzymes include superoxide dismutase (SOD), catalase, and glutathione peroxidase, and there are non-enzymatic antioxidants such as vitamin A (ascorbic acid), vitamin E (α -tocopherol) and glutathione. It is when the antioxidant systems are overwhelmed, due to increased ROS production and/or decreased antioxidative capacity, the cells experience oxidative stress.

Mitochondria are a particularly interesting figure in the discussions of oxidative stress as they are both a prominent source and a target of ROS²⁵. The bidirectional links between oxidative damage to mitochondria and the mitochondrial ROS production are not well understood^{26,27}. However, a *vicious cycle* (positive feedback loop) is reported where mitochondrial dysfunction

increases ROS production from mitochondria, which then causes further mitochondrial dysfunction (the initiating factor could be non-mitochondrial ROS that causes the dysfunction, and so on). Mitochondrial DNA (mtDNA) is especially susceptible to oxidative damage for (1) its proximity to the oxidative machinery that generates ROS, (2) its lack of histones that provide protection²⁸, and (3) its low capacity of DNA repair machinery in mitochondria^{28,29}. The mtDNA encodes many subunits of the respiratory complexes; therefore, mtDNA damage can adversely affect the performance of respiratory complexes. CIII function is reduced under mtDNA damage³⁰ and this may lead to reverse electron flow and subsequent increase in ROS production. Another example is aconitase, a mitochondrial enzyme that is involved in Krebs cycle, who shows augmented ROS production when exposed to ROS³¹.

1.1.3 Mitochondrial Functional Study

Given the multiple roles that mitochondria play in eukaryotic biology, the terms could also apply to a wide range of events. In this thesis, the terms mitochondrial function and dysfunction refer to mitochondrial production of ATP through OXPHOS and related changes.

Mitochondria function can be assessed in multiple different ways. For example, functions of immunocaptured respiratory complexes can be assessed with dye-metabolites and spectrophotometer^{32,33}. Luminance based ATP-content measurement can serve as a marker of mitochondrial marker. $\Delta\Psi$ may be used as a marker of mitochondrial function; fluorescent probes such as safranin or cation-specific electrodes such as tetraphenylphosphonium-specific electrodes are used for this purpose³⁴. Another popular approach of functional assessment involves measurement of oxygen consumption rate, which corresponds well to the CIV activity. Conventionally, this is done with oxygen-sensing electrodes but phosphorescent oxygen-probe

and an optical sensor, such as Seahorse Bioscience XF Extracellular Flux Analyzer (Agilent Technologies, California, United States) can also be used to measure oxygen concentration without involving polarographic electrodes. Clinically, noninvasive measurement of *in vivo* oxygen tension can be assessed with the investigation of oxygenation status of hemoglobin and myoglobin with near-infrared spectroscopy³⁵, though recent findings suggest NIR may interfere with the mitochondrial function itself (see **Chapter 1.4.2**).

The Clark-type electrode is a type of oxygen-sensing electrode setup designed specifically for measurement from biological samples. In Clark-type electrode setup, a platinum or gold cathode and silver/silver chloride anode electrodes immersed in electrolytic solution are placed in a chamber separated from mitochondrial preparation by a selectively permeable membrane³⁴. This membrane allows movement of ions and molecules such as oxygen across it but prevents bigger biomolecule such as proteins from contaminating the electrode surface. When voltage is applied through electrodes, the cathode becomes reduced and it reduces oxygen to H₂O₂. The generated current is then stoichiometrically proportional to oxygen available in sample.

Oxygraph-2K High-Resolution Respirometer (O2k), developed by Oroboros Instruments (Innsbruck, Austria), is an advanced Clark-type electrode that addresses many of its shortcomings. In addition to using electrodes with high temporal and spatial resolution, the materials for experimental chambers are explicitly chosen to be chemically inert and have minimal oxygen back-diffusion (diffusion of oxygen from materials into mitochondrial preparation; Teflon, which is a common material for stirrer and membrane of classical Clark-type electrodes are especially prone to this artifact). O2k is also equipped with a Peltier controller that maintains the desired temperature with 0.001 °C precision. Temperature have a

huge impact on mitochondrial function³⁶. In addition to these hardware quality control, software calibration further corrects for the inherent oxygen consumption by the electrode (instrumental background correction) and back-diffusion of oxygen (zero oxygen calibration).

Also, O2k's chambers have a large volume to support longer titration protocols without oxygen depletion compared to alternatives such as phosphorescent probe-based XF analyzer or conventional Clark-type electrodes. These multiple titration steps allow O2k to express the respiration data in the internally normalized unit of flux control ratio (FCR); allowing an examination of data without influences from the chamber's mitochondria content (influenced by number, size, etc...).

1.1.4 Mitochondrial Respiration States

Meaningful interpretation and comparison of mitochondrial functional data across different experiments require adequate terminologies that capture nuances of non-physiological experimental environment that mitochondria are subjected to. Mitochondrial respiration states can be defined by two parameters – the “coupling control state” and the “substrate control states” – reflecting the substrate and/or inhibitor condition mitochondria are subjected³⁷.

The coupling control states describe the respiration rate of mitochondria in an environment with defined fuel substrates and inhibitor combination corresponding to various degree of coupling between ETS and phosphorylation system. (1) OXPHOS-state describes respiration of mitochondria in saturating-level of ADP present where the phosphorylation system is coupled to the ETS. (2) ETS-state describes noncoupled respiration state with uncoupler agents that artificially remove the proton gradient across inner mitochondrial membrane. Comparison between OXPHOS- and ETS-states can reveal whether phosphorylation system is exerting any

limits on ETS. Mitochondria can be presented with different substrates and inhibitors. (3) The LEAK-respiration reflects compensatory O₂ consumption by ETS for intrinsic leak and slip of protons from intermembrane space of mitochondria to mitochondrial matrix³⁸. LEAK can be measured by inhibiting phosphorylation system or in absence of ADP. Finally, (4) ROUTINE-state respiration does not have explicitly defined substrates and describes the respiration of supported by substrates present in cell growth media (thus, this cannot be measured in permeabilized cells or isolated mitochondria).

In addition to these control states, the residual oxygen consumption (ROX) describes the non-ETS oxygen consumption in the mitochondrial preparation. This is measured after inhibition of ETS and represents oxidative reactions by catalases, peroxidases, monoamine oxidases, monooxygenases, dioxygenase, hydroxylase, NAD(P)H oxidase³⁹ and side-reactions of oxygen that produces ROS⁴⁰.

The substrate control states further describe mitochondrial respiration based on the ETS components that are contributing to the overall respiration at a given time. Substrate available for mitochondria may be powering NADH-, succinate-, or NADH and succinate- electron transfer pathway state (N-, S-, NSuccinate-pathway), respectively corresponding to CI, CII, and CI&II activities.

1.2 RETINA METABOLISM AND MITOCHONDRIA

Numerous tissues of the eyes are highly energetically active. For instance, the extraocular muscles execute fast and almost constant movements, the corneal endothelial pumps need to

maintain optimal fluid level⁴¹, and the photoreceptors need to generate a dark-current (see below), perform phototransduction in response to incoming photons⁴², and synthesize new outer segments on a daily basis⁴³. In fact the retina is one of the most energetically demanding organ of the body – evident by its oxygen demand per weight exceeding even that of the brain⁴⁴.

Photoreceptors are unique to other types of neurons in that they must maintain a depolarized state in the absence of stimulus. The depolarization of unstimulated photoreceptors is called the *dark current*, though it should be noted that even under photopic adaptation, cone photoreceptors maintain a dark current, rendering them responsive to photon catch (the very basis for daylight vision). The maintenance of dark currents by constant Na^+/K^+ ATPase activities accounts for greater part of the retina's excessive energy demand (when compared to other organs, including the myocardium). Additionally, considerable energy is required for the synthesis that ensues outer segment disc shedding, the reuptake of glutamate, not to mention to meet the metabolic demands of numerous types of neurons and glial cells. Na^+/K^+ ATPase pumps are also densely expressed in the RPE apical membranes, producing a chemical gradient that maintains a fluid and ion gradient in the subretinal space. RPE cells also recycle the chromophore retinaldehyde and phagocytose shed photoreceptor outer segment discs. Axons of retinal ganglion cells (the only retina output to the CNS) express Na^+/K^+ ATPase as well⁴⁵. The sheer energetic cost underlying visual system physiology can be inferred by readily regressed visual organs of cave-dwelling or deep-sea creatures⁴⁶.

To meet the high energy demand, retina utilizes both OXPHOS and aerobic glycolysis (also known as Warburg effect; energy production via glycolysis without OXPHOS even in presence

of oxygen)⁴⁷. The degree of contributions from each processes to the overall ATP production

varies depending on the cells; where Muller cells^{42,48} and outer segment of

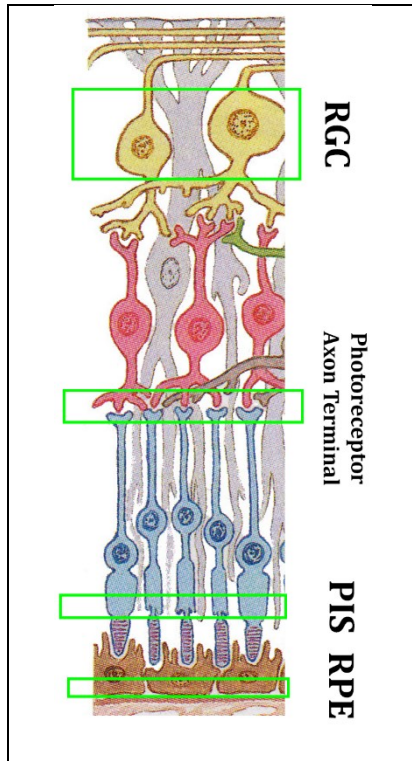


Figure 1.2 Regions of High Mitochondrial Concentration As Reported by Stone et al⁴⁹. Retinal ganglion cell (RGC) layer, axonal terminal of photoreceptors, photoreceptor inner segment (PIS), and retinal pigment epithelium (RPE) are highlighted. The site of highest concentrations is the PIS. Figure is adopted from Kolb et al⁵⁰.

photoreceptor rely more on the aerobic glycolysis whereas the inner segment of photoreceptor on OXPHOS^{47,51}. The exact cell types that carry out aerobic glycolysis remain controversial⁵²; and the implication of retina's aerobic glycolysis (commonly seen in tumor cells⁴⁷) is not completely understood. There is recent experimental evidence supporting that the extensive protein synthesis required to replenish the shed photoreceptor discs is powered via aerobic glycolysis as opposed to OXPHOS as previously assumed⁵².

The regions that rely heavily on OXPHOS for energy production are equipped with highly concentrated populations of mitochondria and direct access to vascular networks. The ophthalmic artery branches into the choroidal and retinal arteries that respectively supply nutrients and oxygen to the outer and the inner retina. Being avascular, the outer retina

receives its oxygen through passive diffusion from the choroidal capillary across the RPE monolayer, which acts as the blood-retinal barrier. On the other hand, the central retinal artery vascularizes the inner retina directly, where tight junctions between endothelial cells form the blood-retinal barrier. Both barriers express numerous GLUT1⁵³ (other types of glucose

transporter, such as GLUT2, 3, and 5 have been reported also⁵⁴) that allow facilitated diffusion of glucose. In photoreceptors, mitochondria are densely packed in the ellipsoidal region of inner segment (IS) and the axon terminals presynaptic to bipolar cells. These sites are located close to the outermost capillaries of the central retinal vasculature⁴⁹. RPE basal membrane, ganglion cells and Muller cells also bear densely packed mitochondria, strategically located close to blood vessels (**Figure 1.2**)^{49,55}. Interestingly, rods and cones have different mitochondrial distributions and mode of energy production⁵⁶, which may have a significance in development of macular-specific diseases.

1.3 MITOCHONDRIAL INVOLVEMENT OF RETINAL DISEASES

1.3.1 Primary Mitochondrial Disorders

Numerous factors contribute to mitochondria being key players in retinal health^{57,58}. Firstly, the retina relies heavily on OXPHOS to meet the heavy metabolic demand of photoreceptor physiology. Unfortunately, the anatomical requirements of retina as a vision sensory organ and the ensuing metabolic strategies that evolved to meet its energy demands have rendered the outer retina (RPE and photoreceptors, both being post-mitotic) highly susceptible to oxidative stress. The list of contributors is extensive, from unregulated high ppO_2 levels and glucose transport activity, high proportion (50%) of the most oxidizable fatty acid (docosahexaenoic acid, DHA, providing the fluidity required of phototransduction)⁵⁹, frequent direct exposure to light⁶⁰ (mostly in the macula) that can induce photodynamic-ROS, and densely packed mitochondria. Oxidative damage to mitochondria can trigger further production of ROS from mitochondria. Known as the

vicious cycle of mitochondrial ROS production, this self-amplifying ROS production is pathological contributors to retinal disease progression and in some cases causation.

This intricate link between mitochondria and vision health may be inferred by the numerous mitochondrial disorders that are associated with visual impairment. In Leber's Optic Neuropathy, a disease caused by mtDNA mutation⁵⁸, CI function is impaired in all mitochondria of the body. However, the main phenotype is in the visual system. Retinal ganglion cells and their axons (forming the optic nerve) degenerate leading to blindness. A similar phenomenon is also observed in Dominant Optic Atrophy, where mutations in X-linked genes encoding inner mitochondrial membrane proteins that play a role in mitochondrial fusion, respiratory coupling, and mtDNA integrity cause pronounced effect in visual system^{61,62}. Furthermore, common eye diseases such as DR, age-related macular degeneration (AMD), and glaucoma⁶³. While not the primary defect mitochondrial dysfunctions play important roles in disease progression, and novel data even suggest a role in disease onset. DR and Stargardt-like macular dystrophy (STGD), a juvenile form of macular degeneration, will be discussed in greater details below.

1.3.2 Diabetic Retinopathy

Diabetes is a systemic disease characterized by defective glucose regulation. It may result from insufficient insulin secretion from pancreatic islet cells (Type 1) or insufficient insulin sensitivity in tissues (Type 2; T2DM). A hallmark of diabetes is development of the hyperglycemia. Prolonged hyperglycemic exposure leads to multiple chronic complications throughout the body⁶⁴. Small vessels are especially sensitive to hyperglycemic insults⁶⁵. As a result, diabetic complications in microvasculature (such as diabetic neuropathy, nephropathy, and retinopathy) are the most common. Diabetic retinopathy (DR) is a landmark microvascular

complication of diabetes⁶⁶, where inner retinal microvasculature is compromised. This leads to abnormal vitreous environment and functional and histological disruptions of the retinal cells that depend on inner retinal blood supply (namely RGCs and amacrine cells), leading to loss of vision⁶⁷.

If detected early and intervened with appropriate lifestyle changes and preventative therapies, the progression of DR and associated vision losses can be avoided or slowed down. DR is a slow progressing disease where symptoms are not apparent in first few years of the disease, which makes early detection difficult. Furthermore, the prevalence of DR increases significantly with prolonged disease duration, with almost 90% in T1DM patients and 60-80% of T2DM becoming affected over 20-25 years following presumed disease onset⁶⁶. DR is the leading cause of blindness among working age adults in developed world^{68,69} and one of the most common ocular diseases. The global prevalence of diabetes itself is increasing at an alarming rate, expecting to reach over 10% of population, 642 million people, by the year 2040⁷⁰. The financial burden for patients with DR on healthcare system are almost double that of those without it⁷¹. Considering the high prevalence rate of DR, coupled with many new diabetic patients arising from developing nations where infrastructure for early detection and preventative treatment is not well implemented, DR represent a significant threat to vision health and the health care system.

Even though DR pathogenesis is still not fully understood, specific biochemical pathway that connects hyperglycemia to vascular damage have been identified: activation of polyol (sorbitol-aldose reductase) pathway, hexosamine pathway, protein kinase C (PKC) pathway, and advanced glycation end products (AGEs) pathway. Oxidative stress is a common denominator found in all of these pathways. In the polyol pathway, increased sorbitol production by aldose reductase

diminishes the production of anti-oxidative glutathione (GSH) and increases ROS production from cytosolic NADPH oxidase^{27,30,72,73} (indirectly through upregulating sorbitol dehydrogenase activity). Activation of the hexosamine pathway similarly contributes to oxidative stress through depletion of GSH pool. PKC delta pathway is activated by oxidative stress and further exaggerates ROS generation, as does accumulation of AGE products.

As covered in **Chapter 1.1.2**, mitochondria are also a significant source and prominent target of oxidative stress. Expectedly, mitochondria play a central role in development of DR. While the exact mechanism that connects the hyperglycemia to mitochondrial damage is not understood completely, both *in vivo* and *in vitro* experiments demonstrate various mitochondrial defects throughout the disease development. Mitochondrial membrane integrity was compromised⁷⁴, expression of genes related to mitochondrial fission and fusion was disturbed⁷⁵, and diminished OXPHOS functions have been reported. It is worth noting that this study only provides a ROUTINE mitochondrial function using the XF Analyzer⁷⁶; this data does not give much information on changed functions of specific components of ETS. Additionally, the overexpression of the mitochondrial antioxidative enzyme, mitochondrial superoxide dismutase (MnSOD) in mice models, mitigates diabetes-induced vascular damages^{59,77}. Furthermore, the outer retina accounts for the majority of oxidative stress production in animal models of DR⁷⁸, where the highest concentration of mitochondria is. The missing piece of puzzle regarding the mitochondrial role in DR is whether mitochondrial dysfunction is due to oxidative stress or oxidative stress is due to mitochondrial dysfunction, it is a chicken and egg conundrum.

Activation of these biochemical pathways leads to the loss of retinal pericytes and anterior smooth muscle cells in the inner retinal vasculature, followed by thickening of basement

membrane, increased adhesion of leukocytes to the blood vessel, and increased vascular permeability⁷⁹. Endothelial cells eventually degenerate, leading to acellular blood vessels and nonperfusion. Under funduscopy investigation, microaneurysms, dot/flame hemorrhage, cotton-wool spots, venous beading, exudates, and retinal edema can be observed. Localized hypoxia leads to the production of angiogenic factors (Hypoxia-Inducible Factor 1 α and Vascular Endothelial Growth Factor), causing the growth of new fragile and leaky blood vessel in retina; we are now in the proliferative phase³⁰. Ultimately, neovascularization is compounded by the formation of glial scarring, which can exert a tractional retinal detachment. Of note, degeneration of the neural retina precedes vascular changes, causing delayed dark adaptation, decreased contrast sensitivity, and disturbances in electroretinogram (ERG) responses such as reduced amplitude of oscillatory potential⁸⁰ and reduced multifocal ERG implicit time⁸¹ – all of which represent key diagnostic tools⁸².

1.3.3 Nile Rat Model of T2DM and Diabetic Retinopathy

Various genetic and chemically-induced animal models of T2DM have been employed in past studies⁸³. While these models succeed in reproducing some symptoms seen in human patients, these artificial disease induction models often fail to capture the complexity of human disease. For instance, manipulation of leptin signaling system is commonly seen in multiple models such as *ob/ob* and *db/db* mice in *C57BLKS/J* background strain or Zucker Diabetic Fatty rats. Chemical destruction of islet β -cell by alloxan or streptozotocin is also commonly used. Some models that use diet-induced obesity often rely on high-fat diet. All of the mentioned models differ significantly with human T2DM etiology. In human T2DM, there is not a single gene that causes diabetes and instead, multiple genetic factors and environmental factors play a

role and the route of pancreatic damage is not direct chemical damage or surgical removal. Therefore, these animal models may not be suitable for studies of delicate nutritional physiology in T2DM or studies of slowly and insidiously developing diabetic complications^{83,84}.

Native to the Nile river delta, savannah grasslands, and forests of North African and southwestern Arabian Peninsula, the Nile grass rat (*Arvicanthis niloticus*) is a promising and relatively new T2DM animal model. It more closely mirrors the human development of T2DM. Nile rats spontaneously develop diabetes without genetic or chemical intervention. When kept in captivity with unlimited access to rodent chow (higher in calories and lower in fiber compared to their native plant- and insect-based diet⁸⁵), Nile rats progressively develop T2DM over the course of a year. Many pertinent signs of human T2DM and metabolic syndrome (MetS) - a term for a cluster of physiological conditions that often accompany T2DM such as central obesity - are observed in Nile rats. These animals can develop liver steatosis, progressive chronic nephropathy, reduced β -cell size with abnormal pancreatic islet morphology⁸⁶. For still unknown reasons, males are more susceptible than females⁸⁷. Furthermore, T2DM development follows the 5 stages of diabetic progression proposed by Wier et al.⁸⁸: normoglycemic and hyperinsulinemic compensational stage 1 at 2mo, hyperglycemia decompensation at 6mo, and severe decompensation and collapse of β -cells seen by 18mo⁸⁹.

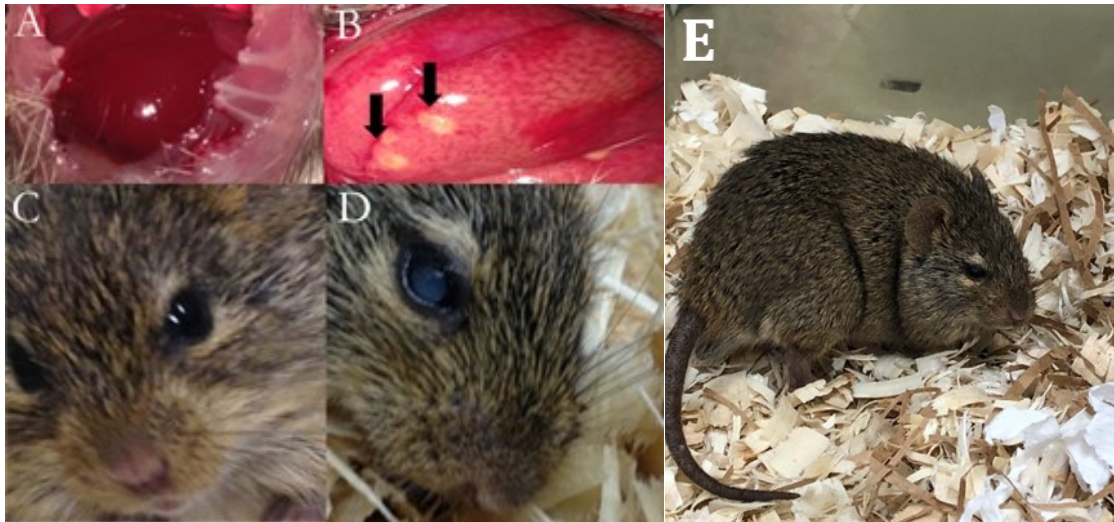


Figure 1.3 Nile Rats Phenotypes During T2DM Progression. Liver from 2mo high-fiber diet (A) and 18mo normal chow fed animals (B) are shown. Evidences of fatty liver deposits are indicated by black arrows. 6mo normal chow fed animal with clear lens (C) is compared with an animal showing signs of cataractogenesis in 18mo normal chow fed animal (D). A typical fully grown (6mo) chow fed animal is shown (E).

Nile rats' spontaneous and slow T2DM provide an excellent opportunity for studies of slowly progressing diabetic complications such as DR. Additionally, their diurnal lifestyle and higher cone-to-rod ratio make them even more attractive model for DR studies. Nile rats were introduced to laboratory environment for study of the circadian rhythm⁹⁰. They have substantially higher percentage of cone population compared to nocturnal laboratory rodents (30-35% in Nile rats compared to 1-2% in mouse and rat^{91,92}). While Nile rat's cone concentration is not the same as human's (which is 5%), they can be a good approximation of human macula (100% cone). Cones and rods have several different functional characteristics; namely, the rods are more sensitive to light and slower in the light response and recovery. Moreover, cones contain more mitochondria and have more surface membrane area in their mitochondrial cristae; perhaps reflecting cones' need for greater energy generation^{56,93}. Therefore, having cone

distribution that is similar to humans in Nile rats gives them an attractive quality as model of DR. Furthermore, since the circadian rhythm plays an important factor in T2DM development⁹⁴, Nile rats' closer-to-human circadian rhythm provides a closer-to-human environment for T2DM studies compared to conventional models which are nocturnal.

1.3.4 Stargardt-Like Macular Degeneration and Transgenic Mice Model

Stargardt disease is a juvenile form of progressive macular degeneration that arises from genetic mutations. The most common form, STGD1 is caused by a mutation in *ATP-binding cassette, subfamily A, member 4 (Abca4)*. It is the most common inherited retinal disease⁹⁵ and shows an autosomal recessive inheritance pattern. A rarer autosomal recessive inheritance pattern of disease has also been identified; one of which is STGD3. It is caused by a single allelic mutation in *elongation of very long-chain fatty acids 4 (Elovl4)* gene. Normally, ELOVL4 protein is expressed in photoreceptors and is targeted to photoreceptor cells' endoplasmic reticulum (ER) membrane to partake in the biosynthesis of very long-chain saturated and polyunsaturated fatty acids (VLC-FA and -PUFA). The ER retention signal at the C-terminus is lost in mutant ELOVL4 proteins, leading to death of photoreceptors and vision loss.

Skin and brain dysfunctions have been reported in patients expressing homozygous *Elovl4* mutation⁹⁶, presumably reflecting the crucial role of VLC-PUFA as brain and skin lipids. In the retina, VLC-PUFA has been shown to tightly associate with rhodopsin with a possible role in phototransduction by maintaining curvature and fluidity of the photoreceptor membrane⁹⁷. Developing mice models of STGD3 have been attempted with a homozygous knock-in (KI) and knock out (KO) of *Elovl4* but it was found that both would lead to neonatal lethality in mice due

to skin permeability problems. Instead, transgenic mice expressing human *Elovl4* gene have been developed (TG1, TG2, and TG3). They have a varying degree of expression of human mutant transgene compared to wild-type transgene model (approximately 1 to 1 in TG1, 2-fold in TG2, and 5-fold in TG3 mice). The challenge of the transgene model is that it is difficult to discern the effect caused by ELOVL4 mutation independently from overexpression of transgene as well as the wildtype mouse protein.

There are number of not mutually exclusive possible mechanisms in which *Elovl4* mutation could lead to photoreceptor death: (1) decreased VLC-PUFA synthesis from enzymatically inactive ELOVL4 protein leading to structural and/or functional defect in photoreceptor membrane and subsequently cell death, (2) mislocalization of enzymatically active ELOVL4 protein (for truncated proteins' active site is preserved) leading to production and accumulation of toxic 3-keto intermediate in other cellular compartments⁹⁸, (3) truncated ELOVL4 protein forming and aggregation in photoreceptor outer segment (POS) and inducing unfolded protein response (UPR) and/or (4) mislocalized truncated protein leading to defective POS phagocytosis. Any of these mechanisms could lead to RPE cell death followed by photoreceptor cell death seen in STGD, as well as a more common form of macular degeneration such as age-related macular degeneration (AMD).

However, it should be noted that: (1) even a near-total loss of retinal VLC-PUFA content did not induce electrophysiological or behavioral defects in TG animals⁹⁹, (2) cell culture studies show that mutant ELOVL4 proteins are not enzymatically active despite having intact active site¹⁰⁰ and (3) the aggregation of truncated protein initiates UPR in cell line models, but not in the TG animals' POS¹⁰¹. Therefore, defective phagocytosis by RPE seems to be likely culprit

behind STGD3 pathogenesis. Precisely which step(s) of phagocytosis is impaired by the truncated protein remains elusive.

While mitochondria have not received much attention in the past studies of STGD, there are multiple steps of phagocytosis that are energy-intensive, such as phagosome movement from apical to basal membrane of RPE and acidification of phagosome. Additionally, oxidative stress, though where it originally arises from is not clear, is an important step of STGD pathogenesis. For instance, lipofuscin accumulation is one of the hallmarks of AMD and STGD. Lipofuscin is a complex protein aggregation that is a product of incomplete digestion of internalized POS discs by RPE's lysosomes during phagocytosis. They are indigestible and thus inexorably accumulate in the RPE. Lipofuscin releases ROS to its surrounding environment and may lead to damaged mitochondria. Subsequently, this causes decreased energy production and mitochondrial production of ROS and the start of the *vicious cycle* of oxidative stress.

1.4 PHOTOBIMODULATION AS MITOCHONDRIA TARGETING THERAPY OF OCULAR DISEASES

1.4.1 Overview of Mitochondria Targeting Therapies

Reflecting the immensely diverse role of mitochondria in the cellular physiology, a wide range of drugs works through or interacts with mitochondria. Examples include anticancer, antidiabetic, anesthetic, antiarrhythmics, and antibiotics¹⁰². These drugs can exert their effect via modifying various aspects of mitochondrial physiology such as ETS, fatty acid metabolism, and mitochondrial transporters^{103,104}. However, drugs that specifically target mitochondria with the

purpose of addressing mitochondrial defects are relatively rare¹⁰⁵, despite frequent reports of mitochondrial involvement in a wide range of diseases.

Management strategies of most mitochondrial diseases, including those with pronounced ocular effects like Leber's congenital Hereditary Optic Neuropathy, focus primarily on limiting exposure to mitochondrial stressors (e.g. cigarette smoking and alcohol¹⁰⁶) and establishing optimal health conditions through lifestyle changes rather than pharmaceutical interventions. The benefit of exercise in mitochondrial health is widely-accepted^{107,108}; exercise increases mitochondrial respiratory capacity in skeletal muscle as well as promote mitochondrial biogenesis¹⁰⁹. An appropriate level of caloric restriction (i.e. without malnutrition) produces a similarly beneficial effect in mitochondrial biogenesis and suppress activation of inflammatory pathways and ROS production^{109,110}. Additionally, studies report that the ketogenic diet, conventionally used for the treatment of a certain type of epilepsies, can increase mitochondrial biogenesis, function, decrease ROS production, and mtDNA deletion^{111,112}. Dietary supplements such as creatine, carnitine, and dichloroacetate are also used for their energy-boosting effect, stimulation of β -oxidation, and lactate-lowering effect, respectively¹⁰⁵.

The most widely used pharmaceuticals for mitochondrial conditions are antioxidants such as coenzyme Q₁₀ (CoQ10)¹¹³. They are often used along with vitamin supplements and antioxidant peptides as an *antioxidant cocktail*. Also known as ubiquinone, CoQ10 is an organic molecule composed of a hydrophobic tail and a redox active quinone ring that is an essential component of mitochondrial ETS. They serve as electron carrier from CI and CII to CIII and disease involving CoQ10 deficiency result in mitochondrial dysfunction¹¹⁴. In addition, they also interact with mitochondrial membrane permeability transition pore and inhibit apoptosis¹¹⁵. They also have

potent antioxidative properties¹¹⁶. Beneficial effects of CoQ10 from preclinical and laboratory settings have been reported, including CoQ10 containing eye-drops preserving corneal mitochondrial function and promoting wound healing following UV-light insult¹¹⁷ and CoQ10 analog improving impaired mitochondrial CI function and improving visual acuity in LHON patients. However, poor intestinal absorption of CoQ10 may limit its utility¹¹³; though it should be noted that there are different delivery methods¹¹⁸ being investigated as well as CoQ10 derivatives that are designed to increase higher absorptivity such as MitoQ and SkQ1^{119,120}.

1.4.2 Photobiomodulation

Photobiomodulation (PBM) is a relatively novel approach that ameliorates disease symptoms through (reportedly) direct modulation of mitochondrial function¹²¹. They are also referred to as Low Level Light Therapy (LLLT) or Near-Infrared (NIR) therapy. PBM consists of a single or series of brief light illumination carried out by a light emitting diode (LED) or laser at a specific frequency corresponding to the far-red or near-infrared range (600-1,000nm)¹²². Importantly, these light applications are carried out in *low intensity*, which is vaguely defined as the intensity that does not elicit any photo-thermal effects on target biological tissues or cells. A wide range of positive effects of PBM is reported: including anti-inflammation¹²³, pain reduction¹²⁴, promotion of tissue healing^{125–127}, neuroprotection, and augmented toxin resistance^{128–130}. Conveniently, NIR range of light happens to have a good penetration characteristic in biological tissue – a phenomenon called “NIR window of biological tissue¹³¹”. In biological tissue, light penetration is limited mainly by scattering and absorption of light by water, blood, and lipids. Water limits penetration of light at high wavelength and blood at the low wavelength. The NIR range of light happens to fall between these two points of obstacle¹³¹. Combined with the rising popularity of

mitochondria as a therapeutic target in various diseases, there is a great enthusiasm in the investigation of PBM's therapeutic applications.

The idea that light can modulate biological events was realized shortly after the invention of the laser in 1960. Mester et al.¹³² serendipitously discovered 694 nm light's ability to accelerate wound healing and hair growth in mice during failed attempt to reproduce previously reported the tumoricidal effect of the laser using significantly weaker laser by mistake. The connections between mitochondria and PBM started to emerge about two decades after Mester's initial discovery, with initial reports of increased ATP following light treatment¹³³ and subsequent observations that mitochondrial inhibition could be reversed with light with specific spectra¹³⁴⁻¹³⁶. The seminal work by Karu et al. demonstrated that the light that correspond to absorption spectra of mitochondrial CIV, more specifically, two heme centers (a and a₃) and two copper centers (Cu_A and Cu_B)¹³⁷, produced maximal biological effects¹³⁸.

The contemporary model of PBM describes that the mitochondrial ETS enzyme CIV (cytochrome *c* oxidase) as the main photoacceptor and effector of PBM. In this model, the effect of PBM occurs in two stages: primary and secondary. The primary effect of PBM describes the direct photochemical change that takes places during or directly after the light exposure. The light exposure by CIV displaces nitric oxide (NO) from CIV's oxygen binding site. NO is a reversible inhibitor of CIV¹³⁹. That is, PBM increases CIV function through disinhibition. Reportedly, the NO-mediated disinhibition of CIV results in an overall increase in electron flow through the ETS and also increases the mitochondrial ATP production. The subsequent increased mitochondrial ROS from upregulated ETS activity is also suggested¹⁴⁰. Following this primary action of PBM, increased mitochondrial activity results in the secondary effect of PBM, which

reflects effects of PBM hours to days after the light exposure that occur as consequences of the primary action. First, the increased ATP availability has reported potential implications such as ATP signaling and neuroprotective effect^{141,142}. NO (displaced from CIV) can act as the second messenger and regulate immune response and cause vasodilation. Changes to the redox environment seem to modulate wide ranges of biochemical pathways such as Janus kinase-signal transducer and activator of transcription (JAK-STAT) pathway and nuclear factor kappa-light-chain-enhancer of activated B cells (Nf-κB) pathway^{140,143–145}. Secondary effects of PBM also include enhanced the anti-oxidative capacity of mitochondria and retrograde signaling from mitochondria to nucleus¹⁴⁶ that increases the RNA and DNA synthesis¹³⁸ and causes upregulation of various genes; 111 genes of 10 functional categories were reported in a study of human fibroblast cells¹⁴⁷.

While this general model of ‘NO-mediated CIV functional increase → increased ATP → activation of survival and protective pathways’ is implicitly assumed in the majority of studies involving the PBM, there are surprisingly little amount of studies that investigate mitochondrial functional changes in response to NIR light exposure, aside from the action spectra studies^{128,138} that were used to suggest CIV functional increasing effect of PBM.

1.4.3 PBM in Treatment of Ocular Diseases

Clinical usages of PBM have been broadened over the years to include treatment of diabetic ulcers, neurological pain, peripheral nerve damages, stroke, and myocardial infractions¹⁴⁸. Given the easy light access, eye diseases such as DR, AMD, and glaucoma are attractive targets for PBM and are actively being investigated^{149–151}. The biggest concern regarding the application of NIR light in the eye is the light damage. Prolonged exposure to white light causes irreversible

damage to photoreceptors and RPE and blue light causes S cone damage¹⁵². Green and red-light cause M and L cone damage, respectively, though they are reversible. However, *in vivo* animal studies demonstrate that PBM can achieve therapeutic effects without incurring light damages, presumably due to low energy carried by NIR wavelength light. Furthermore, the PBM's light irradiance is low (maximum value reported is 60 mW/cm², almost 5-fold smaller than white light intensity that caused irreversible damage) and NIR light produces only negligible thermal effect on the retina and choroidal vessels of treated animals. FDA classifies PBM devices as “general wellness device” that possesses non-significant risk for human use. Thus, while most of the studies involving PBM's treatment of retinal diseases are carried out in rodent models, there is a growing number of studies examining human patients.

Investigations of ocular application of PBM are still in their infancy; regardless, there are still an abundant amount of encouraging empirical reports. In animal studies, pre-treatment with PBM protect the retina from toxins such as methanol¹²⁹, potassium cyanide, rotenone, and 1-methyl-4-phenylpyridinium (MPP+)¹⁵³, light^{123,154,155} and oxygen-induced damages¹⁵⁶, diabetic retinal insults¹⁵⁷⁻¹⁵⁹, aging related decline in mitochondrial function¹⁶⁰ and various models of macular degeneration¹⁶¹⁻¹⁶³ as measured by the preservation of histological changes and functional changes such as ERG or optokinetic parameters. In a limited number of human studies, a successful outcome has been reported in diabetic macular edema, dry form of AMD, and glaucoma where patients showed a reduction of retinal thickening, improved visual acuity, drusen volume, and reduction of IOP¹⁴⁹⁻¹⁵¹. These findings are summarized in **Table 1.1**.

Big hurdles preventing wide adaptation of PBM are (1) incomplete understanding of PBM's biochemical mechanism and (2) inconsistency in light parameters (e.g. wavelength, irradiance,

etc.) used in literature. To add on to the latter point, many researchers in biological background lack the necessary physics background to appropriately report and/or apply the light parameters. Nevertheless, as interest in PBM and other mitochondrial targeting therapies continue to rise, the scientifically-sound investigations of PBM are accumulating.

Table 1.1 Summaries of PBM Studies in Ocular context

Study	Model	Light parameters	Effect
Eells et al. 2003 ¹²⁹	Long-Evans rats. Methanol toxicity.	LED, 670nm, 28mW/cm ² , 4J/cm ² , 144 s	Attenuated retinotoxic effect; preservation of rod- and cone- ERG responses and no enlarged PIS and fragmented photoreceptor nuclei.
Liang et al. 2008 ¹⁵³	Sprague Dawley rats' primary neuron culture. Toxin-induced toxicity	LED, 670nm, 50mW/cm ² , 4J/cm ² , 80s, twice daily*	PBM treated cells had higher cell survival with lower ROS and RNS against potassium cyanide, rotenone, and 1-methyl-4-phenylpyridinium ion (MPP+).
Albarracin et al. 2011 ¹²³	Sprague Dawley rats. Light damage model of AMD	LED, 670nm, 60mW/cm ² , 9J/cm ² , 180s	Attenuated histological changes, prevented cell death, and ERG changes.
Rutar et al. 2012 ¹⁶¹	Sprague Dawley rats. Light damage model of AMD	LED, 670nm, 50mW/cm ² , 9J/cm ² , 180 s daily for 5 days	Reduced oxidative stress marker. Reduced expression of complement genes.
Tang et al. 2014 ¹⁵⁰	T2DM patients with non-center-involving diabetic macular oedema. One eye treated while other was control.	LED, 670nm, 80mW/cm ² , 25J/cm ² , 2.5cm away, 80s twice daily for 2 months.	Macular thickness measured through SD-OCT improved in treated eyes.
Fuma et al. 2015 ¹⁶³	ARPE-19. Oxidative stress induced with H ₂ O ₂ .	LED, 670nm, 3.89mW/cm ² , 250 s twice a day for 4 days	Reduced ROS production (measured with CM-H2 DCFDA, JC-1 dye, and CCK-8) but did not rescue H ₂ O ₂ induced a defect in phagocytosis.
Saliba et al. 2015 ¹⁵⁸	C57Bl/6J mice, streptozotocin injection model of DR.	LED, 670nm, 20.25mW/cm ² , 240 s daily for 10 wks	Reduced superoxide, leukostasis, expression of ICAM-1, and improved visual performances (optokinetics).
Calaza et al. 2015 ¹⁶²	C57 BL/6 Complement factor H knockout (<i>Cfh</i> ^{-/-}) mice model of AMD.	LED, 670nm, 40mW/cm ² , 90 s daily for 5 days.	ATP content decline in <i>Cfh</i> ^{-/-} mice increased 50% compared to non-treated <i>Cfh</i> ^{-/-} animals. Increased mitochondrial membrane potential and reduced age-related inflammation are observed.
Merry et al. 2016 ¹⁵¹	Patients with dry AMD.	Multiwavelength LED 590, 670, 790nm, 80mW/cm ² , 4J/cm ² , 88s per session, 9 sessions over 3 weeks.	Increased best corrected visual acuity, improved contrast sensitivity, reduced drusen volume and thickness.
Sivapathasuntharam et al. 2017 ¹⁶⁰	C57BL/6 mice. Aging.	LED, 670nm, 40mW/cm ² , 900s daily*	Age-related decline in ERG parameters (a- and b-waves) in 7mo and 12mo animals were improved (amplitude of response). Greater CIV staining in NIR treated animals reported.

Table 1.1 Summaries of PBM Studies in Ocular context (continued)

Study	Model	Light parameters	Effect
Lu et al. 2018 ¹⁵⁹	Sprague Dawley rats. Light damage model of AMD.	LED, 670nm, 60mW/cm ² , 2.5cm away, 180s daily for 5 days.	Reduced activation of Muller cells, lower stress markers (GFAP, FGF-2), and pro-inflammatory cytokines (IL-1 β)
Cheng et al. 2018 ¹⁶⁴	C57BL/6J streptozotocin injection model of DR.	LED, 670nm, 25mW/cm ² , 2-3cm away, 240s daily for 8 months.	Reduced diabetes-induced leakage and degeneration of retinal capillaries, function (optokinetics), number of circulating stem cells, and vitamin D receptor mRNA level.

* Overall period not specified

2 EXPERIMENTAL RATIONALE

2.1 OVERVIEW

Despite the often and widely reported pathogenic roles of mitochondria in major ocular diseases such as DR and AMD⁶³, many functional aspects of retinal mitochondria are not understood well. Furthermore, many of the previous reports of retinal mitochondrial function were acquired using techniques with various limitations that diminish their reliability. A comprehensive understanding of disease mechanism is fundamental for an effective development of preventative therapies, which are especially valuable in many ocular diseases where a loss of visual function is often irreversible. The Oxygraph 2K high-resolution respirometer enables detailed investigation of mitochondrial function without the limitations found in previously used methods. The present thesis provides pioneering accounts of its utilization in study of rodent ocular mitochondria. The preliminary accounts of mitochondria-related effects of photobiomodulation are also presented.

2.2 HYPOTHESIS

We hypothesize that prodromal changes will be observed in ocular (neural retina and RPE) mitochondria in pre-disease states of Nile rat model of DR and ELOVL4 model of STGD3. Furthermore, we hypothesize that PBM treatment with 670nm light at 0.5J/cm² fluence will elicit increased CIV function in Jurkat and HEK293T cell lines.

2.3 AIMS

1. To demonstrate the validity of studying retinal and RPE mitochondrial function with the O2k respirometer.
2. To investigate early-mitochondrial functional changes in retina and RPE in Nile rat model of T2DM and ELOVL4 mice model of STGD3 using high-resolution respirometry.
3. To provide preliminary evaluation of PBM's ability to modify CIV function by studying the effect of a single PBM application with high-resolution respirometry.

3 MODIFICATIONS IN RETINAL MITOCHONDRIAL RESPIRATION PRECEDE TYPE 2 DIABETES AND PROTRACTED MICROVASCULAR RETINOPATHY

3.1.1 Introduction

With a worldwide prevalence of 415 million and importantly, estimates that only one out of every two adults has been diagnosed⁷⁰, the number of individuals living with diabetes may be closer to 1 billion. In adults, T2D accounts for the majority (90-95%) of diagnosed cases of diabetes¹⁶⁵. A well-recognized microvascular complication of diabetes is diabetic retinopathy (DR).

Clinically, DR is an inner retina pathology that begins with the non-proliferative form characterized by alterations in blood flow, death of retinal pericytes and basement membrane thickening.^{3,4} Subsequently, the disease progresses to non-perfusion, microaneurysms, vascular loops, and hemorrhages evident on ophthalmic examination¹⁶⁶. Ultimately, DR evolves to a proliferative stage, typified by neovascularization, neurodegeneration, and retinal detachment, which cause irreversible vision loss¹⁶⁷. The cellular mechanisms underlying microvascular complications involve neurovascular cross talk, which is currently under intense scrutiny¹⁶⁸. There is accumulating evidence that the outer retina, although asymptomatic itself, contributes to these microvascular changes^{78,169}. Photoreceptor inner segments, in view of their extremely high metabolic activity¹⁷⁰, their constitutive production of high amounts of ROS¹⁷¹, and their high capacity for mitochondrial oxidative phosphorylation¹⁷², are attracting increasing attention in the pathophysiology of DR⁸⁴. A major hurdle in identifying early pathological events in DR has been

the prevalence of animal models with early onset of diabetes^{84,173,174}. In this study, we relied on the combined advantages of the laboratory rodent *Arvicanthis niloticus*: 1) it is a well-established model of T2D^{86,89,175} and of associated retinopathy¹⁷⁶; 2) unlike mouse and rat models, retinopathy progresses in a cone-rich retina (30-35%, as opposed to 1-2% in mouse and rat)^{91,92}, therefore more closely approximating the human macula (cone dominated area); and 3) unlike mice and rats, Nile rats are diurnal, as humans are¹⁷⁷. The latter advantage is particularly pertinent in the context that development of T2D has been associated with circadian rhythm disruption via the dysregulation of clock genes⁹⁴.

During development of T2D, Nile rats undergo an initial compensation for insulin resistance with increased insulin secretion at 2 mo, followed by rising glucose levels from 6 mo, increasing β -cell dysfunction and associated endoplasmic reticulum stress at 12 mo, and finally, severe decompensation and progression to ketosis at 18 mo^{86,89,175}. Of note, feeding of a high fiber diet completely prevents T2D in Nile rats⁸⁹. Noda et al.¹⁷⁶ described the protracted accumulation of leukocytes in retinal arteries at high plasma insulin levels, which was correlated with plasma leptin (body fat) in this model, and furthermore, demonstrated microvascular biomarkers of human early DR¹⁷⁸ including tortuosity, acellular capillaries, and pericyte ghosts, all of which corroborate pericyte apoptosis. Hajmoussa et al.¹⁷⁹ attributed pericyte apoptosis, *in vitro*, to hyperglycemia-induced accumulation of reactive oxygen species (ROS). Long-term exposure of “pericyte-like” adipose-derived stromal cells to hyperglycemia was also associated with impaired glucose uptake and mitochondrial electron transport system capacity measured in the intact cells after uncoupling¹⁷⁹.

While mitochondrial dysfunction has been extensively studied in T2D, with distinct links between obesity, inactivity and energy homeostasis, a causal relationship has yet to be established for the development of DR¹⁰⁹. Deficiencies in mitochondrial biogenesis and/or activity as well as chronic imbalances in energy metabolism have been documented¹⁸⁰⁻¹⁸², in tissues other than the retina (such as muscle, liver and pancreas), with healthy aging and across all T2D stages: (1) insulin sensitive with normal oxidative capacity and load; (2) prediabetic with compensation for insulin resistance characterized by low oxidative capacity (inactivity, aging), increased oxidative load (overnutrition, obesity) and associated with initially increased mitochondrial biogenesis; but incomplete oxidation ultimately leads to accumulation of lipid intermediates, fatty acid oxidation products and ROS that induce (3) compensation failure and insulin secretory dysfunction (hyperglycemia). In the retina, alterations in mitochondrial membrane structure have been documented in hyperglycemia-induced DR⁷⁵. Using the streptozotocin-injected (STZ) rat model of type 1 diabetes, Zhong and Kowluru⁷⁵ reported enlarged mitochondria with loss of cristae in retinal microvasculature, which persisted after reversal to normoglycemia.

Here, we took advantage of the long-term beta-cell compensation and T2D prevention in control Nile rats fed high fiber diet versus those fed standard diet, in which compensation fails, to examine the interplay in the retina between early dysregulation of glucose metabolism and mitochondrial oxidative phosphorylation changes in a prediabetic stage prior to clinical manifestation of DR.

3.2 METHODS

3.2.1 Animals and Diets

This study was performed on male Nile rats (*Arvicanthis niloticus*) aged 2 to 18 mo of age; females were excluded on the basis of their reduced susceptibility to develop T2D⁸⁶ and to control for potential sexual dimorphisms with respect to metabolic pathways. After weaning at 21 days, animals were divided into two diet groups: 1) prediabetic and diabetic animals fed standard rodent diet (Prolab[®] RMH 2000, 5P06, LabDiet, Nutrition Intl., Richmond, IN, USA; 9.6% fat, 3.2% fiber), known to induce hyperinsulinemia by 2 mo, followed by hyperglycemia from 6 mo and decompensation at 18 mo⁸⁹; or 2) control animals fed high fiber diet (Mazuri[®] Chinchilla Diet, 5M01, Purina Mills, LLC, St. Louis, MO, USA; 4.1% fat, 15.0% fiber), normoglycemic to 18 mo. Food and water were provided *ad libitum*. Animals were maintained on a 14:10 light-dark cycle, room temperature $21 \pm 2^{\circ}\text{C}$ and relative humidity ~40%. This research was done under the approval of the Institutional Animal Care and Use Committee (University of Alberta). Experiments were carried out in accordance with NIH (USA) guidelines regarding the care and use of animals for experimental procedures and the ARVO (Association for Research in Vision and Ophthalmology) Statement for the Use of Animals in Ophthalmic and Visual Research.

3.2.2 Fasting blood glucose, glycated hemoglobin and plasma insulin

Fasting blood glucose (FBG) values were measured from tail blood samples after overnight (16-18 h) fasting using an Accu-chek Compact Plus glucose monitoring system (Roche,

Mississauga, ON, Canada). Hyperglycemia was determined as FBG levels >5.6 mmol/L (100 mg/dL) as previously described⁸⁹.

Nile rats were euthanized with a lethal dose (480 mg/kg) of Euthanyl (Bimeda-MTC Animal Health Inc., Cambridge, ON, Canada). When animals reached surgical plane, cardiac puncture was performed and blood was collected in K₂EDTA-coated BD Microtainer™ Tubes with Microgard™ Closures (Becton, Dickinson and Company, Mississauga, ON, Canada). After centrifugation at 2000 rpm for 20 min. at 4°C, plasma was collected and stored at -80°C until use.

Plasma insulin levels were assessed using an insulin ELISA kit (Ultra Sensitive Mouse Insulin ELISA kit #90080, Crystal Chem Inc., Downers Grove, IL, USA). Fasting insulin levels >2 ng/mL were indicative of compensation as previously described⁸⁹.

Glycated hemoglobin (HbA1c) was measured using a GLYCO-Tek affinity column kit (#5351, Helena Laboratories, Beaumont, TX, USA). Absorbance was measured at 415 nm. Percentage of HbA1c (*%HbA1c*) in the sample was calculated as recommended by the manufacturer. Nile rats with HbA1c levels >6.5% were considered diabetic, as previously defined^{89,183}.

3.2.3 Funduscopy

Nile rats were anaesthetized using ketamine:xylazine (75:30 mg/kg). Eyes were dilated with corneal application of 1% tropicamide and 2.5 % phenylephrine; and kept hydrated with Tear-gel (Novartis Pharmaceuticals Canada Inc., Mississauga, ON, Canada). Images from both eyes were captured using a Micron III retina imaging system for rodents (Phoenix Research Laboratories,

Inc., Pleasanton, CA, USA) equipped with a Semrock FF01-554/211 filter for white light, FF01-469/35 exciter and BLP01-488R barrier filters for blue excitation with green emission (Semrock, Inc., Rochester, NY, USA) and StreamPix 5 software (NorPix, Montreal, QC, Canada). Fluorescein angiography images were captured after intraperitoneal injection with fluorescein (1.5 μ L/g body weight of 100 mg/mL fluorescein in PBS; F6377 Sigma, Oakville, ON, Canada).

3.2.4 Trypsin digestion of retinal vasculature

After overnight fixation (16-18 h) in 4% paraformaldehyde, retinas were removed and immersed in 3% trypsin in 0.1M Tris, pH 7.8 (pre-heated to 37°C) for 130 min. Following digestion, the vitreous was carefully removed and the retina was subjected to gentle trituration with water to separate disintegrated neuronal tissue from the vasculature. Isolated vascular networks were mounted, treated with periodic acid solution and stained with Schiff's reagent and hematoxylin (Periodic Acid-Schiff kit 395B-1KT, Sigma-Aldrich, St. Louis, MO, USA).

Pericytes were identified as round, dark extracapillary protrusions when compared to endothelial cells, which were oval shaped and lighter in color¹⁸⁴. Images were captured on a Reichert Polyvar 2 microscope with Infinity Analyze imaging software (Lumenera Corporation, Ottawa, ON, Canada) using a 40x oil objective. Counts of pericytes, endothelial cells and degenerated capillaries were performed and normalized to capillary area using ImageJ 1.48v software (National Institutes of Health, USA, <http://imagej.nih.gov/ij>). Pericytes were categorized into three subtypes based on location; pericytes located on straight capillaries, forked capillaries and bridged between capillaries were classified as longitudinal, forked and bridging

pericytes, respectively. Six diabetic and six control animals were assessed at each time point (6, 12 and 18 mo), and 5 randomly selected images per animal were analyzed. All variables met the criteria of normality and homogeneity of variance for ANOVA as tested with Kolmogorov-Smirnov (Lilliefors' correction) and Spearman tests, respectively. Therefore, differences between diet groups could be analyzed using two-way ANOVA with Bonferroni post hoc comparisons. Significance was set to $p < 0.05$.

3.2.5 Immunohistochemistry

After enucleation, corneas were punctured, and eyes were fixed in 4% PFA for 30 min. at 4°C. Corneas and lenses were carefully removed, and posterior eyecups were fixed a further 30 min., cryoprotected in sucrose (10 and 20% for 1 h each, 30% overnight), embedded in O.C.T. (Tissue-Tek, Sakura® Finetek, Torrance, CA, USA), frozen in liquid nitrogen and stored at -80°C.

For cross sections, 20 µm cryosections were cut along the naso-temporal axis. After blocking in 10% normal serum and 0.3% triton X-100 in PBS for 2 hours, sections were reacted overnight with goat anti-choline acetyl transferase (ChAT; 1:200; AB144P; Chemicon, Etobicoke, ON, Canada). All incubations were performed at room temperature. The following day sections were washed (3 x 5 min.) in PBS and reacted for 2 h with donkey anti-goat Alexa594 antibody (1:500; Molecular Probes Inc, Eugene, OR, USA). After washing in PBS, slides were coated with ProLong® Gold anti-fade reagent with DAPI (Life Technologies, Carlsbad, CA, USA) and coverslipped. Images were captured from the central and peripheral retina on a Leica DM6000B

fluorescence microscope with DFC360FX camera and LAS AF v2.2.0 software (Leica Microsystems, Inc.), using a HC PL FLUORTAR 20.0x0.50 DRY objective (448.60 μm window). Brightness and contrast were adjusted using Adobe Photoshop CC 2015 software.

ChAT-immunoreactive amacrine cells and displaced amacrine cells (found in the GCL) were counted on both sides of the optic nerve and averaged (\pm standard deviation). Outer and inner nuclear layer thickness measures were performed in the same manner. Comparisons were made using Mann-Whitney U-test. Significance was set to $p < 0.05$.

For whole retina flatmounts, retinas were washed extensively (6 x 30 min.) in PBS + 0.1% tween-20 + 0.3% triton X-100 and then blocked for 2 h in 5% normal goat (or horse) serum in same, with shaking at room temperature for both steps. Flatmounts were then reacted with either goat anti-4-hydroxynonenal (4-HNE; 1:200; ab46544 Abcam, Cambridge, UK) or mouse anti-nitrotyrosine (NT; 1:100; 189542 Cayman Chemical, Ann Arbor, MI, USA) diluted in PBS + 0.3% triton X-100 for 4 days at 4°C. After washing as before, flatmounts were incubated with species appropriate Alexa488 secondary antibodies (1:1000) + DyLight® 594 *Lycopersicon esculentum* (Tomato) Lectin (TL; 1:100; DL-1177 Vector Laboratories, Burlingame, CA, USA) in a 1/10 dilution of blocking solution for 2 days at 4°C. After final washing, retinas were mounted ganglion cell side up in Fluoromount™ Aqueous Mounting Media (F4680-25ML; Sigma-Aldrich, St. Louis, MO, USA) and coverslipped. Images were captured as above.

3.2.6 ERG recordings

ERGs were recorded at 18 mo (n=6 diabetic animals, n= 3 control animals). Nile rats were dark-adapted one hour prior to recording, and all subsequent preparations were made under dim red light. Animals were anaesthetised with inhaled isoflurane (Somnosuite, Small Animal Anesthesia System; Kent Scientific, Torrington, CT, USA) and placed over a homeothermic blanket to maintain their body temperature at 38°C. Pupils were dilated with one drop of 1% tropicamide and corneas were kept hydrated with methylcellulose. ERG recordings were performed as previously described⁹². Data were analyzed in a single eye per animal, selected on the basis of largest maximal a-wave amplitude in the scotopic intensity series. For oscillatory potential (OP) analysis, to ensure consistency between traces, amplitudes and implicit times were calculated by manually placing cursors at the base and apex of the first 4 OPs; cursors were sequentially labeled from 1 to 8 and values (amplitude or implicit time) were plotted for each cursor against stimulus strength.

Scotopic ERG: Intensity response series in dark-adapted animals were generated by presenting flashes (10 μ s duration, 6500°K, xenon bulb) ranging between -3.70 to 2.86 log cd s/m^2 in luminance over 16 consecutive incremental steps. Intensity levels were measured with a photometer at the cornea level. Inter-stimulus intervals ranging from 10 s to 2 min. were used for lowest to highest intensity flashes, respectively, providing sufficient time for rods to recover from photobleaching. Responses were recorded 3-6 times and averaged to optimize signal-to-noise ratio. For all recordings, a-wave amplitude corresponded to the difference between baseline at time 0 s (flash delivery) and negative a-wave trough, while b-wave amplitude corresponded to

the difference between negative a-wave trough and positive b-wave peak (excluding OPs). Criterion amplitudes were set to 10 μV .

Mesopic ERG: After completion of scotopic ERG recordings, animals were exposed to a background illumination of 0.01 cd/m^2 for 10 min. prior to applying the same tests as described above.

Photopic ERG: Finally, after completion of mesopic ERG recordings, animals were light adapted at 30 cd/m^2 background for 10 min. Intensity response series were generated by presenting white flashes ranging between -1.63 to $2.86 \log \text{cd s}/\text{m}^2$ in luminance over 11 consecutive incremental steps. Responses were recorded 6 times and averaged. Inter-stimulus intervals of 3 s were used. Flicker response series were then recorded to flashes of $1.36 \log \text{cd s}/\text{m}^2$ presented at the following thirteen incremental frequencies: 3, 5, 10, 15, 20, 25, 30, 35, 40, 45, 50, 55, and 60 Hz. The first 3 seconds were not harvested, avoiding averaging responses to single flashes. Amplitudes were measured from adjacent trough to peak and latencies from flash onset to peak.

Statistical comparison for each marker (1 to 8) was assessed using non-parametric Kruskal-Wallis on way analysis of variance. Significance was set to $p < 0.05$.

3.2.7 High-resolution respirometry

High-resolution respirometry (Oxygraph 2k; OROBOROS Instruments, Innsbruck, Austria) was performed using freshly isolated retinas from individual Nile rats from 2 to 18 mo ($n=5-12$ per group, replicate measurements from a single animal were pooled). The oxygraph was

calibrated at 37 °C as per manufacturer's instructions with each chamber filled with 2 mL of Mitochondrial Respiration Medium 05 (MiR05; 0.5 mM EGTA, 3 mM MgCl₂·6H₂O, 60 mM K-lactobionate, 20 mM taurine, 10 mM KH₂PO₄, 20 mM HEPES, 110 mM sucrose and 1 g/L BSA essentially fatty acid free, pH 7.1)⁴⁰. Datlab software (OROBOROS Instruments, Innsbruck, Austria) was used for data acquisition and analysis.

Wet weight was measured and retinas were immediately transferred into 1 mL of ice-cold MiR05. Retinas were homogenized on ice with a Potter-Elvehjem attached to an overhead stirrer (Wheaton Instruments, Millville, NJ, USA). After five passes at intensity level two, 200 µL of homogenate was immediately placed in each oxygraph chamber containing 1.8 mL of MiR05. The remaining homogenate was frozen at -80 °C for determination of total protein (Pierce BCA protein assay kit, Cat.# PI-23227, Thermo Fisher Scientific) and citrate synthase (CS) activity (according to Kuznetsov et al.¹⁸⁵). CS (EC 4.1.3.7) activity was measured at 37 °C using a UV/Vis spectrophotometer (Ultrospec 2100 Pro, Biochrom, Cambridge, USA) equipped with a thermostated cell holder and a circulating water bath. After thawing the sample on ice, an additional cycle of homogenization with a conical glass homogenizer for 30 s on ice was performed to ensure complete homogeneity of the sample. The absorbance was measured at 412 nm following the reduction of 0.1 mM 5,5'-dithiobis-2-nitrobenzoic acid (ϵ : 13.6 mL cm⁻¹ µmol⁻¹) in the presence of 0.31 mM acetyl-CoA, 0.5 mM oxalacetic acid, 0.25% triton X-100, 100 mM Tris-HCl buffer (pH 8.0), and 25 µL of the retina homogenate in a spectrophotometer cuvette containing a total volume of 1 mL.

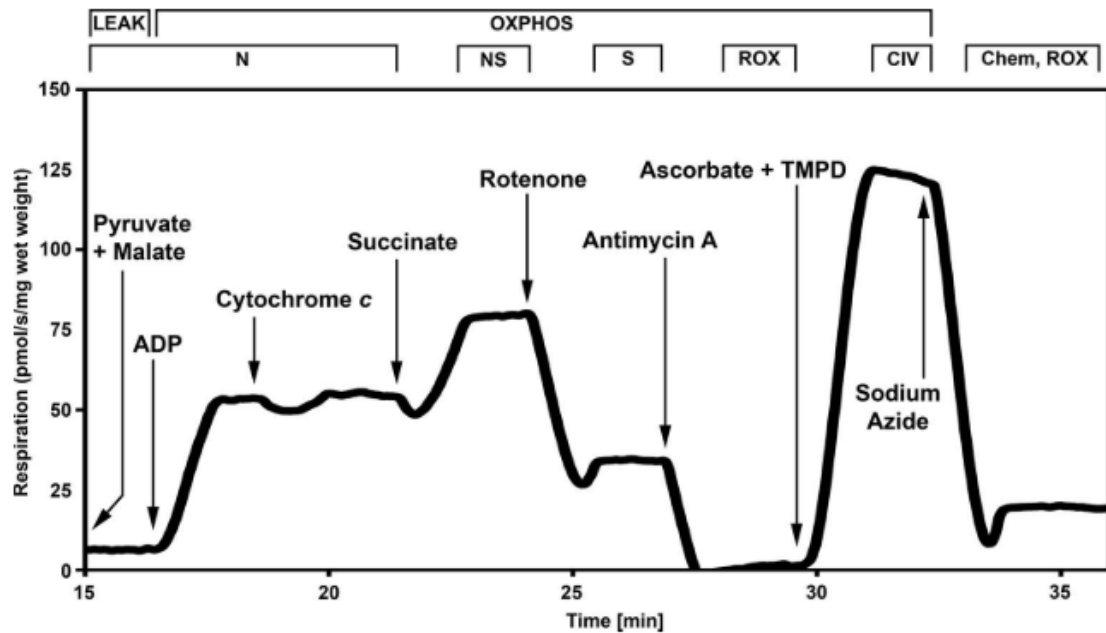


Figure 3.1 Representative trace of high-resolution respirometry using a multiple substrate-inhibitor-titration protocol in retinas from a single Nile rat. The oxygen consumption (y-axis) is represented as a function of time (x-axis). Arrows indicate times of titrations of substrates and inhibitors. The protocol includes the following steps: pyruvate&malate (added before the homogenate, N, NADH-pathway, -LEAK state), ADP (N pathway, OXPHOS capacity); cytochrome c (integrity of outer mitochondrial membrane; damaged membrane allows exogenous cytochrome c to enter the intermembrane space, causing an increase in respiration), succinate (NADH and Succinate-pathway, NS, OXPHOS capacity), rotenone (inhibition of Complex I, S, Succinate-pathway, S, OXPHOS capacity), antimycin A (inhibition of Complex III, ROX), ascorbate&TMPD (CIV, Complex IV single step), sodium azide (inhibition of Complex IV, chemical background, Chem, ROX).

The protocol used for evaluating mitochondrial function is presented in *Figure 3.1*. Two different states are measured: LEAK respiration represents the non-phosphorylated state in the absence of ADP, and OXPHOS represents oxygen consumption coupled to phosphorylation of ADP to ATP in the presence of saturating ADP. The following substrates and inhibitors were added (final chamber concentration): pyruvate (5 mM), malate (5 mM), ADP (2.5 mM), cytochrome c (10 μ M), succinate (10 mM), rotenone (1 μ M), antimycin A (5 μ M), ascorbate (2

mM), tetramethylphenylenediamine (TMPD; 0.5 mM), and sodium azide (100 mM). Pyruvate and malate were added before the retina homogenate and the chamber was closed immediately after homogenate addition. An uncoupler titration (dinitrophenol; 5 μ M steps) was performed after succinate in order to determine the maximal capacity of the electron transport system (ETS). Furthermore, addition of digitonin after ADP did not show any increase in respiration, confirming that none of the plasma membranes were left intact after homogenization (results not shown). Mitochondrial respiration was corrected for oxygen flux due to instrumental background, and for residual oxygen consumption (ROX) after inhibition of Complex I and III, with rotenone and antimycin A, respectively¹⁸⁶. This protocol provides an indirect assessment of Complex III activity. Although electrons are initially fed into Complexes I, II or I&II, defects in steps downstream of the Q-cycle, requiring electron transfer by Complexes III and IV, impact the capacity of Complexes I and II. For Complex IV respiration, the chemical background measured in presence of sodium azide was subtracted.

For the detection of qualitative changes in the OXPHOS system, respiration was expressed as Flux Control Ratio, FCR, normalized for maximal OXPHOS capacity in presence of substrates simultaneously feeding electrons into both NADH and Succinate-pathways (Complex I and II, respectively).

Statistical analyses were performed with SigmaStat 4 (Aspire Software International, Ashburn, VA, USA). Criteria of normality and homogeneity of variance for ANOVA were tested for each variable with Kolmogorov-Smirnov (Lilliefors' correction) and Spearman tests, respectively. For variables meeting the above criteria (FCR, for NADH and Succinate-pathways;

and CS activity), differences between age-matched diet groups were tested using two-way ANOVA, followed by pairwise Tukey comparison. For variables not meeting the criteria (Coupling Control Ratio; FCR for Complex IV; and Cytochrome *c* Control Factor), age-matched differences were analyzed with Mann-Whitney U-test. Unless otherwise stated, values reported in this study represent mean \pm standard error of the mean (sem). Significance was set to $p < 0.05$.

3.3 RESULTS

3.3.1 Changes in retinal mitochondrial respiration precede T2D

Flux Control Ratio (when normalized for maximal OXPHOS capacity) allows detection of qualitative changes, and this approach revealed a greater NADH-pathway contribution to maximal OXPHOS capacity at 2 mo (**Figure 3.2A**). At hyperglycemia onset (6 mo), no differences were observed; however, statistical comparisons segregating hyperglycemic and hyperinsulinemic status, revealed an increase attributed to hyperinsulinemia alone. After sustained hyperglycemia (18 mo), NADH-pathway FCR was lower in diabetic compared to control animals, and this was accompanied by an increased Succinate-pathway contribution to maximal OXPHOS capacity (**Figure 3.2B**). Statistical comparisons segregating hyperglycemic and hyperinsulinemic status, confirmed that this increase was attributed to increases in FBG (18 mo).

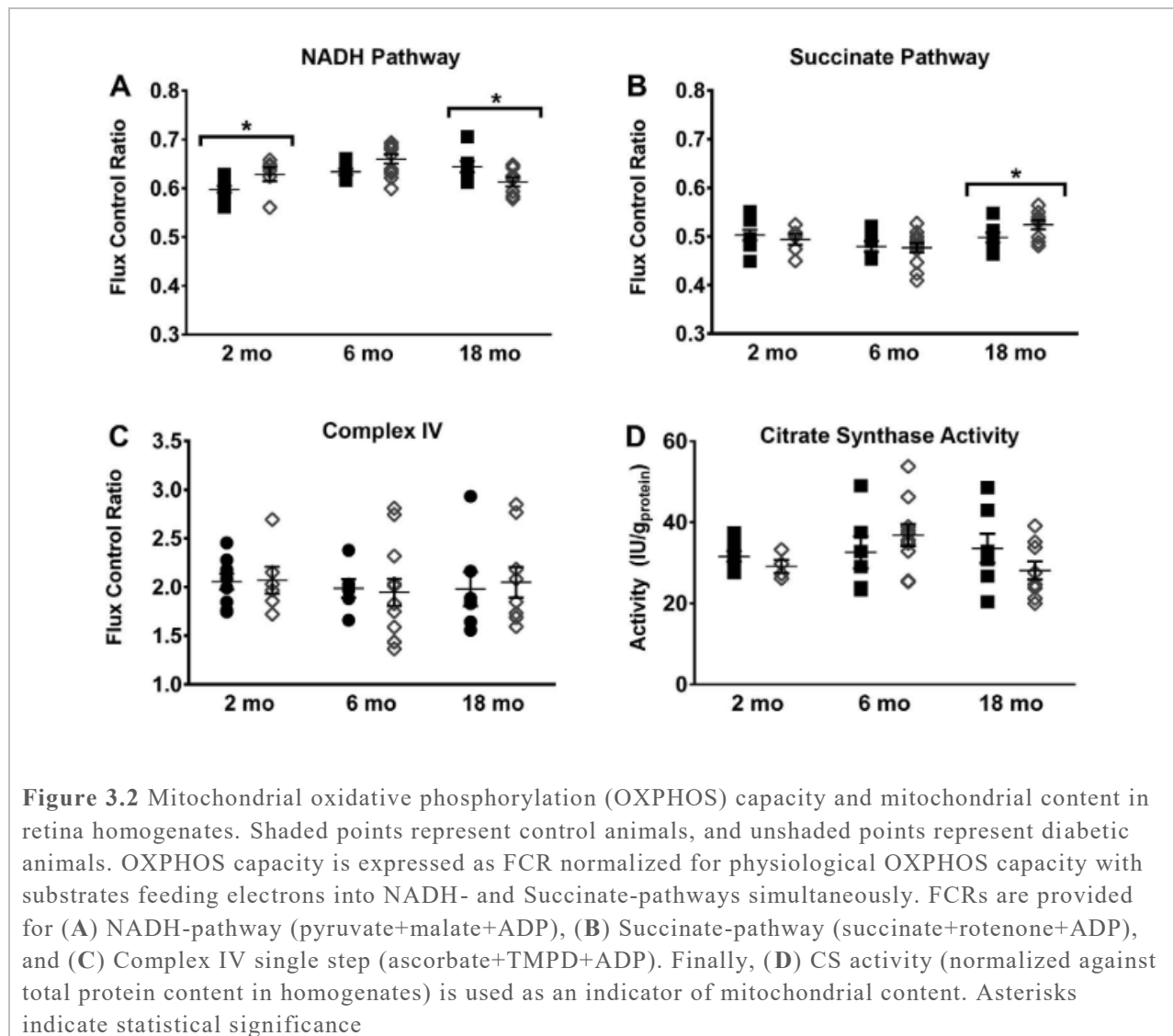


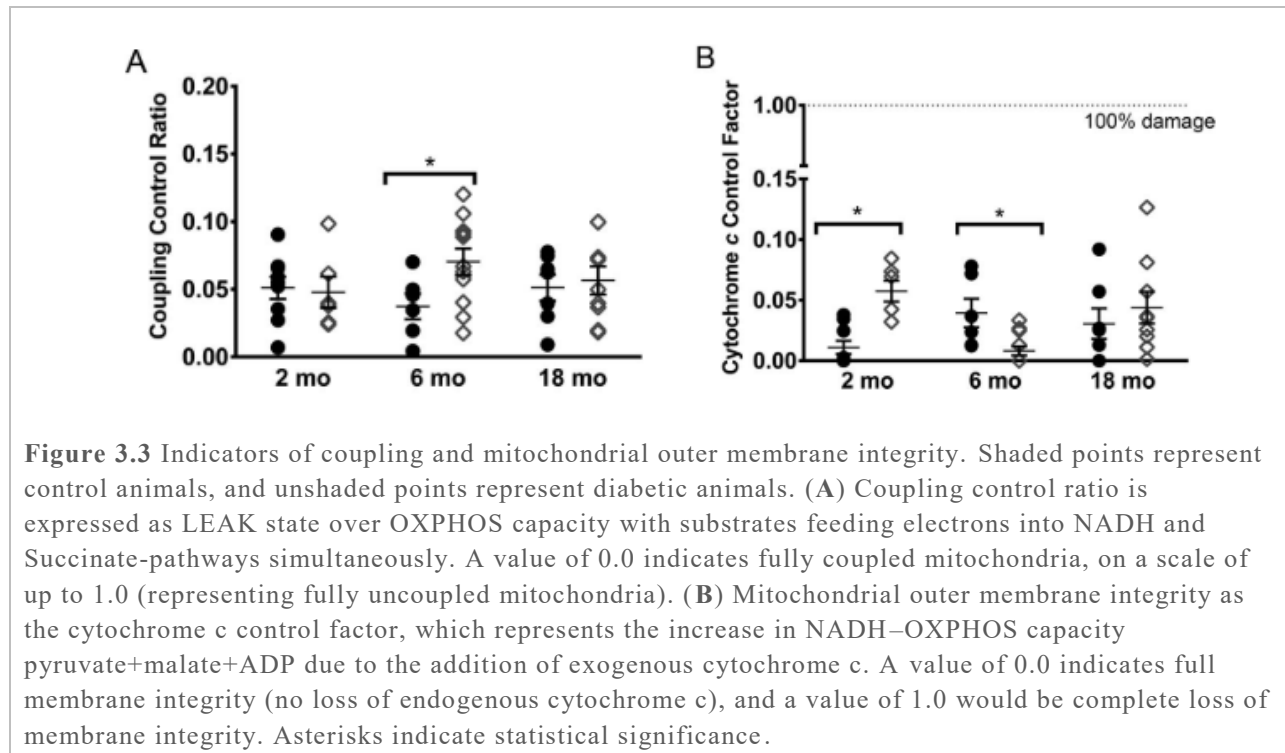
Table 3.1 Retinal Mitochondrial Function Expressed in Flux per Mass

	2 mo		6 mo		18 mo	
	Prediabetic	Control	Diabetic	Control	Diabetic	Control
LEAK	2.2 ± 0.7	2.8 ± 0.5	4.1 ± 0.6*	2.2 ± 0.7	2.6 ± 0.5	2.2 ± 0.4
NADH pathway	29 ± 5	32 ± 3	36 ± 3	34 ± 4	30 ± 3	29 ± 2
Succinate pathway	22 ± 4	27 ± 3	26 ± 2	26 ± 3	26 ± 3	22 ± 2
NADH-succinate pathway	46 ± 7	54 ± 5	55 ± 4	53 ± 6	49 ± 5	44 ± 3
Maximal COX capacity	96 ± 17	111 ± 11	102 ± 8	104 ± 10	99 ± 10	86 ± 6

COX, cytochrome *c* oxidase.* $P < 0.05$.

Regardless of FBG levels, FCR for Complex IV did not vary at any of the time points examined (Figure 2C). The phosphorylation system did not exert a limitation on electron transport in NR retinas; ratios of maximal OXPHOS/ETS were 0.97 ± 0.03 and 0.96 ± 0.01 in diabetic versus control animals, respectively. Mitochondrial respiratory capacity expressed as a function of tissue mass did not vary between diets (**Table 3.1**) and mitochondrial content, as reflected by CS activity, was comparable between age-matched diet groups (**Figure 3.2D**).

Coupling Control Ratio (LEAK over maximal OXPHOS; below 0.12; **Figure 3.3A**) and stimulation of respiration following addition of ADP (**Figure 3.1**), together demonstrate that mitochondrial electron transport and OXPHOS were well coupled at all ages under our experimental conditions. Coupling Control Ratio increases in diabetic animals at 6 mo indicated elevated proton leakage and electron slip in the absence of ADP phosphorylation. There were no differences in Coupling Control Ratio at other time points.



Cytochrome *c* Control Factor was higher in prediabetic (2 mo) Nile rats (**Figure 3.3B**). At hyperglycemia onset (6 mo), the opposite effect was observed, and was still attributed to hyperinsulinemia alone. No differences were detected at 18 mo, regardless of insulin or FBG levels.

3.3.2 Type 2 diabetes

Nile rats fed standard rodent diet, progressed from less than 10 percent of animals (8%) displaying T2D (FBG levels >5.6 mmol/L) at the first time point examined (2 mo), to approximately one-half (44%) demonstrating both elevated FBG and HbA1c by 6 mo (Table 2). On this diet, hyperinsulinemia rates doubled from 2 to 6 mo (40% to 83%). Hyperinsulinemia

declined to 15% at 12 mo, with even higher proportions of Nile rats demonstrating elevated FBG (81%) and HbA1c (89%). At the latest time point (18 mo) 80% of Nile rats showed a history of hyperglycemia as indicated by elevated HbA1c levels.

Controls never exceeded the threshold for hyperglycemia at any time point. In agreement with maintained normoglycemia at 18 mo, controls also exhibited normal HbA1c levels. However, of note, increasing rates of hyperinsulinemia were detected in controls at 6 mo (18%), 12 mo (38%) and 18 mo (62%).

Table 3.2 Metabolic Phenotype of Nile Rat

	2 mo		6 mo		12 mo		18 mo	
	Control (n = 11)	Prediabetic (n = 7)	Control (n = 10)	Diabetic (n = 12)	Control (n = 21)	Diabetic (n = 20)	Control (n = 16)	Diabetic (n = 25)
Body weight, g	66 ± 3	73 ± 3	92 ± 3	98 ± 5	103 ± 3	122 ± 1*	108 ± 3	122 ± 2*
BMI, kg/m ²	5.4 ± 0.2	5.8 ± 0.2	6.9 ± 0.2	7.3 ± 0.3	5.2 ± 0.1	5.9 ± 0.1*	5.5 ± 0.1	5.9 ± 0.1*
FBG, mM	2.9 ± 0.3	2.7 ± 1.4	3.2 ± 1.6	5.4 ± 1.9*	3.8 ± 0.1	10.8 ± 1.1*	3.7 ± 0.2	8.6 ± 1.3*
HbA1c†	N/A	N/A	4.3 ± 0.1	4.1 ± 0.1	4.0 ± 0.1	7.8 ± 0.6*	5.0 ± 0.4	7.7 ± 0.6*
Insulin,‡ ng/mL	0.9 ± 0.3	4.3 ± 1.5*	2.9 ± 1.5	5.6 ± 0.9*	2.2 ± 0.7	0.9 ± 0.3*	2.6 ± 0.6	0.7 ± 0.2*

Data represented as mean ± SEM, Mann-Whitney *U* test. N/A, not applicable.

* *P* < 0.05.

† A subset of animals was used, *n* = 4, 6 (6 months); 4, 8 (12 months), and 4, 10 (18 months); control and diabetic, respectively.

‡ A subset of animals was used, *n* = 4, 5 (2 months); *n* = 5, 9 (6 months); 13, 20 (12 months), and 6, 6 (18 months); control and prediabetic/diabetic, respectively.

3.3.3 Early diabetic retinopathy

The first clinical sign of retinopathy (pericyte loss) is observed in T2D Nile rats from 12 mo (**Figure 3.4A**). These animals exhibited a preferential loss of longitudinal pericytes from 12 mo onwards (**Figure 3.4B**; 12 mo, 1481 ± 111 vs 1746 ± 183; 18 mo, 1163 ± 131 vs 1563 ± 84, in diabetic vs control animals respectively). This corresponds to a 15 ± 3% loss in the total number of longitudinal pericytes at 12 mo. The decline in this cell population progressed to 26 ± 4% at

18 mo. In contrast, forked pericytes and bridged pericyte cell populations were unaffected. The total pericyte-to-endothelial cell (TP:EC) ratio at 6 mo is approximately 1:1 (*Figure 3.4C*) and declines thereafter due to pericyte loss.

The number of degenerated capillaries was unchanged at 12 mo, however, at 18 mo there was a >3-fold increase in the number of degenerated capillaries (156 ± 36 in diabetic vs 47 ± 36 in control animals; *Figure 3.4D*).

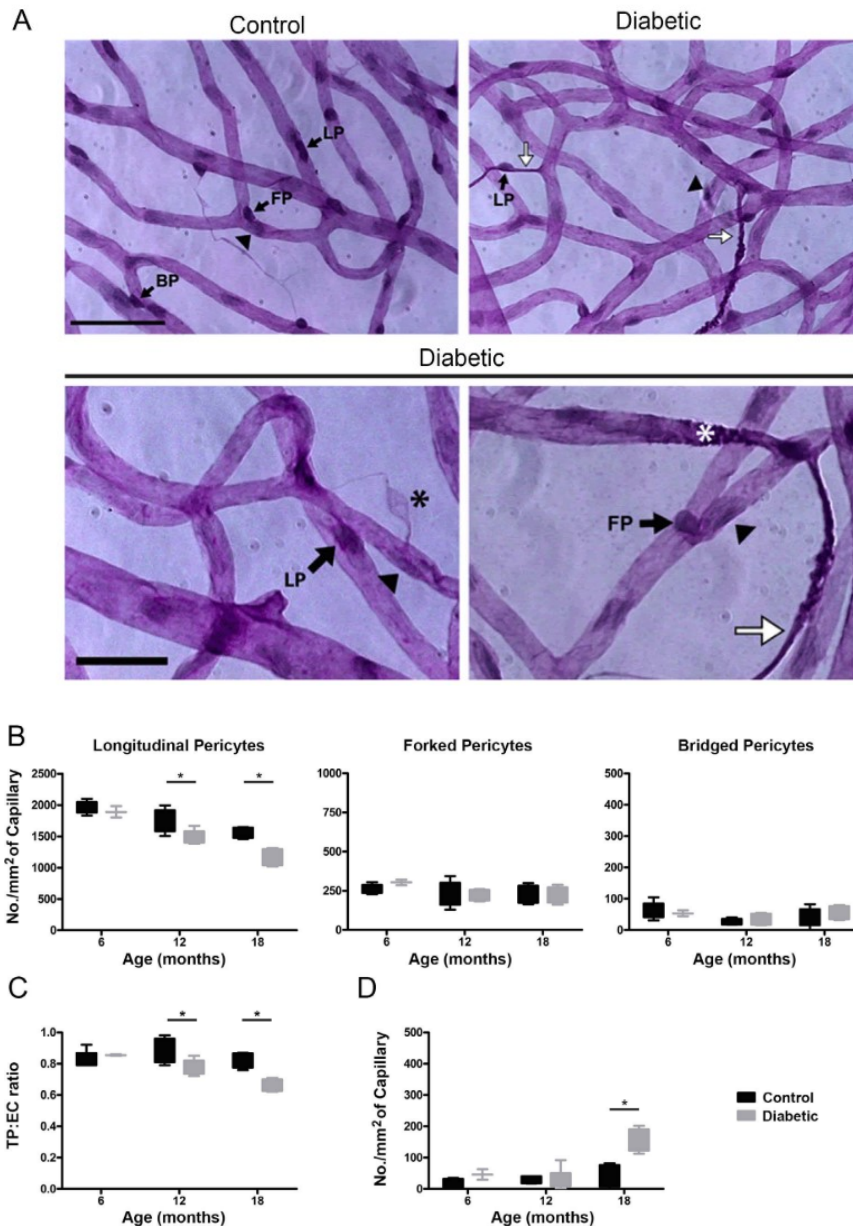


Figure 3.4 Retinal digest preparations of diabetic and control Nile rat retinas. Representative images (A) of isolated retinal vasculature, 12 (lower row) and 18 months (upper row). Quantification of pericyte numbers (B), total TP:EC ratio (C), and number of degenerated capillaries (D). Scale bar:50 μ m upper panel;20 μ m, enlarged images in lower panel. Black arrows: pericytes; arrowheads: endothelial cells; white arrows: tortuous capillaries; white asterisk: early capillary degeneration; black asterisk: pericyte ghost. Asterisks on graphs indicate statistical significance. LP, longitudinal pericyte; FP, forked pericyte; BP, bridged pericyte.

A second clinical sign of DR demonstrated in diabetic Nile rats is delayed ERG OP kinetics (*Figure 3.5*). OP implicit times were delayed, exclusively under photopic adaptation. Cursor positions on OP base and apex were shifted to longer times, with the exception of two cursors (5 and 6) corresponding to the largest amplitudes in the OP bursts. OP amplitudes were unaffected.

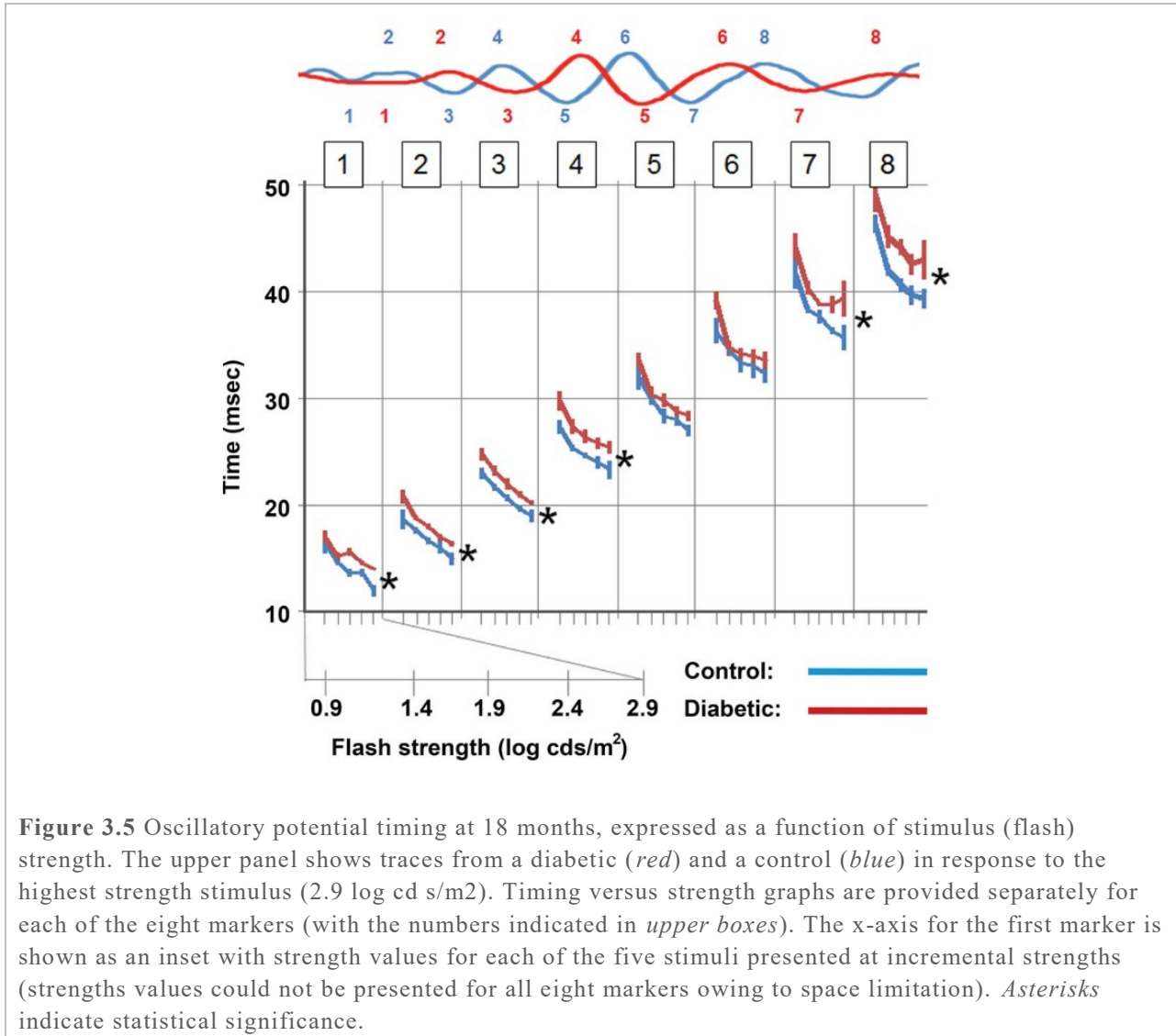


Figure 3.5 Oscillatory potential timing at 18 months, expressed as a function of stimulus (flash) strength. The upper panel shows traces from a diabetic (*red*) and a control (*blue*) in response to the highest strength stimulus (2.9 log cd s/m²). Timing versus strength graphs are provided separately for each of the eight markers (with the numbers indicated in *upper boxes*). The x-axis for the first marker is shown as an inset with strength values for each of the five stimuli presented at incremental strengths (strengths values could not be presented for all eight markers owing to space limitation). *Asterisks* indicate statistical significance.

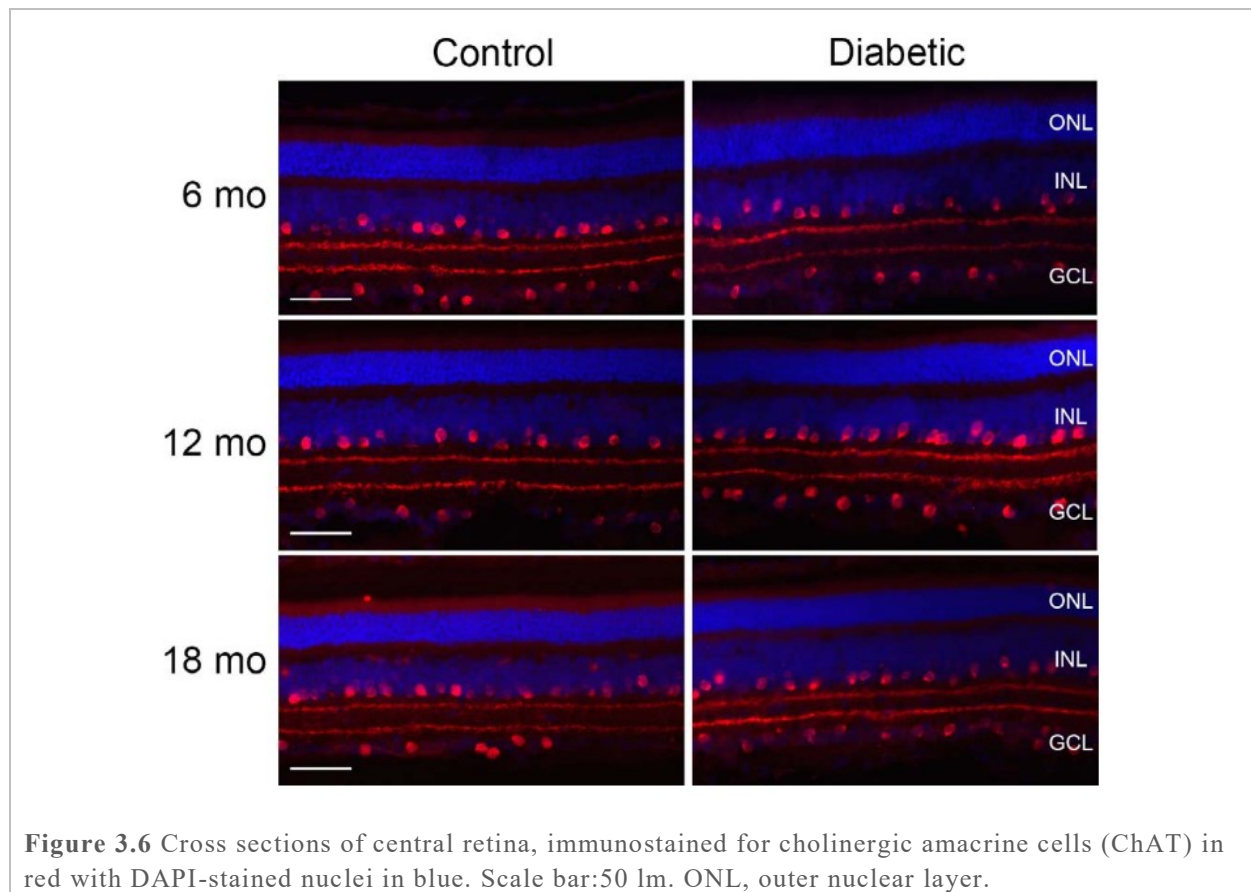
No differences were observed in a- and b-wave amplitudes or implicit times between diabetic and control animals at 18 mo, regardless of the adaptation background studied (scotopic, mesopic or photopic). Finally, b-wave amplitudes were quantified at time 0 versus 10 min. after switching background adaptation from scotopic to mesopic, as well as from mesopic to photopic and again no changes were observed.

No evidence of either retinal edema or thinning was observed in diabetic animals from 6 to 18 mo at any eccentricity (**Figure 3.6**). Outer and inner nuclear layer measures taken from the central and peripheral retina did not differ between groups (**Table 3.3**). Cholinergic amacrine (ChAT-immunoreactive) total cell numbers, both in the inner nuclear layer (INL) as well as those displaced in the ganglion cell layer (GCL), were unchanged (**Table 3.3**).

Table 3.3 Central and Peripheral Retina Outer and Inner Nuclear Layer Thickness Measures and ChAT-Immunoreactive Amacrine Cell Counts

		6 mo		12 mo		18 mo	
		Control	Diabetic	Control	Diabetic	Control	Diabetic
Center	ONL thickness, μm	29.1 \pm 4.9, n = 4	30.9 \pm 2.9, n = 3	28.5 \pm 3.5, n = 6	30.4 \pm 2.8, n = 6	28.8 \pm 5.0, n = 6	29.3 \pm 2.8, n = 6
	INL thickness, μm	37.6 \pm 3.8, n = 4	39.5 \pm 6.8, n = 3	36.8 \pm 4.7, n = 6	39.5 \pm 5.1, n = 6	38.8 \pm 7.7, n = 6	37.1 \pm 3.8, n = 6
	ChAT+ cells	24 \pm 4, n = 4	27 \pm 4, n = 3	28 \pm 5, n = 6	30 \pm 5, n = 6	24 \pm 5, n = 4	29 \pm 4, n = 6
Periphery	ONL thickness, μm	21.5 \pm 3.8, n = 4	22.9 \pm 2.3, n = 3	19.2 \pm 2.2, n = 6	23.4 \pm 1.8, n = 6	20.9 \pm 3.4, n = 6	22.3 \pm 2.7, n = 6
	INL thickness, μm	25.0 \pm 6.8, n = 4	23.2 \pm 2.2, n = 3	22.4 \pm 5.9, n = 6	25.0 \pm 3.6, n = 6	26.7 \pm 4.7, n = 6	27.6 \pm 4.2, n = 6
	ChAT+ cells	16 \pm 4, n = 4	18 \pm 4, n = 3	18 \pm 4, n = 6	17 \pm 3, n = 6	20 \pm 4, n = 4	22 \pm 5, n = 6

Values indicate average \pm standard deviation.



Likewise, no differences were detected in retinal flatmounts stained with specific oxidative/nitrative stress markers (*Figure 3.7*). Very low levels of extravascular lipid oxidative modifications were demonstrated using 4-hydroxynonenal specific antibodies (12 mo only); the retinal vasculature was devoid of any detectable immunoreactivity. The nitrative stress marker, nitrotyrosine, was detected at low levels in blood vessels of both groups at 2 mo. This vascular staining was exacerbated at 12 mo in both central and peripheral retina but did not differ between groups.

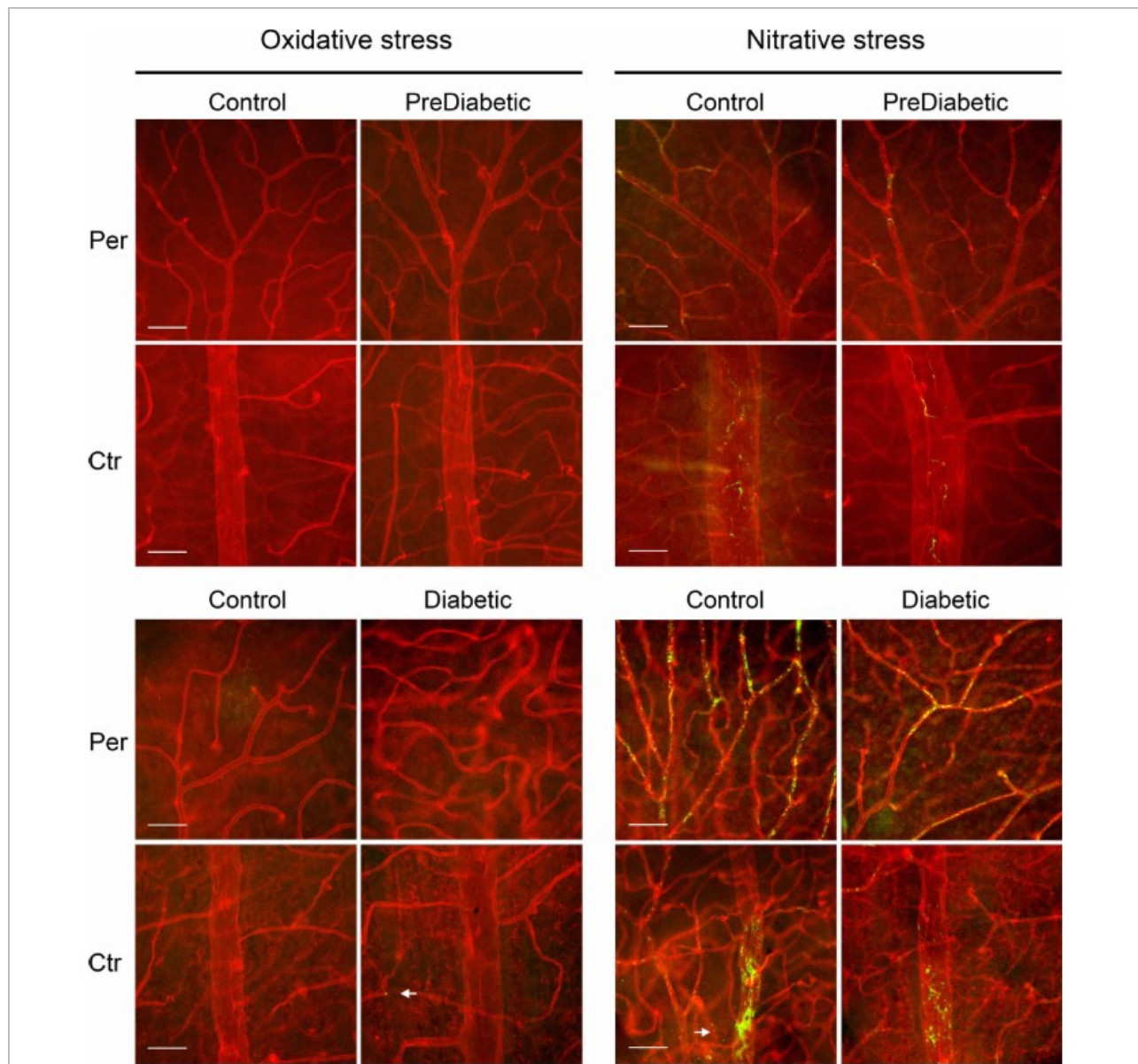


Figure 3.7 Retinal flatmounts of blood vessels (2 months, top; 12 months, bottom) stained for oxidative (4-hydroxynonenal) and nitrate (nitrotyrosine) stress in green. Tomato lectin staining of vasculature in red. Extravascular immunoreactivity for stress markers (white arrows). Scale bar: 50 μ m. Ctr, center; Per, periphery.

3.3.4 Cataracts of increasing severity

Fluorescein angiography (FA) was performed to assess inner retinal vasculature. Imaging of diabetic animals was limited due to impedance by cataract formation. Clearly evident in the eyes of diabetic animals (*Figure 3.8A*; lens only *Figure 3.8B*), cataracts exhibited a range of severity (*Figure 3.8C-I*), illustrating the barrier to examining retinal blood vessels *in vivo* (*Figure 3.8D-J*). Incidence increased from 13% at 12 mo, to 50% at 18 mo. Cataracts were never detected in controls at any of the ages examined. Although, rarely observed, evidence of a microaneurysm in an 18 mo diabetic Nile rat is presented in *Figure 3.8F* (inset).

3.4 DISCUSSION

The present study establishes that high-resolution respirometry (with a multiple substrate-inhibitor-titration protocol to assess individual respiratory

Complex function) can be applied to isolated retinæ. Furthermore, unlike the other approaches such as Seahorse¹⁸⁷, high-resolution respirometry allows the normalization of results as FCR

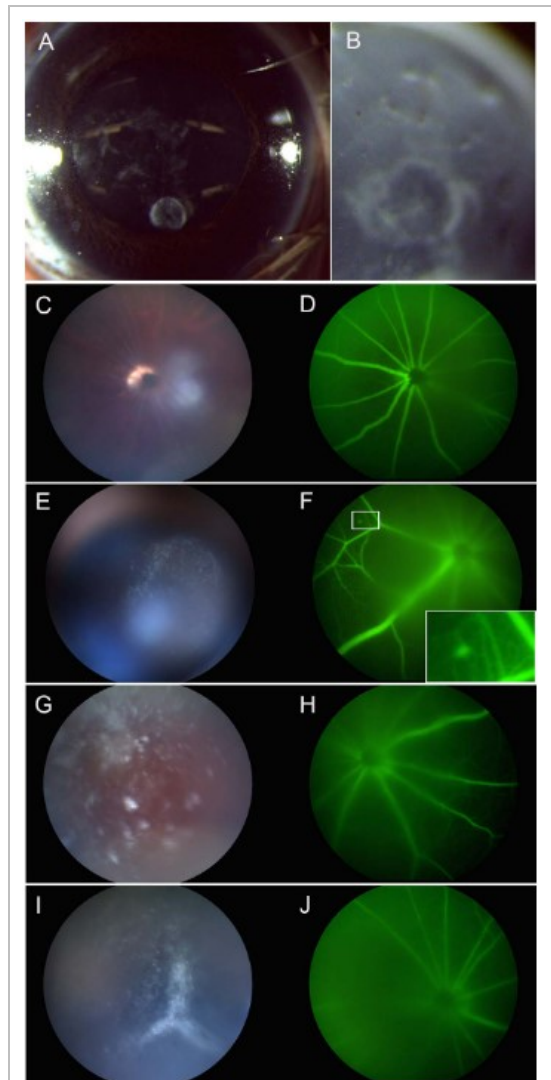


Figure 3.8 Example of cataractogenesis in 18-month hyperglycemic Nile rats. Enucleated eye (A) with isolated lens (B). Representative fundus images of increasing cataract severity (C, E, G, I) with corresponding fluorescein angiography image (D, F, H, J). Inset in (F) demonstrates a microaneurysm.

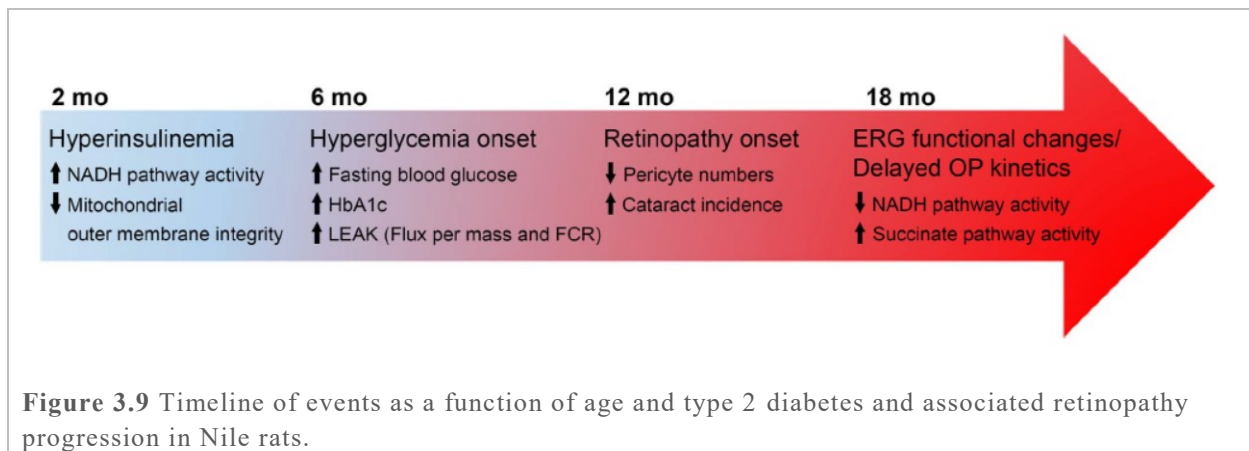
values, which is crucial to accurately detect modest changes, and also allows many titration protocols to be performed in a single experiment. We show evidence of well-coupled mitochondria in tissue homogenates, which allowed us to identify changes in oxidative phosphorylation and breaches in outer membrane integrity during insulin resistance (2 mo), prior to the manifestation of hyperglycemia (6 mo), in *Arvicanthis niloticus* (Nile rat). In addition, we provided evidence of delayed OPs (specific to the cone pathway) and increased incidence of cataractogenesis after prolonged hyperglycemia in retinas of this cone-rich diurnal rodent model, which recapitulates the five stages of human T2D progression⁸⁹ (**Figure 3.9**). A key target in the development of DR is the synergistic interaction between neurons (amacrine and retinal ganglion cells), glial cells (Müller cells and astrocytes) and blood vessels (endothelial cells and pericytes) involved in the autoregulation of vascular flow and metabolic activity¹⁸⁸. Dysregulation of this "neurovascular unit" has been implicated in diabetes, in part due to oxidative stress originating from the outer retina⁷⁸, and well before onset of clinically detectable DR¹⁸⁹. According to Kooragayala et al.¹⁸⁹, photoreceptors have limited mitochondrial reserve capacity for ATP production from their electron transport system. Therefore, photoreceptors are particularly vulnerable to changes in homeostasis. Fort et al.¹⁹⁰ observed that during the initial stages of type 1 diabetes, the retina compensates by lowering its constitutively high metabolic activity. Reductions in retinal electrical activity¹⁹¹, biosynthetic activity¹⁹², increases in autophagic flux in the outer plexiform layer¹⁹³, and even apoptosis of marginal populations of neural and vascular cells¹⁹⁴ are all contributors. However, these mechanisms eventually fail, leading to the first clinically detectable signs of DR, specific to inner retina microvasculature: capillary basement

membrane thickening and pericyte loss. Our results support that changes in mitochondrial function and integrity occur early and likely contribute to transient compensation in an attempt to maintain energy homeostasis.

Increased respiration at 2 mo, as a result of exogenous cytochrome *c* entering the intermembrane space, indicates changes in mitochondrial membrane properties (such as composition and/or organization). Surprisingly, this transient increase in outer membrane permeability was associated with an increase in NADH-pathway (Complex I and related dehydrogenases) contribution to maximal OXPHOS capacity, whereas it is generally associated with defects in mitochondrial respiratory complexes.^{92,195} At the onset of hyperglycemia (6 mo), we observed increases in LEAK and decreases in cytochrome *c* access to mitochondrial respiratory complexes without paradoxical increases in NADH-pathway activity. One possible explanation would be that early changes in mitochondrial function and integrity might entice transient compensation for the maintenance of energy homeostasis. Changes in mitochondrial membrane composition take several months to develop¹⁹⁶⁻¹⁹⁸ and may explain the improved membrane integrity observed in 6 mo diabetic animals, with no further changes at 18 mo.

Mitochondria were well-coupled in prediabetic animals, without decreased respiratory capacity, emphasizing the specificity of this change in membrane sensitivity in retinal mitochondria. These early changes did not correlate with fasting plasma insulin levels. Increased mitochondrial membrane permeability was documented in isolated mitochondria from retinas of ZDF (Zucker diabetic fatty) rats during hyperinsulinemia (prior to hyperglycemia), but alongside a decrease (rather than an increase) in Complex III activity¹⁹⁹. Decreases in Complex III activity

(without changes in Complex I) were also reported in STZ mice⁵⁹. Respiration in the presence of substrates feeding electrons into Complex I (NADH-pathway), II (Succinate-pathway) or I and II also involves Complex III and IV, and so a decrease in Complex III would cause a decrease in maximal OXPHOS capacity, which was not observed in our study. The above differences between animal models epitomizes the debate about whether changes in mitochondrial capacity are causal or consequential to insulin resistance^{181,200,201}. Such discrepancies between models and studies might in fact provide pertinent insight into the intricate relationship between mitochondria and insulin action, and subsequently effective preventative targets.



Enhanced NADH-pathway contribution to maximal OXPHOS capacity in retinas is reminiscent of data on cardiac mitochondria showing an increase in mitochondrial oxidation of palmitoyl carnitine, glutamate, and succinate in insulin resistant mice²⁰¹, and an increase in oxidation of palmitoyl-CoA and octanoylcarnitine, as well as in Complex I activity, at early stages of diabetes in fructose-fed rats²⁰². Complexes I, II and III have the highest capacity for

superoxide production²⁰³, therefore, decreases in their activity (albeit associated with maintenance of respiratory complex flux) would lead to excessive free radical production. In fact, most mitochondria produce superoxide high rates after addition of the Complex I inhibitor rotenone^{203,204}, and furthermore, several pathologies involving defects in Complex I are associated with elevated production of superoxide^{205,206}. Therefore, the initial increase in relative contribution of electron flow through Complex I observed during prediabetes (2 mo) could represent a compensatory mechanism serving to reduce the production of reactive oxygen species. In contrast, at 18 mo of age, after one year of hyperglycemia, reduced NADH-pathway capacity suggests pathology as a result of oxidative stress. However, the age-related changes previously reported in other tissues (reduced CS activity and decrease in the activity of mitochondrial complexes)^{207,208} were not observed in Nile rat retinas at 18 mo, regardless of their diabetic status. We failed to detect upregulation of targeted oxidative/nitrative stress markers in retinal vasculature of either prediabetic (2 mo) or diabetic animals (up to 12 mo) relative to controls. Our main focus with limited starting material was to examine the vasculature for 4-HNE (marker of aldehydic products of lipid peroxidation) and nitrotyrosine formation specifically as a possible cause of pericyte dropout, using an approach that successfully demonstrated upregulation of oxidative/nitrative stress in whole mounted retinas (STZ rat model)²⁰⁹. Our high-resolution respirometry results support these findings. We cannot rule out that examination of additional markers (and/or later time points) may have demonstrated oxidative stress in the vasculature. Assuming that oxidative stress would have occurred in the retina, then the expected outcome would have been a decrease (and not an increase as observed

here) in NADH-pathway activity^{203–205}. In STZ rats, at early stages (1-3 weeks post-induction) retinal mitochondria have been shown to undergo adaptive changes associated with maintained energetic requirements and prevention of oxidative stress²¹⁰. However, at later stages (after 8-12 weeks post-induction), upregulation of oxidative stress markers was reported²⁰⁹. STZ rats are characterized by hyperglycemia due to insufficient insulin secretion (T1D model), whereas Nile rats undergo hyperinsulinemia without initial hyperglycemia (T2D model). While STZ studies show adaptive mitochondrial changes at early stages of hyperglycemia (without elevated insulin levels), the mitochondrial changes reported here in Nile rats precede manifestations of DR.

Well-established clinical indicators of early DR, oscillatory potentials^{80,211}, were affected at 18 mo in diabetic Nile rats; implicit times were prolonged while amplitudes were preserved. Of interest, Morlet wavelet transform failed to detect implicit time delays in this study. Morlet is limited to time domain analysis of the largest amplitude oscillatory components and these OPs were not delayed. Similar findings were reported in early human DR and in animal models where delays in OPs also preceded changes in their amplitudes^{212,213}. Using a mouse model of T2D (high-fat diet), Rajagopal et al.²¹⁴ reported delayed OP timing as the first functional retina phenotype, coinciding with the peak of insulin resistance (6 mo). Once hyperglycemia developed (by 12 mo), amplitudes became reduced, alongside microvascular changes. However, a- and b-waves (amplitudes and latencies) were unaltered²¹⁴, as was the case in diabetic Nile rats. Our findings support previous evidence that changes in OPs precede those in b-waves²¹⁵. One major difference with mouse and rat models is that alterations in OPs in these nocturnal rodents were detected under scotopic adaptation. Interestingly, we only observed alterations in OPs when

recorded under photopic adaptation, which could be related to the higher proportion of cones in Nile rats (35%)²¹⁶ compared to rats and mice (1-3%)^{217,218}. Our observation of preserved OP amplitudes is in agreement with the preserved total number of cholinergic amacrine cells, which likely contribute to OP generation together with other inner retina neurons²¹⁹. Studies in induced and spontaneous diabetes type 1 diabetic rodent models (STZ rats and Ins2^{Akita} mice, respectively) reported the loss of both cholinergic and dopaminergic amacrine cells; however ERG recordings were not performed²²⁰. Other studies on STZ models reported defects in a-waves, but whether these reflect impaired photoreceptor response to light due to hyperglycemia²²¹ or a direct toxic effect of STZ²²² remains unclear. Our ERG results therefore further support that DR is at its earliest stage of manifestation in Nile rats. The lack of changes in a-wave amplitudes and implicit times in our study, implies that changes in photoreceptor metabolism likely contribute to DR initiation⁷⁸, without early concomitant changes in photoreceptor response to light flashes.

The 50% incidence of cataracts in diabetic Nile rats, at this time point is similar to the high incidence reported in T2D patients²²³.

Pericyte loss was preferential to the subtype lining straight capillaries as previously reported in the Ins2^{Akita} mouse model of type 1 diabetes²²⁴, as opposed to pericytes lining forked capillaries or bridging adjacent capillaries. While the underlying mechanisms elude us, one avenue warranting scrutiny is the potential for hyperglycemia to alter the types of integrins expressed on specific pericytes, and hence modulate their response to pro-apoptotic ligands such as angiopoietin-2²²⁵. Recent *in vitro* studies by Zhang et al.²²⁶ have demonstrated increased levels of autoantibodies against pericyte cell surface antigens in the serum of DR patients. Of

interest in terms of the Nile rat's pertinence as a DR model, the ratio of total pericytes over endothelial cells (at 6 mo, prior to any cell loss) was close to 1:1, as observed in humans²²⁷, which contrasts with the 1:3 ratio reported in rats²²⁸. Degenerated capillaries were only observed at the latest time point (18 mo), consistent with DR progression^{166,229,230}.

Control animals do not become hyperglycemic up to 18 mo, but they do demonstrate hyperinsulinemia from 6 mo onward, which alone is not associated with DR. Harris and colleagues⁷⁴ estimated that T2D likely develops over 12 years (and retinopathy over 7 years) prior to a clinical diagnosis of T2D. Our results from high-resolution respirometry support that early mitochondrial function changes might be part of these insidious changes that precede clinical detection of T2D and therefore, DR.

One major limitation to characterizing retinal mitochondrial change during the development of diabetes (and other insults) is the limited amount of tissue. Examples of specific changes that could not be directly assessed in our broad-scope study include: 1) complementary assays to measure oxidative stress directly in isolated mitochondria; 2) specific content analysis of mitochondrial external membranes (such as phospholipid types and cardiolipin); and 3) direct measures of Complex III activity using spectrophotometric assay for this protein. Although indirect, our overall data did not support a potential defect in Complex III.

3.5 CONCLUSION

There is overwhelming experimental evidence linking hyperglycemia with pericyte loss and development of microvascular complications in early DR¹⁹⁴. Application of high-resolution

respirometry, with a multiple substrate-inhibitor-titration protocol, allowed detection of early onset retinal changes in the Nile rat T2D model. Hyperinsulinemia is associated with increased contribution of NADH-pathway to oxidative phosphorylation and with compromised outer membrane integrity. The diet-based difference between groups is of particular relevance as it offers the potential to mimic clinical interventions aimed at reversing hyperglycemia itself, such as with diet or metformin. A key challenge is to understand why in some patients, even with hyperglycemia reversal, progression to retinopathy continues. This model would be a valuable tool to examine whether hyperinsulinemia alone might "program" retinopathy onset.

4 PHOTORECEPTOR-INDUCED RPE PHAGOLYSOSOMAL MATURATION DEFECTS IN STARGARDT-LIKE MACULOPATHY

4.1 INTRODUCTION

Mutations in ELOVL4, responsible for a dominant maculopathy (Stargardt-like, STGD3), lead to an enzymatically inactive truncated protein lacking its C-terminal endoplasmic reticulum retention signal²³¹. Unfolded protein response (UPR) alone should initiate death in cells expressing the truncated ELOVL4 protein, as occurs in cell lines (COS-7 and HEK-293 cells)²³². However, transgenic mice expressing mutant ELOVL4 in their photoreceptors do not display evidence of UPR until advanced cell death^{99,233}. Furthermore, loss of ELOVL4 elongase activity¹⁰⁰, essential for the synthesis of very long chain polyunsaturated fatty acids (VLC-PUFAs, of 28–36 carbon chains)⁹⁹, does not cause retinal degeneration in STGD3^{99,234}.

The mechanisms initiating retinal degeneration in STGD3 still elude us and are the subject of intense debate. Human mutant ELOVL4 mislocalizes to outer segments when expressed in the photoreceptors of *Xenopus laevis*²³⁵; whether it also mislocalizes to the much thinner outer segments of mice has yet to be elucidated. A major hurdle is the inability to generate an antibody specific to the truncated ELOVL4 protein. Furthermore, while ELOVL4 transgenic mice have been studied in detail, this model does not express a tag on the transgene. We previously described that transgene expression in photoreceptors lead to perturbations in disc membrane ultrastructure and signs of RPE cell toxicity, prior to cell death²³⁶. A clinical hallmark of STGD3 is the accumulation of a toxin, lipofuscin (a non-enzymatic by-product of vitamin A aldehyde),

formed in photoreceptors and transferred to RPE cells through daily outer segment phagocytosis, which exerts deleterious effects on the RPE²³⁷.

One hypothesis receiving increasing scrutiny is that for cells expressing a mutant protein to die, these cells must first alter the physiology of other cell types²³⁸. Survival requirements of highly specialized neurons involve interactions with supporting cells. Photoreceptor survival depends on the daily shedding and degradation of their outer segments (POS) by adjacent RPE cells²³⁹. Sequential steps including recognition, ingestion and degradation, are involved. Defects in any of these cellular processes lead to photoreceptor death. Impaired outer segment tip recognition leads to the accumulation of lipofuscin in the RPE and of toxic debris in the subretinal space²⁴⁰. Defects in ingestion, cause dry AMD-like phenotypes²⁴¹. Finally, defective lysosomal degradation of POS content, as reported in mice lacking Cathepsin D²⁴² or expressing mutant beta-crystallin A1/A3²⁴³, is associated with increased lipofuscin levels, which have been reported to impede lysosomal function in AMD²⁴⁴. In Stargardt hereditary maculopathies, and the more common age-related macular degeneration that affects close to 200 million worldwide²⁴⁵, photoreceptor death and vision loss is preceded by asymptomatic RPE defects.

Previous findings in the transgenic ELOVL4 (TG1-2) mouse showed signs of RPE toxicity *in vivo* (disorganization of apical villi and vacuolization) at one month of age, followed at 2 months by photoreceptor cell death onset, and at 3 months by phagocytic defects (delayed phagosome movement, undigested outer segments and lipid deposits)²³⁶ and increased A2E levels²⁴⁶. This study examines how RPE cells are affected by the expression of mutant ELOVL4 in photoreceptors, prior to cell death.

4.2 METHODS

4.2.1 Animals

The animals used in this study were heterozygous transgenic ELOVL4 (TG1-2; TG) and wild-type (WT) littermate mice bred from a colony maintained at the University of Alberta, originally derived from the TG2 line generated by Karan et al.²⁴⁷, but with transgene expression levels comparable to the TG1 line²⁴⁶. All mice were culled at one month of age, with the exception of photoreceptor outer segment isolation, which gave optimal yield when using 2 month-old mice (due to larger eye size). Timing of light onset and subsequent tissue collection was strictly controlled to examine specific time points in relation to the peak of phagocytosis (2 hours into daylight cycle)⁴³. They were housed under a 14:10 light-dark cycle, at $21 \pm 2^\circ\text{C}$, relative humidity 40% with ad libitum access to Laboratory Rodent Diet (5021; LabDiet®, Nutrition Intl., Richmond, IN) and water. All procedures were approved by the University of Alberta Animal Care and Use Committee (ACUC, license AUP00000328) and were conducted in accordance with the ARVO (Association for Research in Vision and Ophthalmology) Statement for the Use of Animals in Ophthalmic and Vision Research.

4.2.2 Cell culture

ARPE-19 human stable cells (ATCC® CRL2302™) were cultured to optimize native phenotypes²⁴⁸. Post-confluent cultures in T75 flasks (353136, Falcon) were maintained in DMEM-F12 (11330-032, Gibco) supplemented with 100 U/mL penicillin, 100 µg/mL streptomycin (15140-122 Gibco) and 10% fetal bovine serum (Canadian origin, F1051, Sigma-

Aldrich) at 37°C in a humidified atmosphere of 5% CO₂. Cells were split 1:2 every 4 weeks to allow epithelial phenotype maintenance²⁴⁹. Under these conditions, ARPE19 cells recapitulated all steps of OS phagocytosis, but with slower kinetics than in primary RPE cultures, as previously reported by Mazzoni et al²⁵⁰. We followed their recommendations of 2–5 h as being optimal in cell lines for POS challenge (as opposed to 30 min to 2 h for unpassaged primary rat or mouse cell lines).

4.2.3 Isolation of photoreceptor outer segments

Mouse photoreceptor outer segments (POS) were prepared using OptiPrepTM density gradient medium (D1556, Sigma-Aldrich) as previously described²⁵¹. *In vitro* quantification of POS phagocytosis by human RPE cells was performed as previously described²⁵². In brief, eyes were dissected under dim red light and retinas collected in 120 µL ice-cold 8% OptiPrepTM diluted in Ringer's buffer, then vortexed at maximum speed for one minute, centrifuged at 200 x g for one minute and the supernatant was collected. This procedure was repeated five times to collect 700 µL of crude extract which was then loaded on a 10% and 18% OptiPrepTM step gradient in Ultra-ClearTM centrifuge tubes (347356, Beckman Coulter). Following centrifugation (30 minutes at 26,500 x g), the orange band containing POS on top of the 18% OptiPrepTM was collected, diluted with four volumes of Ringer's buffer and centrifuged at 500 x g for 3 minutes. The supernatant was transferred into a clean tube, centrifuged (26,500 x g for 30 minutes), the pellet collected and resuspended in 8% OptiPrepTM to a final concentration of 1x10⁷ POS/mL and stored at -80°C. Just before use, POS were labelled with 1% (v/v) Alexa Fluor 488 carboxylic acid succinimidyl ester (A20000, Molecular Probes, 15 mM) for one hour on ice, rinsed three

times with PBS and finally resuspended in DMEM-F12 medium (11330-032, ThermoFisher Scientific) supplemented with 1% FBS (F1051, Sigma-Aldrich). POS concentration was verified by direct counting on a hemocytometer.

4.2.4 Phagocytosis assay

Post-confluent stationary human RPE cells were seeded at a confluence of 20,000 cells per well in Nunc® MicroWell 96 well optical bottom plates (P8991, Sigma-Aldrich) and cultured for 2 weeks in DMEM-F12 medium (11330-032, ThermoFisher Scientific) supplemented with 1% FBS (F1051, Sigma-Aldrich). To quantify the binding and internalization of POS, cells were fed with Alexa-Fluor 488 labelled POS (10 POS per cell) and incubated for 30, 60, 90 and 120 minutes at 37°C. Cells were then rinsed twice with ice-cold Dulbecco's phosphate-buffered saline, no calcium, no magnesium (DPBS-CM, 14190-144, ThermoFisher Scientific). A subset of the wells were incubated with ice-cold trypan blue 0.4% for 10 minutes to quench the fluorescence derived from externally bound particles, and rinsed twice with ice-cold DPBS-CM. POS processing by human RPE cells was studied using pulse-chase assays. Following 2 hours incubation with Alexa-Fluor 488 labelled POS, cells were rinsed twice with growth medium to remove the unbound POS and the cells were then return to 37°C for chase periods of 4, 8, 15, or 24 hours. Human RPE cells were fixed 10 minutes with ice-cold methanol and counterstained with ethidium bromide. Fluorescence signals were quantified in duplicate wells using a Typhoon Trio scanner (GE Healthcare). POS fluorescence was normalized using ethidium bromide fluorescence.⁵⁰ Mann-Whitney U-test (one-tailed) was used with significance set to $P \leq 0.05$; $n =$

3-5 independent experiments. For each individual experiment, POS were isolated from 26 pooled retinas per group.

4.2.5 Live imaging of LysoTracker-labelled phagolysosomes.

Phagolysosomes were stained and imaged as previously described.¹⁹ Freshly dissected posterior eyecups were incubated at 37°C for 15 minutes in DMEM (11995-065, Gibco) with 0.4 µM LysoTrackerTM Red DND-99 (L7528, Molecular Probes) to label acidified phagolysosomes and 5 µM 4',6-Diamidino-2'-phenylindole dihydrochloride (DAPI) to stain nuclei. Confocal images (z-stacks, 0.3 µm steps, 30 µm in total) were captured in the central part of the RPE, using an Olympus IX-81 inverted microscope equipped with a Yokagawa CSU X1 spinning disk confocal scan-head, a Hamamatsu EMCCD camera (C9100-13). The volume occupied by phagolysosomes inside individual RPE cells was calculated using VolocityTM software (version 6.3, PerkinElmer). RPE cells were imaged from 8 independent experiments (4 WT and 4 TG animals) and a total of 13 microscope fields per group (3-4 images per animal), representing 297 and 331 RPE cells from WT and TG animals respectively, for final analysis. Mann-Whitney U-test (one-tailed) was used; significance was set to $P \leq 0.05$.

4.2.6 Nuclear and cytoplasmic TFEB localization by western blotting.

Nuclear and cytoplasmic proteins were isolated from freshly dissected posterior eyecups (RPE/choroid) using the NE-PER Nuclear and Cytoplasmic Extraction Reagent kit (#78833, ThermoFisher Scientific) according to the manufacturer instructions. Animals were culled 2 hours after light onset and homogenized tissues from 3-4 animals were pooled. Nuclear and

cytoplasmic extracts were kept at -80°C until use. Protein levels were determined (Pierce BCA protein assay kit, PI-23227, ThermoFisher Scientific). After addition of 4X Laemmli sample buffer (161-0747, BioRad) with 2-mercaptoethanol (2.5% final conc.), samples were boiled for 5 minutes, 2 µg total protein (nuclear extract) or 5 µg total protein (cytoplasmic extract) were loaded per lane on 10% SDS-PAGE gels, run at 200 V constant voltage for 60 minutes, and then transferred to PVDF membranes. After blocking for 1 hour in 5% skim milk powder in TBS-T (20 mM Tris, 137 mM NaCl, pH 7.6 with 0.1% Tween-20), membranes were incubated overnight with rabbit polyclonal anti-TFEB (1:5000, A303-673A, Bethyl Laboratories) diluted in block solution. The following day membranes were washed 3 x 10 minutes in TBS-T and incubated for 1 hour with anti-rabbit IgG HRP-conjugated antibody (1:5000 in block; NA934, GE Healthcare) as before. Then membranes were washed 2 x 10 minutes in TBS-T, 2 x 5 minutes in TBS (no Tween-20), and visualized with Clarity™ Western ECL substrate (170-5060 BioRad) on a ChemiDoc™ Touch Imaging System (BioRad). ImageLab version 5.2.1 software (BioRad) was used to determine volume (intensity) of bands (samples loaded in duplicate, 2 independent experiments). Isolation of cytoplasmic and nuclear proteins specifically was verified using PCNA (1:500, rabbit polyclonal, ab2426, Abcam) and TUBA (1:500, mouse monoclonal, sc-8035, Santa Cruz), respectively. Total protein loading and transfer was verified by staining the blot with GelCode® Blue stain reagent (24590, ThermoFisher Scientific). TFEB signal was measured in duplicate wells for each sample and the ratio of cytoplasmic over nuclear TFEB (for 5 µg of total protein) was calculated in two independent experiments.

4.2.7 RPE flatmounts and immunohistochemistry

After light 4% PFA fixation and sucrose cryoprotection, eyecups (cornea and lens removed) were embedded in OCT (Tissue-Tek, Sakura® Finetek) and stored at -80°C until flatmount preparation. After eyecups were washed in PBS and flattened with four radial cuts, whole retinas were gently removed. RPE flatmounts were blocked for 1 hour in PBS with 0.3% Triton X-100, 0.1% Tween-20, and 5% bovine serum albumin and then reacted overnight at 4°C with primary antibodies diluted in same: rabbit polyclonal anti-TFEB (1:500, A303-673A, Bethyl Laboratories); or rabbit polyclonal anti-IBA-1 (1:400, 019-19741, Wako). F-actin was detected by incubation with Alexa Fluor 488 Phalloidin (1:40, A12379, Molecular Probes) for 30 minutes. After extensive PBS washes, RPE flatmounts were incubated for 2 hours with 10 µg/mL Hoechst (Bisbenzimidazole, H33258, Sigma-Aldrich) and 1:1000 species appropriate Alexa Fluor labelled secondary antibodies (Molecular Probes). RPE flatmounts were washed as before, then coverslipped and mounted with Vectashield mounting media (H-1000, Vector Laboratories). TFEB immunoreactivity was evaluated on the central part of the RPE flatmount (mice were culled 3 hours after light onset). Total numbers of IBA-1 positive cells were counted. Mann-Whitney U-test was used; significance was set to $P \leq 0.05$, with $n = 4$ animals per group.

4.2.8 cDNA synthesis and quantitative RT-PCR.

Total RNA was isolated immediately following RPE and retina dissection. RNA was reverse transcribed and cDNA quantified using real-time PCR. All details regarding nucleic acid extraction, reverse transcription, qPCR assay settings and validation in adherence with MIQE

guidelines are respectively described in supplementary Tables 1 and 2. Expression of CLEAR genes (*Tfeb*, *Map1lc3a*, *Atp6v0a1* and *Ctsd*), chemokine genes (*Ccl2*, *Ccl5*) and crystallin family genes (*Cryaa*, *Cryab*, *Cryba1*, *Cryba4*, *Crybb2*, *Cryga* and *Crygs*) was normalized to the reference gene *Hprt*. Student's t-test and Mann-Whitney U-test were used appropriately. Data are presented as mean \pm SEM. Significance was set to $P \leq 0.05$; n = 5-10 animals per group.

4.2.9 RPE cell protein preparation and western blotting.

For LC3B-I/LC3B-II, cathepsin D and beta-crystallin A1/A3 western blots, animals were culled 3 hours or 5 hours after light onset (n = 4-5 animals). Proteins were prepared from isolated RPE as previously described (confirmed RPE markers with an absence of choroid markers²⁵³).

Briefly, after removing neural retina, four slits were made in the posterior eyecup and the flattened tissue was immersed in 100 μ L RIPA lysis buffer (R0278, Sigma-Aldrich) with HALT™ Protease inhibitor cocktail (87786, ThermoFisher Scientific) on ice. Each tube was tapped 20 times and returned to ice, and this was repeated 5 times in total (100 taps each to release RPE). After incubation on ice for a maximum of 20 minutes (to prevent choroid contamination), choroid/sclera was discarded, and RPE from individual animals was pooled (200 μ L per tube). Samples were then sonicated 2 x 10 seconds on ice. After centrifugation, 14,000 rpm for 15 minutes at 4°C, supernatants were collected and stored at -80°C until use. Protein concentrations were measured and 10 μ g of total protein per lane were analysed on 12% SDS-PAGE gels and PVDF membranes as described in the previous section. Membranes were incubated overnight with LC3B (1:1000, rabbit polyclonal, 2775, Cell Signaling Technology),

cathepsin D (1:500, goat polyclonal, sc-6486, Santa Cruz) or beta-crystallin A1/A3 (1:5000, rabbit polyclonal, PA5-28954, ThermoFisher Scientific), diluted in block solution. Membranes were washed, incubated 1 hour with anti-rabbit or anti-goat IgG HRP-conjugated antibody (1:5000 in block solution; NA934, GE Healthcare; sc-2354 Santa Cruz, respectively), washed again and imaged as described before (samples loaded in duplicate, 2 independent experiments). Protein levels were normalized to α -tubulin (TUBA, 1:500, mouse monoclonal, sc-8035, Santa Cruz) loading control.

4.2.10 Mass spectrometry

Posterior eyecups (RPE/choroid) collected from TG and WT (n = 6-8 each per experiment, run in duplicate) were pooled and homogenized in sample lysis buffer (20 mM Tris HCl, pH 7.5; 150 mM NaCl; 1 mM EGTA; 1% Triton X-100, HALT™ Protease inhibitor cocktail, 87786, ThermoFisher Scientific). After 30 minutes at 4°C, samples were passed repeatedly through a 26-gauge needle, centrifuged 5 minutes at 4°C and supernatants were frozen at -80°C until use. Protein levels were determined (Pierce BCA protein assay kit, PI-23227, ThermoFisher Scientific). After addition of 2% (vol/vol) 2-mercaptoethanol and 1% (vol/vol) saturated bromophenol blue, samples were boiled for 5 minutes, 20 μ g total protein was loaded per lane on 12% SDS-PAGE gels, and gels were run at 200 V constant voltage for 45 minutes. Gels were western blotted for beta-crystallin A1/A3 as described above. Duplicate gels were washed in ultrapure water (3 x 5 minutes), stained for one hour with GelCode® Blue stain reagent (24590, ThermoFisher Scientific), and rinsed with ultrapure water. Mass spectrometry was performed by

the Alberta Proteomics and Mass Spectrometry Facility (Department of Biochemistry, Faculty of Medicine & Dentistry, University of Alberta).

Excised gel lanes were de-stained twice in 100 mM ammonium bicarbonate, acetonitrile (50:50). The samples were then reduced (10 mM β ME in 100 mM bicarbonate) and alkylated (55 mM iodoacetamide in 100 mM bicarbonate). After dehydration, in-gel trypsin digestion was allowed to proceed overnight at room temperature. Tryptic peptides were first extracted from the gel using 97% water, 2% acetonitrile, 1% formic acid followed by a second extraction using 50% of the first extraction buffer and 50% acetonitrile. Fractions containing tryptic peptides were resolved and ionized by using nanoflow HPLC (Easy-nLC II, ThermoFisher Scientific) coupled to an LTQ XL-Orbitrap hybrid mass spectrometer (ThermoFisher Scientific). Nanoflow chromatography and electrospray ionization were accomplished by using a PicoFrit fused silica capillary column (ProteoPepII, C18) with 100 μ m inner diameter (300 \AA , 5 μ m, New Objective). Peptide mixtures were injected onto the column at a flow rate of 3,000 nL/minutes and resolved over 60 minutes at 500 nL/minutes using linear gradients from 0 to 45% v/v aqueous ACN in 0.2% v/v formic acid. The mass spectrometer was operated in data-dependent acquisition mode, recording high-accuracy and high-resolution survey Orbitrap spectra using external mass calibration, with a resolution of 30,000 and m/z range of 400–2000. The fourteen most intense multiply charged ions were sequentially fragmented by using collision induced dissociation and spectra of their fragments were recorded in the linear ion trap; after two fragmentations all precursors selected for dissociation were dynamically excluded for 60 seconds.

Raw data were processed using the proteomic platform MaxQuant version 1.5.8.2 (<http://maxquant.org>) with the computational workflow designed for quantitative label-free proteomics⁵¹ and data were analysed with Perseus version 1.5.8.5. Raw MaxQuant files were searched against Uniprot *Mus musculus* reference proteome database (UP000000589, strain C57BL/6J). Data were filtered to keep only proteins detected in all samples. Label-free quantification (LFQ) methodology was used to compare the levels of identified proteins between TG and WT. To estimate the abundance of identified proteins, LFQ intensities were transformed by Log_2 to fit a normal distribution then subjected to hierarchical clustering and presented as multiscatter plots.

4.2.11 High-resolution respirometry

To provide a sensitive measure of oxidative stress and assess the bioenergetics status of RPE cells (essential for phagocytosis), high-resolution respirometry (Oxygraph 2k, OROBOROS Instruments, Innsbruck, Austria) was performed on freshly isolated TG and WT eyecups (2 littermates/4 eyecups pooled per measurement), $n = 8$ measurements for each genotype, with slight modification from the method previously described²⁴⁷. In brief, after measurement of wet weight, tissues were immediately transferred into 1 mL of ice-cold MiR05 (0.5 mM EGTA, 3 mM $\text{MgCl}_2 \cdot 6\text{H}_2\text{O}$, 60 mM K-lactobionate, 20 mM taurine, 10 mM KH_2PO_4 , 20 mM HEPES, 110 mM sucrose and 1 g/L BSA essentially fatty acid free, pH 7.1⁴⁰) and homogenized on ice with a Potter-Elvehjem attached to an overhead stirrer (Wheaton Instruments). After ten passes (intensity level two), 600 μL of homogenate was immediately placed in an oxygraph chamber containing 1.4 mL of MiR05. Remaining homogenate was frozen at -80°C for measurement of

citrate synthase (CS) activity and total protein using a BCA protein assay (PI-23227, ThermoFisher Scientific).

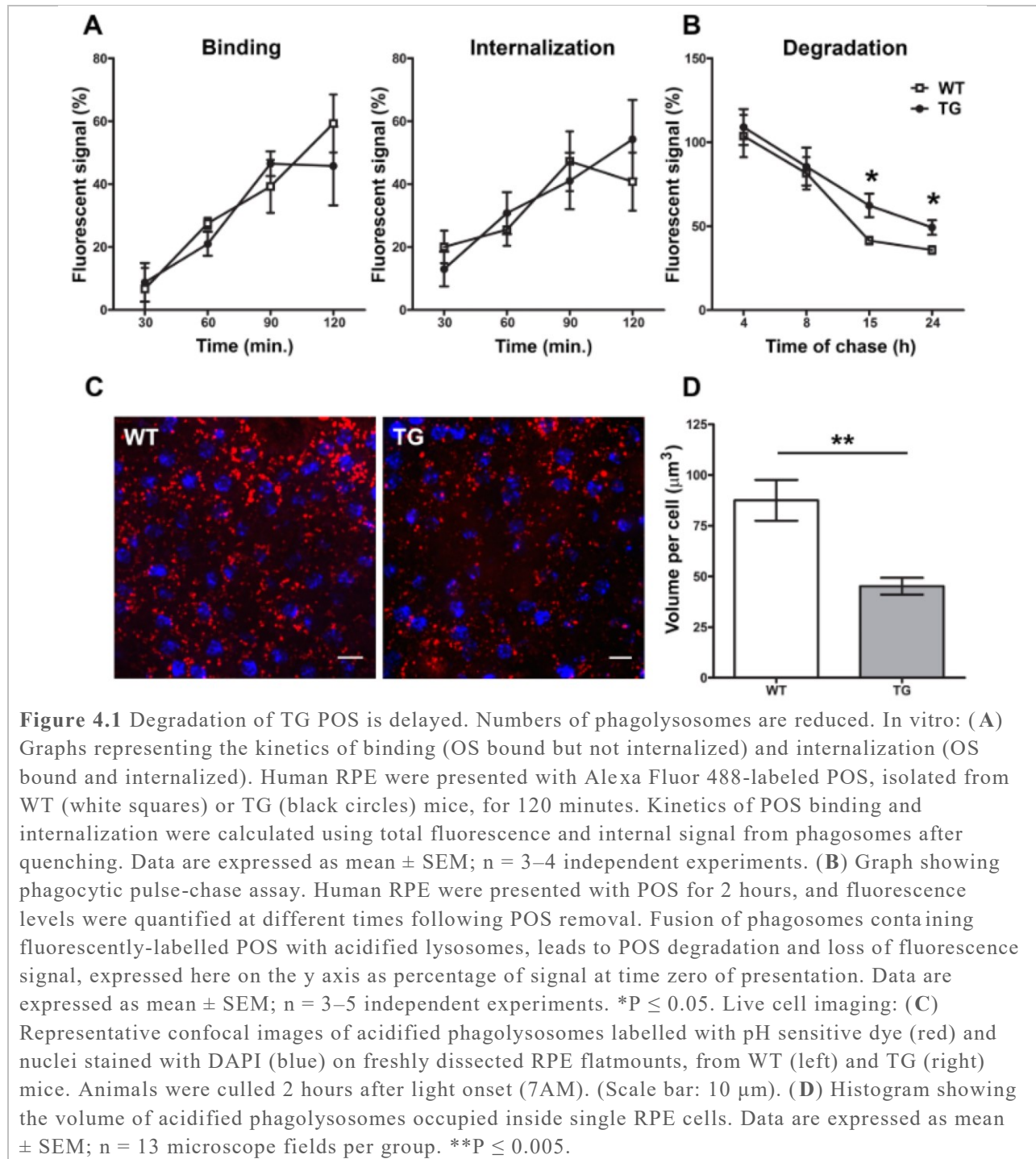
The protocol used for evaluating mitochondrial function included sequential addition of the following substrates and inhibitors: pyruvate (5 mM), malate (5 mM), ADP (2.5 mM), cytochrome *c* (cyt. *c*; 10 mM), succinate (10 mM), rotenone (1 μ M), antimycin A (5 μ M), ascorbate (2 mM), tetramethylphenylenediamine (TMPD; 0.5 mM), and azide (100 mM). Residual oxygen consumption (ROX; non-mitochondrial oxygen consumption), measured after inhibition of Complexes I and III with rotenone and antimycin A represented a small fraction (median of 5%) of maximal NS-OXPHOS capacity and was subtracted. For Complex IV respiration (CIV, cytochrome *c* oxidase), chemical background measured in the presence of sodium azide was also subtracted. Respiration was expressed in flux per mass of tissue and as Flux Control Ratios, FCR, normalized for maximal NS-OXPHOS capacity.

Datlab software (OROBOROS Instruments, Innsbruck, Austria) was used for data acquisition and analysis. Using SigmaStat4 (Aspire Software International) software, each variable was tested for normality and homogeneity of variance for ANOVA with Kolmogorov-Smirnov (Lilliefors' correction) and Spearman tests, respectively. Student's t-test and Mann-Whitney U-test were used appropriately. Data are presented as mean \pm SEM. Significance was set to $P \leq 0.05$; $n = 8$ independent experiments.

4.3 RESULTS

4.3.1 Processing of POS isolated from TG mice is delayed *in vitro*.

Since the RPE of TG mice (with photoreceptor expression of human truncated ELOVL4 protein) already demonstrates evidence of toxicity²³⁶, we hypothesize that POS presentation leads to lysosomal dysfunction in the RPE. To examine the cytotoxic effect of TG-POS on RPE cells, we presented isolated POS from WT and TG littermate mice to human RPE *in vitro*.



The kinetics of three distinct phagocytic steps was studied: POS binding, internalization into phagosomes and lysosomal degradation. Human RPE cells were challenged with fluorescently labelled POS over a 2-hour time period. A progressive increase in fluorescence signal demonstrates that RPE cells bind and internalize POS isolated from TG and WT mice with the same kinetics (**Figure 4.1A**). Therefore, RPE cells have the ability to recognize POS from TG mice, form phagosomes and internalize them.

We then quantified the ability of RPE cells to digest POS over time by performing a 2 hour pulse period with POS, followed by chase periods of increasing duration (**Figure 4.1B**). After a 4 hour chase period, the amount of fluorescence is still comparable to initial levels measured after 2 hours incubation with POS. From 4 to 8 hours, the fluorescence signal decreases at the same rate for cells incubated with either TG or WT POS (1.3-fold decrease). However, between 8 and 15 hours, fluorescence decreases at a slower rate in the group presented with TG-POS (1.4-fold vs 2.0-fold decrease). This gap persists after 24 hours of chase with the percentage of fluorescent signal remaining higher for RPE cells digesting TG-POS (49.4 ± 4.39 vs 35.7 ± 2.23 ; $P = 0.0278$). This slower decrease in fluorescence suggests that phagosome fusion with lysosomes is impeded when phagosomes contain TG-POS.

4.3.2 Acidified phagolysosome maturation is impaired.

We quantified phagolysosomes using live cell imaging of RPE in the presence of a pH-sensitive acidophilic fluorophore²⁵² at 2 hours after light onset (**Figure 4.1C**), during the predicted burst of POS uptake. In TG mice, acidified phagolysosomes occupy a 2.0-fold smaller

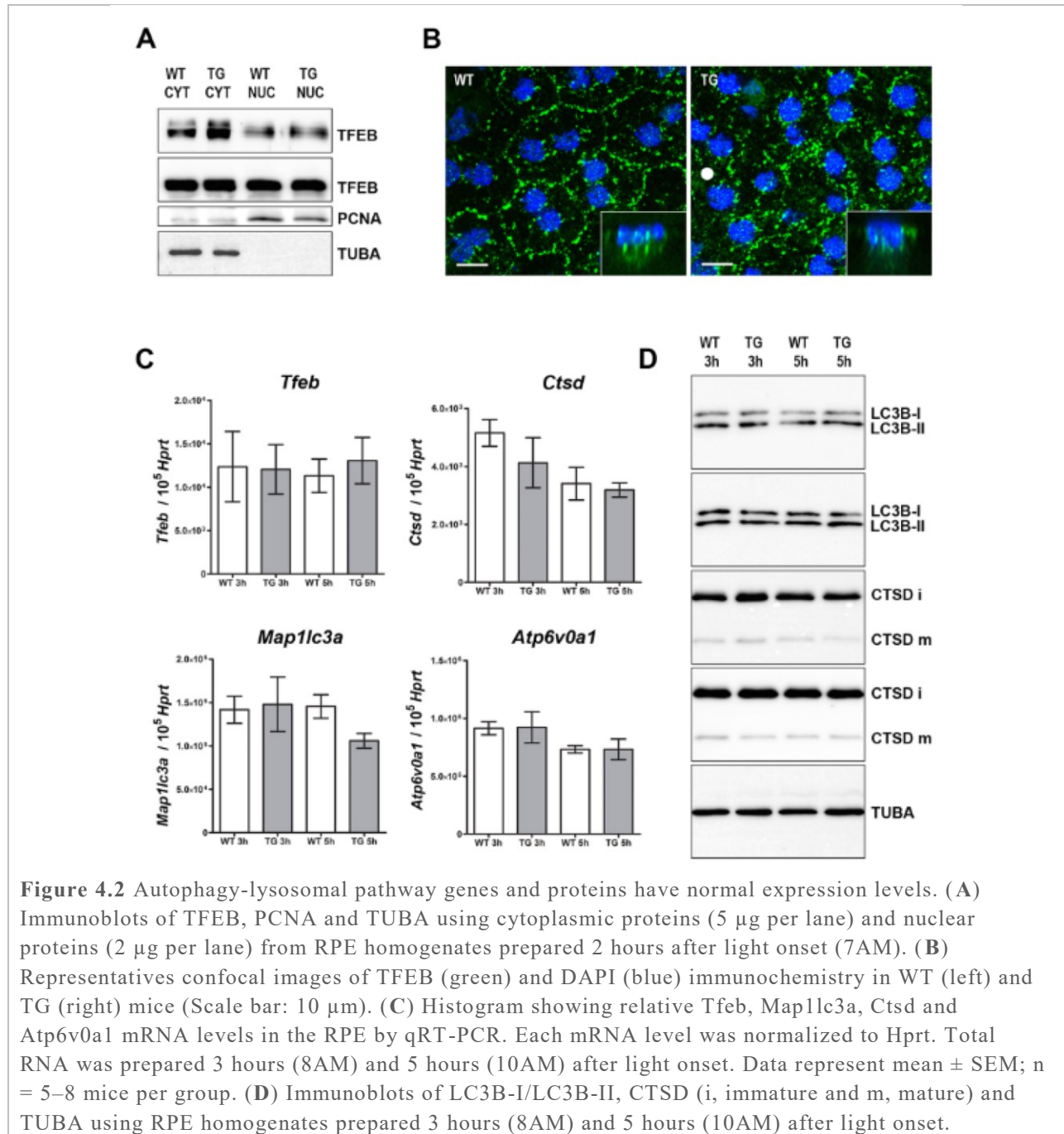
total volume within RPE cells (**Figure 4.1D**, $P = 0.001$). This difference is due to a lower number of phagolysosomes per cell (17 ± 1 in TG vs 28 ± 3 in WT; $P=0.001$; $n = 13$ images per group) and not to a difference in phagosome volume ($1.77 \pm 1.01 \mu\text{m}^3$ vs $1.84 \pm 1.03 \mu\text{m}^3$). The reduced abundance of acidified phagolysosomes in RPE cells reflects a maturation defect that could either be due to decreased fusion of phagosomes with lysosomes and/or to impaired acidification.

4.3.3 Preserved activation of autophagy-lysosomal pathway components

Phagocytosis of OS by RPE cells induces activation of Transcription Factor EB (TFEB), a master gene for lysosomal biogenesis²⁵⁴ and an effector of lysosomal function when translocated to the nucleus²⁵⁵. We quantified with western blot the respective cytoplasmic and nuclear fractions of TFEB. The ratio of cytoplasmic over nuclear TFEB (examined at 2 hours after light onset) is equivalent in TG and WT mice (**Figure 4.2A**, means of 0.50 vs 0.46, from two independent western blots). TFEB nuclear translocation is occurring at normal levels. Characterization of the cellular location of TFEB by immunofluorescence confirms the presence of TFEB in the nuclei of both TG and WT RPE (**Figure 4.2B**). In TG, TFEB-labelled vesicles are diffusely distributed within the RPE cytosol. Since TFEB acts as a sensor of lysosomal state when located on the lysosomal surface²⁵⁵, these findings warrant further studies.

Next we evaluated the transcriptional activation of *Tfeb* and of select targets of the Coordinated Lysosomal Expression and Regulation (CLEAR) gene network²⁵⁶. *Tfeb* is expressed at WT levels in the hours following POS engulfment (**Figure 4.2C**). Downstream CLEAR genes

Map1lc3a, *Ctsd* and *Atp6v0a1* are similarly unaffected. Finally, we verified unchanged protein levels of microtubule-associated protein 1 light chain 3 beta (LC3B) and cathepsin D (CTSD).



4.3.4 Members of the crystallin protein family are upregulated in RPE.

In an attempt to identify the signaling pathways affected in TG mice following POS phagocytosis, we conducted RPE proteomics. This analysis demonstrates that not all TG mice are showing changes at this early stage, as highlighted in the proteomic heatmap (**Figure 4.3A**). Across all samples, 963 proteins were analysed and compared. The close proximity of both proteomes is reflected by a Pearson correlation coefficient of 0.891, obtained when averaged protein abundances are plotted against each other (**Figure 4.3A**). Table 1 further highlights variations in protein expression between duplicates of pooled TG eyecups. Only 10 proteins are differentially expressed in a range of 4.13 to 0.11 fold-change TG pool A. Whereas TG pool B showed 64 proteins with differential expression levels and fold-change ranging from 122.32 to 0.07. One major cluster demonstrating overexpression includes the alpha-, beta- and gamma-crystallin family members (**Figure 4.3A**; Table 1).

Targeted crystallin family members (**Figure 4.3A** arrows) were examined in further detail. The greatest increase in crystallin protein expression is for CRYGA (122.32-fold). However, examination of gene expression in individual animals reveals preserved mRNA levels (Fig. 3B; $P = 0.113$). The level of *Cryaa* is similarly unchanged (small heat shock protein; $P = 0.201^{257}$). *Cryab* gene expression was only increased by 2.0-fold ($P = 0.022$). Whether this borderline upregulation might reflect a neuroprotective response to oxidative stress²⁵⁸ is unlikely in view of our respirometry results (see below). CRYBA4, CRYBB2, and CRYGS, are found in drusen

deposits²⁵⁹. Expression levels support their upregulation in TG mice; however, only the *Crybb2* increase (6.5-fold) is statistically significant (P = 0.040). Subretinal deposits are not seen in TG mice until after cell death onset²³⁶.

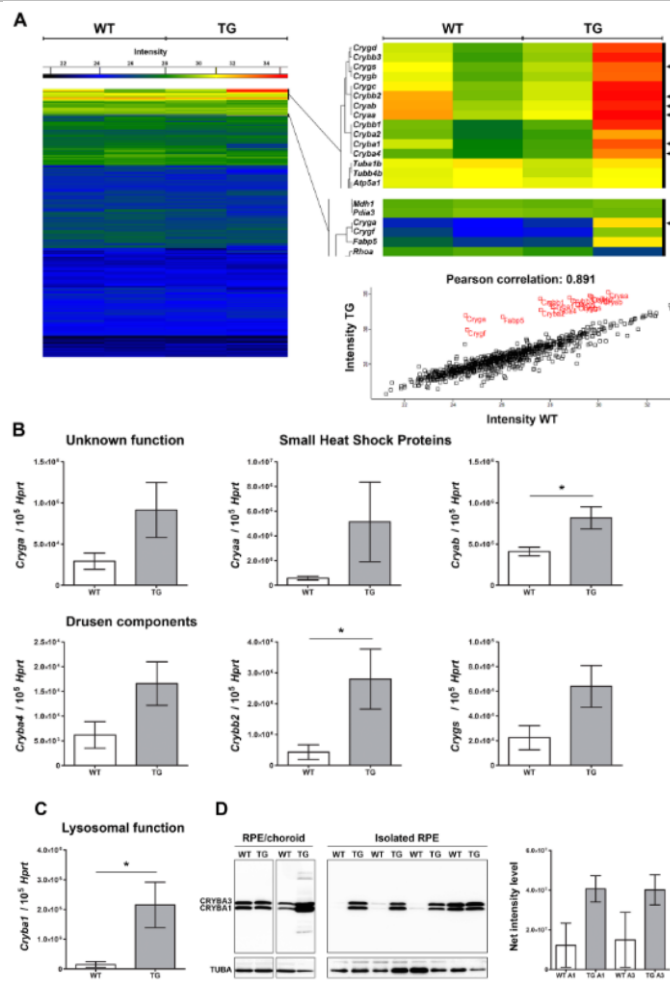


Figure 4.3 Crystallin genes and proteins are differentially expressed. **(A)** Heatmap showing expression levels of 963 proteins detected in RPE/choroid homogenates from WT (left) and TG (right) mice (2 independent experiments). Eyecup pool WT, n = 4 mice; eyecup pool TG n = 3–4 mice. Zoom showing relative intensities for the crystallin protein cluster. Expression of genes coding for targeted crystallin family members was further evaluated by qRT-PCR (black arrows). Graph showing Pearson correlation (2 independent experiments). **(B)** Histogram showing relative mRNA levels of drusen components (Cryba4, Crybb2 and Crygs), genes coding for small heat shock proteins (Cryaa and Cryab) and Cryga in the RPE by qRT-PCR. Each mRNA level was normalized to Hprt. Data represent mean \pm SEM; n = 6–10 mice per group. *P \leq 0.05. **(C)** Histogram showing relative mRNA levels of Cryba1, involved in lysosomal function, in the RPE by qRT-PCR. Each mRNA level was normalized to Hprt. Data represent mean \pm SEM; n = 7–9 mice per group. *P \leq 0.05. **(D)** Immunoblots of RPE/choroid homogenates analysed by mass spectrometry (left, proteins from 3–4 mice per lane) and isolated RPE protein extracts (right, 1 animal per lane, n = 4 each group).

We quantified mRNA and protein levels of beta-crystallin A1/A3, a regulator of lysosomal function²⁴³. *Cryba1* expression is 14.4-fold higher in TG ($P = 0.031$; **Figure 4.3C**). Western blot analysis of the RPE/choroid protein samples used for proteomics (**Figure 4.3D**) confirmed that CRYBA1/A3 levels in TG can either be equal to WT littermates or elevated. To further evaluate CRYBA1/A3 expression levels we prepared and analysed RPE-enriched proteins isolated from single animals. CRYBA1/A3 expression levels remain consistently high in TG mice. In contrast, WT mice display a wide range of expression levels, indicative of tightly regulated CRYBA1/A3.

4.3.5 RPE cells conserve their mitochondrial respiration capacity and show no sign of oxidative stress.

Since the RPE is such a metabolically active tissue, it is particularly vulnerable to oxidative stress. Mitochondria are both a source of oxidative stress and a highly vulnerable target for oxidative damage. For this reason, we examined mitochondrial oxidative phosphorylation (OXPHOS) capacity in RPE using high-resolution respirometry (Oxygraph 2k; Oroboros), as a sensitive indicator of early oxidative stress in the RPE.

Well-coupled mitochondria respond to the introduction of substrates, ADP and inhibitors. Mitochondrial function was measured as (1) LEAK respiration, a non-phosphorylated state in the absence of ADP but in the presence of substrates feeding the NADH-pathway (pyruvate and malate), and (2) OXPHOS capacity, oxygen consumption coupled to the phosphorylation of ADP to ATP. OXPHOS capacity was evaluated for both the NADH- (pyruvate and malate), and Succinate- (succinate and rotenone) pathways, as well as for the single step of Complex IV (CIV,

cytochrome *c* oxidase). The results demonstrate no differences between groups for any of the mitochondrial functions measured. The values in fluxes per mass are as follows (in pmol/s•mg for TG vs WT animals, respectively): LEAK respiration, 0.42 (0.00-3.37) vs 0.42 (0.00-2.96), P = 0.88; OXPHOS capacity for the NADH-pathway, 5.94 (4.20-8.94) vs 6.94 (4.03-13.72), P = 0.34; Succinate-pathway, 12.67 (10.58-24.01) vs 18.67 (9.43-23.10), P = 0.23; and Complex IV, 43.07 (22.22-54.49) vs 41.10 (19.68-72.54), P = 0.89. To account for subtle qualitative differences in the OXPHOS system, respiration data were also expressed as Flux Control Ratios (FCR), normalized for maximal OXPHOS capacity in the presence of electrons feeding the NADH and the Succinate-pathways simultaneously (NS-OXPHOS). The FCRs also fail to detect any significant differences between groups (*Figure 4.4A and B*).

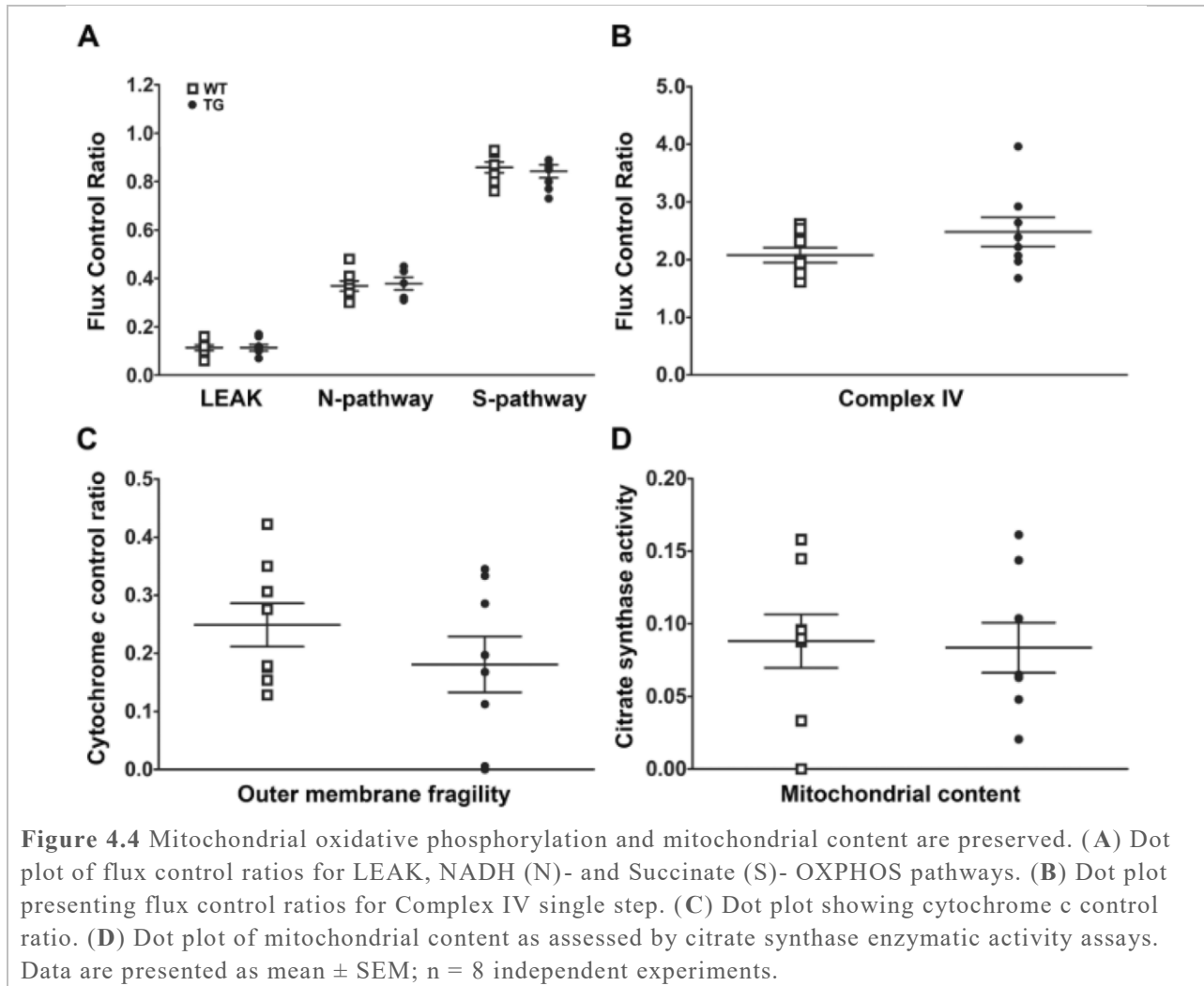
Uniprot ID	Gene name	Protein Name	Fold Change/ WT
TG eyecup pool A			
A2AEN9	<i>Gm5938</i>	Uncharacterized protein	4.13
Q02257	<i>Jup</i>	Junction plakoglobin	3.78
Q9CYZ2	<i>Tpd52l2</i>	Tumor protein D54	3.41
A2BHD2	<i>Gm14743</i>	Uncharacterized protein	3.24
Q00898	<i>Serpina1e</i>	Alpha-1-antitrypsin 1-5	3.03
Q91Z53	<i>Grhpr</i>	Glyoxylate/hydroxypyruvate reductase	0.33
P30999	<i>Ctmd1</i>	Catenin delta-1	0.31
Q9Z1Z0	<i>Uso1</i>	General vesicular transport factor p115	0.30
O35639	<i>Anxa3</i>	Annexin A3	0.29
P09470	<i>Ace</i>	Angiotensin-converting enzyme	0.11
TG eyecup pool B			
P04345	<i>Cryga</i>	Gamma-crystallin A	122.32
Q9WVJ5	<i>Crybb1</i>	Beta-crystallin B1B	52.31
Q05816	<i>Fabp5</i>	Fatty acid-binding protein	35.50
Q9JJU9	<i>Crybb3</i>	Beta-crystallin B3	24.54
Q9CXV3	<i>Crygf</i>	Gamma-crystallin F	21.58
Q9JJV0	<i>Cryba4</i>	Beta-crystallin A4	21.35
P02525	<i>Cryba1</i>	Beta-crystallin A1	20.06
Q9JJV1	<i>Cryba2</i>	Beta-crystallin A2	17.75
P04342	<i>Crygd</i>	Gamma-crystallin D	16.54
Q61597	<i>Crygc</i>	Gamma-crystallin C	15.33
P24622	<i>Cryaa</i>	Alpha-crystallin A chain	12.82
P62696	<i>Crybb2</i>	Beta-crystallin B2	12.37
P04344	<i>Crygb</i>	Gamma-crystallin B	10.04
O35486	<i>Crygs</i>	Gamma-crystallin S	8.93
P23927	<i>Cryab</i>	Alpha-crystallin B chain	7.91
Q8BKCS	<i>Ipo5</i>	Importin-5	6.12
Q78ZA7	<i>Nap1l4</i>	Nucleosome assembly protein 1-like 4	4.62
Q99K85	<i>Psat1</i>	Phosphoserine aminotransferase	4.51
Q921M7	<i>Fam49b</i>	Protein FAM49B	3.82
P16330	<i>Cnp</i>	2,3-cyclic-nucleotide 3-phosphodiesterase	3.77
P14602	<i>Hspb1</i>	Heat shock protein beta-1	3.60
P53994	<i>Rab2a</i>	Ras-related protein Rab-2A	0.33
P97457	<i>Mylpf</i>	Myosin regulatory light chain 2	0.33
P22599	<i>Serpina1b</i>	Alpha-1-antitrypsin 1-2	0.32
Q9WVA4	<i>Tagln2</i>	Transgelin-2	0.32
P35980	<i>Rpl18</i>	60S ribosomal protein L18	0.32
P62874	<i>Gnb1</i>	Guanine nucleotide-binding protein G(I)/G(S)/G(T) subunit beta-1	0.32
O35643	<i>Ap1b1</i>	AP-1 complex subunit beta-1	0.31
P14115	<i>Rpl27a</i>	60S ribosomal protein L27a	0.31
P48774	<i>Gstm5</i>	Glutathione S-transferase Mu 5	0.31
P30412	<i>Ppic</i>	Peptidyl-prolyl cis-trans isomerase C	0.30
Q9DB20	<i>Atp5o</i>	ATP synthase subunit O	0.29
F6YVP7	<i>Gm10260</i>	40S ribosomal protein S18	0.29
Q8VEH3	<i>Arl8a</i>	ADP-ribosylation factor-like protein 8A	0.28
Q99J16	<i>Rap1b</i>	Ras-related protein Rap-1b	0.28
P62717	<i>Rpl18a</i>	60S ribosomal protein L18a	0.28
Q60692	<i>Psm6</i>	Proteasome subunit beta type-6	0.28
Q9QZ88	<i>Vps29</i>	Vacuolar protein sorting-associated protein 29	0.27
Q9DCZ4	<i>Apoo</i>	Apolipoprotein O	0.27
Q9CYH2	<i>Fam213a</i>	Redox-regulatory protein FAM213A	0.27
Q9CQC9	<i>Sar1b</i>	GTP-binding protein SAR1b	0.26
O09167	<i>Rpl21</i>	60S ribosomal protein L21	0.25
Q62000	<i>Ogn</i>	Mimecan	0.24
Continued			

Uniprot ID	Gene name	Protein Name	Fold Change/ WT
Q8BL97	<i>Srsf7</i>	Serine/arginine-rich splicing factor 7	0.23
Q61171	<i>Prdx2</i>	Peroxiredoxin-2	0.22
Q99NB9	<i>Sf3b1</i>	Splicing factor 3B subunit 1	0.22
P09528	<i>Fth1</i>	Ferritin heavy chain	0.20
Q9QZ47	<i>Tnnt3</i>	Troponin T	0.19
Q9CY50	<i>Ssr1</i>	Translocon-associated protein subunit alpha	0.19
P35282	<i>Rab21</i>	Ras-related protein Rab-21	0.19
P35278	<i>Rab5c</i>	Ras-related protein Rab-5C	0.18
P97461	<i>Rps5</i>	40S ribosomal protein S5	0.18
P60766	<i>Cdc42</i>	Cell division control protein 42 homolog	0.17
P62835	<i>Rap1a</i>	Ras-related protein Rap-1A	0.16
P35293	<i>Rab18</i>	Ras-related protein Rab-18	0.16
Q9CPR4	<i>Rpl17</i>	60S ribosomal protein L17	0.16
Q9QUI0	<i>Rhoa</i>	Transforming protein RhoA	0.15
F6QL70	<i>Gm17669</i>	60S ribosomal protein L29	0.14
O08599	<i>Stxbp1</i>	Syntaxin-binding protein 1	0.14
P84104	<i>Srsf3</i>	Serine/arginine-rich splicing factor 3	0.14
P09470	<i>Ace</i>	Angiotensin-converting enzyme	0.13
O08547	<i>Sec. 22b</i>	Vesicle-trafficking protein SEC. 22b	0.13
P97315	<i>Csrp1</i>	Cysteine and glycine-rich protein 1	0.09
P63001	<i>Rac1-2-3</i>	Ras-related C3 botulinum toxin substrate 1-2-3	0.07

Table 4.1 Variation in Protein Levels in TG eyecups at one month. Threshold is set at 3-fold change.

The addition of cytochrome *c* was used as an indicator of mitochondrial outer membrane integrity and expressed as a cytochrome *c* control factor (fractional change of respiration from the state without cytochrome *c* to the state stimulated by exogenous cytochrome c^{260}). A value of zero (0.00) indicates full membrane integrity (no loss of endogenous cytochrome *c*), while a value of one (1.00) signifies maximal damage. Cytochrome *c* control factors are comparable between groups 0.18 pmol/s•mg (0.00-0.35; min-max) vs 0.23 (0.13-0.42), $P = 0.28$ (**Figure 4.4C**). The values presented are higher than previously obtained with retinas¹, likely reflecting the more aggressive mechanical disruption required for homogenizing eyecups. This addition of exogenous cytochrome *c* also served to remove the bias induced by limitation of cytochrome *c*

availability (as a result of sample preparation). Finally, mitochondrial content as assessed by citrate synthase activity is comparable between groups (*Figure 4.4D*).



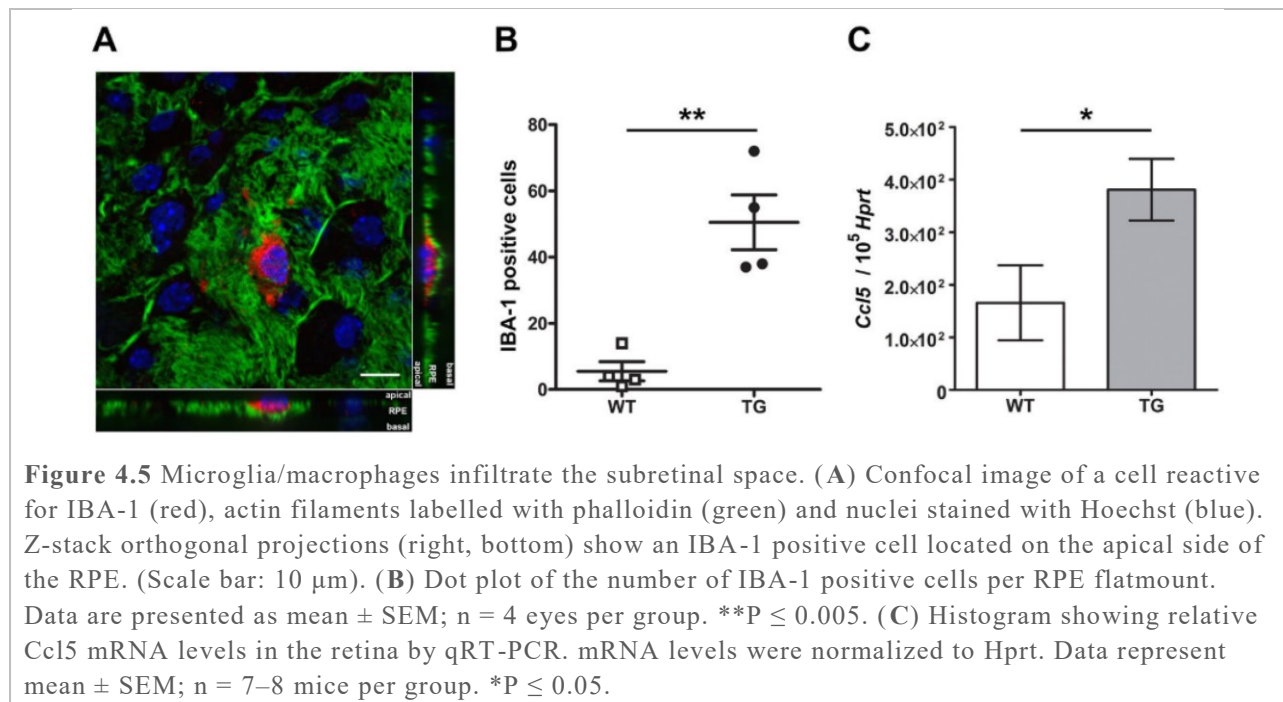
Preserved mitochondrial function excludes the possibility of oxidative stress induced by changes in mitochondrial oxidative phosphorylation capacity.

4.3.6 Microglia/macrophages infiltrate the subretinal space.

Prior to detectable subretinal debris accumulation, cells were observed on the RPE apical surface and were identified as being of the microglia/macrophage lineage (IBA-1+ labelling; Fig. 5A).

Microglia/macrophages are particularly abundant in the central part of the eye where photoreceptor degeneration first begins in this TG model^{233,247}. Confocal imaging confirms that the microglia/macrophages are at the RPE apical surface and therefore within the subretinal space (Fig. 5B). The number of IBA-1 positive cells is 8.5-fold higher in TG mice (51 ± 17 vs 6 ± 3 cells per eye; mean \pm SEM; n = 4 eyes; P = 0.014; **Figure 4.5C**).

Evaluation by qPCR (in RPE vs neural retina) for the expression of chemotactic cytokines reveals a 2.4-fold upregulation of Chemokine (C-C motif) ligand 5 (*Ccl5* or RANTES), a macrophage-activating chemokine²⁶¹, in TG retinas (P = 0.015; **Figure 4.5D**). Expression of *Ccl2*, a leukocyte-attracting signal released from the RPE/choroid with age, is low in both TG and WT mice (does not reach minimal signal intensity).



4.4 DISCUSSION

Despite detailed scrutiny, the events initiating photoreceptor death in STGD3, and many other neurodegenerative disorders, are unknown. In STGD3, photoreceptors possess the primary defect (expression of mutant ELOVL4 enzyme) and their death is responsible for vision loss. We know that loss of ELOVL4 elongase activity¹⁰⁰, essential for the synthesis of very long chain polyunsaturated fatty acids (VLC-PUFAs, of 28–36 carbon chains²³¹) does not cause retinal degeneration in STGD3^{99,234}. Therefore, STGD3 presents itself as a gain of function disease with mutant ELOVL4 playing a direct role.

We describe early pathological events in a transgenic mouse model of STGD3 maculopathy, involving two phagocytic cell types, RPE and microglia/macrophages, prior to the death of photoreceptors. At the circadian peak of outer segment uptake, acidified RPE phagolysosomes are 50% less abundant in TG animals with photoreceptors expressing the mutant protein. This finding reveals that impairments are occurring in a step prior to degradation. The delays in degradation of fluorescent signal observed *in vitro*, when fluorescently labelled OS (isolated from TG compared with WT animals) are presented to human RPE cells may result from dysfunction in upstream events. *In vivo* evidence for processing delays at one month of age include: 1) increased expression of crystallin protein family member CRYBA1/A3, a regulator of lysosomal function²⁴³; 2) upregulation of drusen component CRYBB2²⁵⁹; and 3) invasion of microglia/macrophage in the central retina, where photoreceptor loss begins^{233,259}, despite still undetectable accumulation of debris²³⁶; **Figure 4.6** summarizes these events.

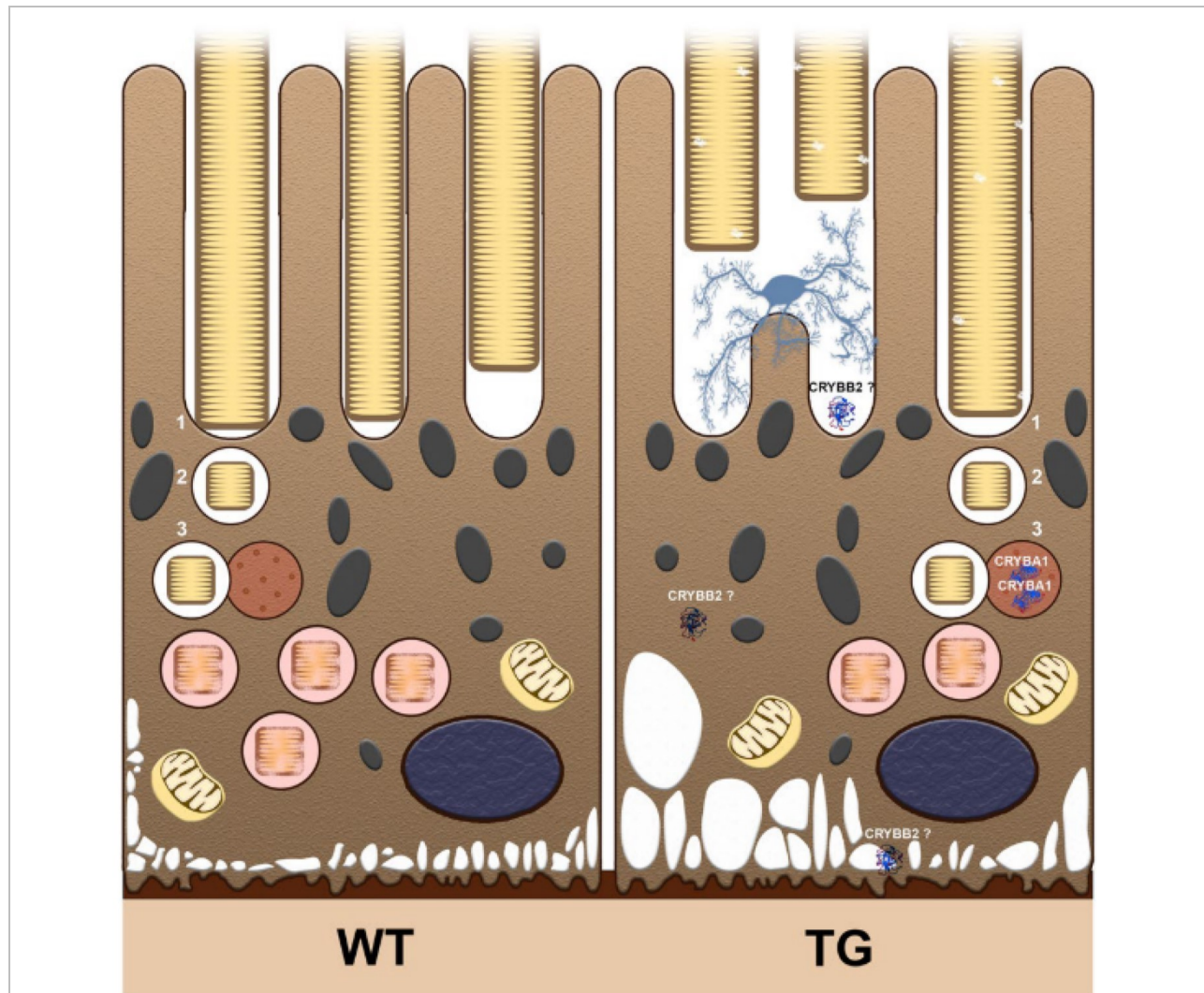


Figure 4.6 Summary of events occurring prior to photoreceptor death. Daily renewal of POS relies on phagocytosis of shed POS (in yellow) by underlying RPE cells (cytoplasm, brown; melanosomes, grey; nuclei, dark blue). In healthy cells (on the left), POS are recognized by microvilli (1) and phagosomes containing shed POS are internalized (2). Finally (3), phagosomes fuse with lysosomes (red vesicle), forming mature acidified phagolysosomes (red vesicles containing POS). In TG mice (on the right), photoreceptors expressing the mutant human ELOVL4 protein have outer segment ultrastructural abnormalities. Presentation of these segments to RPE cells leads to impaired phagolysosome maturation. Less acidified phagolysosomes are detected during the burst of phagocytic activity (2 hours after light onset). Lysosomal protein CRYBA1/A3 levels remain abundant (3 and 5 hours after light onset). Vacuoles (in white) form at the basal RPE. RPE cells produce CRYBB2, a protein present in AMD drusen. Phagocytic cells (microglia/macrophages, pale blue) are recruited to the subretinal space.

Mouse models of RPE phagolysosomal maturation defects, such as induced in the absence of caveolin-1, share a phenotype of reduced lysosomal acidification and delayed POS protein clearance²⁶². In *Abca4*^{-/-} mice, lysosomal pH is abnormally elevated as early as four months, in parallel with age-dependent accumulation of A2E, the main constituent of lipofuscin²⁶³. Since we previously demonstrated normal A2E levels at one month of age in ELOVL4 transgenic mice (with increases of 10% at 3 months²⁴⁶), this toxin is unlikely to affect lysosomal pH at this early stage²⁶⁴.

The long term impact on RPE homeostasis of daily occurring phagolysosomal maturation delays may provide an explanation for RPE vacuolization in TG mice observed already at one month²³⁶. Vacuolization has been reported in mouse models exhibiting dry-AMD pathological hallmarks including mutant *Elovl4* knock-in²⁶⁵. Vacuoles are also evident in models of lysosomal clearance defects, such as *Cryba1* cKO mice²⁶⁶.

Crystallins (alpha-, beta- and gamma-) have been associated with innate stress responses in neurodegenerative disorders²⁶⁷. Persistently elevated CRYBA1/A3 supports that compensatory homeostatic mechanisms are activated in RPE cells experiencing processing delays in the presence of photoreceptors expressing mutant ELOVL4 protein. CRYBB2, along with CRYBA4 and CRYGS accumulate in AMD drusen²⁵⁹. Upregulation of *Crybb2* and other crystallin genes was also reported following induction of RPE damage in D-galactose fed mice²⁵⁷. Whether CRYBB2 also accumulates in subretinal and/or basal laminar debris remains to be elucidated.

The IBA-1+ cells present in the subretinal space can be either microglia or macrophages or both²⁶¹. Defects in RPE phagocytosis, and not cell death, have been attributed to the recruitment of microglia/macrophage cells in the subretinal space. As the primary resident immune cells in the retina, migrating microglial/macrophages initially participate in debris clearance²⁶⁸ and adaptive para-inflammation²⁶⁹. With the persistent build-up of undigested material, microglia/macrophages have been shown to impair the structure and physiology of RPE cells²⁷⁰ and to induce the expression by RPE cells of pro-inflammatory cytokines that aggravate microglia/macrophage accumulation, leading to deleterious inflammation and cell death²⁷¹.

Disturbances in mitochondrial physiology are involved in a variety of neurodegenerative diseases²⁷². Ultrastructural analysis of human AMD donor eyes revealed a reduction in the number of RPE mitochondria, associated with loss of cristae and membrane density²⁷³. We previously reported abnormal morphology in RPE mitochondria (swollen intercrystal spaces) but only after the onset of photoreceptor death²³⁶. A recent study showed that photoreceptor outer segment phagocytic function provides the metabolic substrates needed for mitochondrial fatty acid β -oxidation and ketogenesis in the RPE²⁷⁴. In *Mreg*^{-/-} and *Abca4*^{-/-} mouse models, defective phagosome maturation and degradation lead to delayed ketogenesis²⁷⁵.

Our findings reveal that phagolysosomal maturation defects provide the earliest known link between photoreceptor expression of human mutant ELOVL4 and the onset of photoreceptor cell death, and as such present a potential novel preventative target for STGD3 and other pathologies such as AMD that might share similar triggering events.

5 CIV EFFECT OF PHOTOBIMODULATION

5.1 INTRO

Photobiomodulation (PBM) is a relatively new therapeutic technique that reportedly exerts its effects through modulation of mitochondrial function. It involves a single or series of infrared light (600 – 1,000 nm) exposures at low intensity, without photothermal effect. Most of biochemical mechanism of PBM has yet been illuminated, but the currently accepted model describes cytochrome *c* oxidase, Complex IV (CIV) of mitochondria, as the principal photoacceptor of infrared light. More specifically, the copper and heme redox centers of CIV demonstrate absorbency in NIR range of light¹³⁸. The fact that the light corresponding to CIV's absorption spectra could induce biological responses such as increased DNA synthesis and toxin resistance is used to suggest that mitochondria is involved in mechanism of PBM^{128,138}.

Reportedly, the interaction between NIR light and CIV results in dissociation of nitric oxide (NO) from oxygen-binding site of CIV²⁷⁶ and subsequently increases electron flow through the electron transport system (ETS) and the mitochondrial ATP production²⁷⁷. The increased ATP production in response to PBM have been reported^{278,279}. Also, there are some respirometer studies utilizing a traditional Clark-type electrode. One of them reports 808nm laser-induced increase in NADH- and Succinate-pathways (N- and Succinate-pathways) respiration and CIV function (CIV single step)²⁸⁰. Another study utilizing the same setup reports multiple-fold increase in ROUTINE respiration (respiration with endogenous substrates available in cell medium) from 650-900nm LED and laser exposures²⁸¹. Following these primary effects of PBM,

there are reported secondary effects such as activation of kappa-light-chain-enhancer of activated B cells (Nf- κ B) pathway^{140,144} and Janus kinase signal transducer and activator of transcription (JAK-STAT) pathway^{143,145} that are attributed to the clinical improvements reported in response to PBM therapies¹²². While there are accumulating evidences of various clinical benefits and biochemical pathways that may explain such effects of PBM, the studies looking into the first events of PBM – the mitochondrial effect – have not been extensively investigated. In recent study, the CIV expression and activity (measured through enzymatic activity assay) were not changed with 670nm LED exposure even though it did improve retinal vascular improvement in diabetes¹⁵⁷. Another study utilizing a traditional Clark-type electrode found that irradiation with NIR light laser had no effect in reversing the NO-mediated inhibition of CIV²⁸². A fluorescent-probe based respirometer study also report lack of increased respiration following NIR light irradiation²⁸³.

Essentially, while PBM's effect to increase CIV function has been implicitly accepted in most of contemporary studies, the recent reports that shows no or negative changes has not been adequately addressed. In present study, we aim to provide a preliminary, but nonetheless detailed account of the changes in mitochondria in response to NIR light exposure. Changes in various aspects of mitochondrial function over 24h-time course following a single exposure to NIR light with well-defined parameters are reported here. Based on the report that ATP concentration peak after 6h²⁸³, we hypothesized that a single application would elicit maximal response at 6h and return to baseline by 24 h post-exposure and the functional change would occur immediately after NIR light exposure.

5.2 METHODS

5.2.1 Cell Culture

Two cell lines were used for investigation of changes in mitochondrial function in response to NIR light exposure. Largely, the effects were studied in two bodies of study: real-time effect measured simultaneously with the light exposure and post-exposure effect measured hours after the initial exposure was done. Jurkat human immortalized T lymphocytes cells were used for the post-exposure study with varying light fluence and post-exposure times. Cells were grown from 75cm² falcon tissue culture treated flasks (353136, Falcon) placed in humidified incubator containing 5% CO₂ at 37 °C. Jurkat cells were maintained with RPMI 1640 medium containing L-glutamine (SH3002701, HyClone) enriched with 10% fetal bovine serum (Canadian origin, F1051, Sigma-Aldrich), 100 U/mL penicillin, and 100 µg/mL streptomycin. Cells were split 1:2 every 3 days. When cells have reached 80% confluency, at concentration of approximately 0.5-1x10⁶ cells/mL, 20mL each of cells are placed in two 75cm² flasks. One of the flask received NIR treatment of appropriate fluence while the other received control treatment (ambient light).

For real-time segment of the study, mutant version of the SV40 large T antigen derived from Human embryonic kidney cells 293 (HEK293T) were grown in the same manner as described above, except that the cells were maintained with DMEM cell medium (11965118, ThermoFisher). Cells were collected with 0.05% trypsin-EDTA with final concentration of approximately 1.0-2.0x10⁶ cells/mL.

The change in cell models occurred as we realized HEK293T may not be a suitable model for post-exposure protocol that requires repeated measurement throughout the day – for repeated trypsinization necessary to study HEK293T in O2k would have introduced mechanical stress to the cells; thus, a suspended Jurkat cells were used instead. This was an acceptable compromise as this study represents a preliminary study exploring broad effect of PBM.

5.2.2 NIR light Exposure

The real-time experiments were carried out with 2.0mL of HEK293T cells placed in the experimental chambers of the respirometer (Oxygraph 2k, OROBOROS Instruments, Innsbruck, Austria). NIR light exposures were applied by holding the LED devices immediately next to the observational window of the O2k during specific titration step of O2k protocol and lasted until the end of monitoring (discussed below). Two light devices with power densities of 6.37mW/cm² and 200mW/cm² (described in *Table 5.1*) were used on separate chambers to examine light intensity-dependent differences in the mitochondrial response. There were one control chambers (no light treatment) for each light treated chambers which were used in paired t-test statistical analysis.

Table 5.1 Light Characteristics of NIR Light

Parameters	6.37mW/cm² light	200mW/cm² light
Manufacturer	Assembled in U of A workshop with ELD-670-524 from Roithner	Red Light Man
Year produced	2017	2017
Number of Emitters	10 LEDs	12 LEDs
Wavelength	670±10 nm	670±10 nm

Radiant power	6.37 mW/cm ²	200 mW/cm ²
---------------	-------------------------	------------------------

For post-exposure experiments with Jurkat cells, NIR light exposures were carried out with LED device with power density of 0.637mW/cm² at distance of 1cm from the bottom of the flask. Both treated and control flasks were in room temperature during the exposure process. Fluence of 0.5J/cm², 5J/cm², and 36J/cm² are applied by varying the exposing time of same LED light at 78 seconds, 785 seconds, and 5652 seconds, respectively (*Equation 5.1*).

Equation 5.1 $Fluence (J/cm^2) = Radiant\ Power (mW/cm^2) * Time (s)$

The light exposure did not alter the temperature of the flasks. Once the light exposures have been completed, the flasks were kept in 5% CO₂ at 37 °C incubator until the O2k examination.

5.2.3 Mitochondrial Functional Assessment with O2k

O2k high-resolution respirometry was used to study the mitochondrial functional changes associated with NIR light exposure. The post-exposure measurements were performed on Jurkat cells at time point of 1h, 3h, 6h, and 24h after NIR light exposure (n=6-10 for each group). Cells were counted immediately before the O2k experiment started. At each time point, 200 uL of cells from each group were frozen at -80 °C for measurement of citrate synthase (CS) activity.

The protocol used for evaluating mitochondrial function included sequential addition of the following substrates and inhibitors: malate (5 mM), glutamate (5 mM), oligomycin (10mM), carbonyl cyanide-p-trifluoromethoxyphenylhydrazone (FCCP; 0.1mM), rotenone (1 μM),

antimycin A (5 μ M), ascorbate (2 mM), tetramethylphenylenediamine (TMPD; 0.5 mM), and azide (100 mM). Residual oxygen consumption (ROX; non-mitochondrial oxygen consumption), measured after inhibition of CI and CIII with rotenone and antimycin A represented a small fraction (median of 5%) of fully uncoupled respiration and was subtracted from all data prior to data analysis. The last three substrate/inhibitor titration (As, TMPD, and Azd) are used for the CIV function examination was used. The respiration following Azd titration (chemical background) is corrected from the As+TMPD respiration.

The ETS respiration was achieved by small titration steps of uncoupler, FCCP. This was used to express the respiration data in Flux Control Ratios (FCR). In FCR, respiration states are normalized against the ETS capacity and are allow comparison of respiration data independently from how many cells and/or mitochondria are present in the O2k chamber (respiration expressed in flow per cell). For real-time experiment with HEK293T cells, infrared treatment started after titration of rotenone and antimycin A and continued until the end of the titration protocol.

DatLab software (OROBOROS Instruments, Innsbruck, Austria) was used for data acquisition and analysis. Using SigmaStat4 (Aspire Software International) software, each variable was tested for normality and homogeneity of variance for ANOVA with Kolmogorov-Smirnov (Lilliefors' correction) and Spearman tests, respectively. Paired t-test and Wilcoxon signed rank test were used appropriately. Data are presented as mean \pm SEM. Significance was set to $P \leq 0.05$.

5.3 RESULTS

5.3.1 Intermittent changes in ROUTINE Respiration

ROUTINE respiration refers to the oxygen consumption measured by O2k that reflects the mitochondrial activity with endogenous substrates present in the culture media. All the data presented in result section is FCR corrected for ROX, unless otherwise stated. With NIR exposure with fluence of 5J, there was increase in ROUTINE respiration at 6h post-exposure (0.461 ± 0.0251 vs. 0.492 ± 0.0230 ; $p=0.000526$) while the 15J treated cells at 24h post-exposure time showed decreased respiration (0.529 ± 0.0224 vs. 0.504 ± 0.0220 ; $p=0.014$). In other groups, the ROUTINE respiration remained unchanged.

5.3.2 NIR Light exposure did not increase CIV activity

The effect on CIV activity, both the magnitude of the change and the temporal characteristic of the change did not increase with real-time measurements with the radiant power of 6.37mW/cm^2 and 200mW/cm^2 (**Figure 5.1A**). Relative decrease in CIV capacity in cells treated with 0.5J fluence of NIR light at 1h (control 2.879 ± 0.118 vs. treated 2.336 ± 0.249 in FCR; $p=0.0194$), 3h (control 2.342 ± 0.120 vs. treated 1.960 ± 0.163 in FCR; $p=0.031$), 6h (control 2.181 ± 0.0520 vs. treated 1.785 ± 0.171 in FCR; $p=0.0462$) and 24h (control 2.125 ± 0.162 vs. treated 1.900 ± 0.182 in FCR; $p=0.031$; **Figure 5.1CD**). The decrease in CIV relative capacity was also measured at 5J fluence and 24h post-exposure (control 2.546 ± 0.373 vs. treated 2.319 ± 0.388 in FCR; $p=0.031$; **Figure 5.1D**).

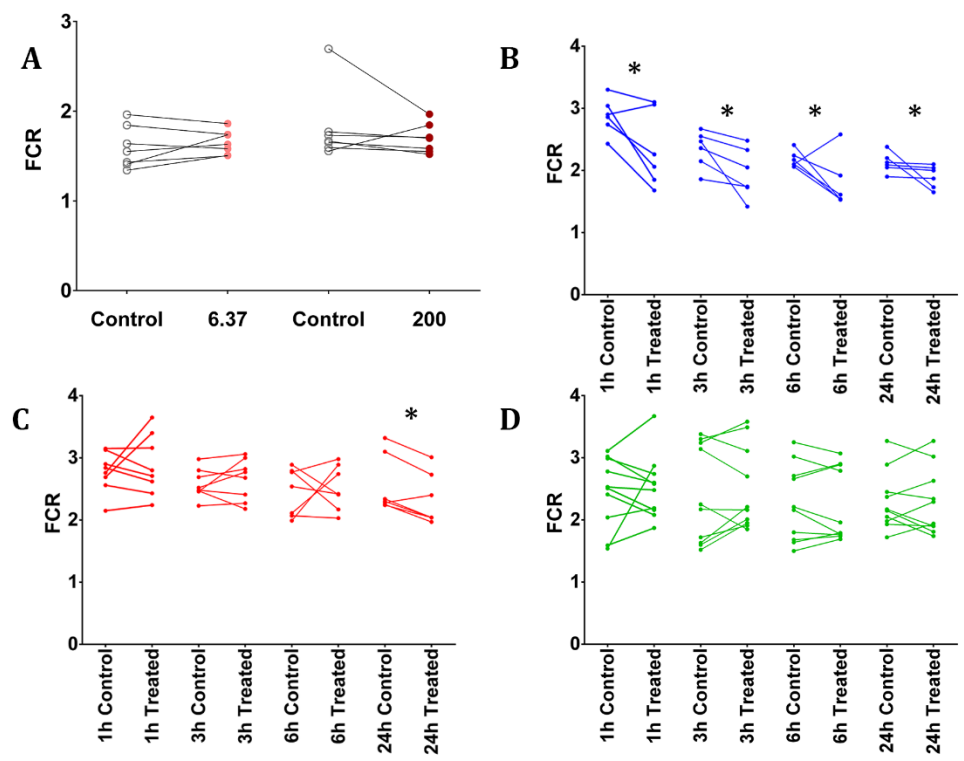
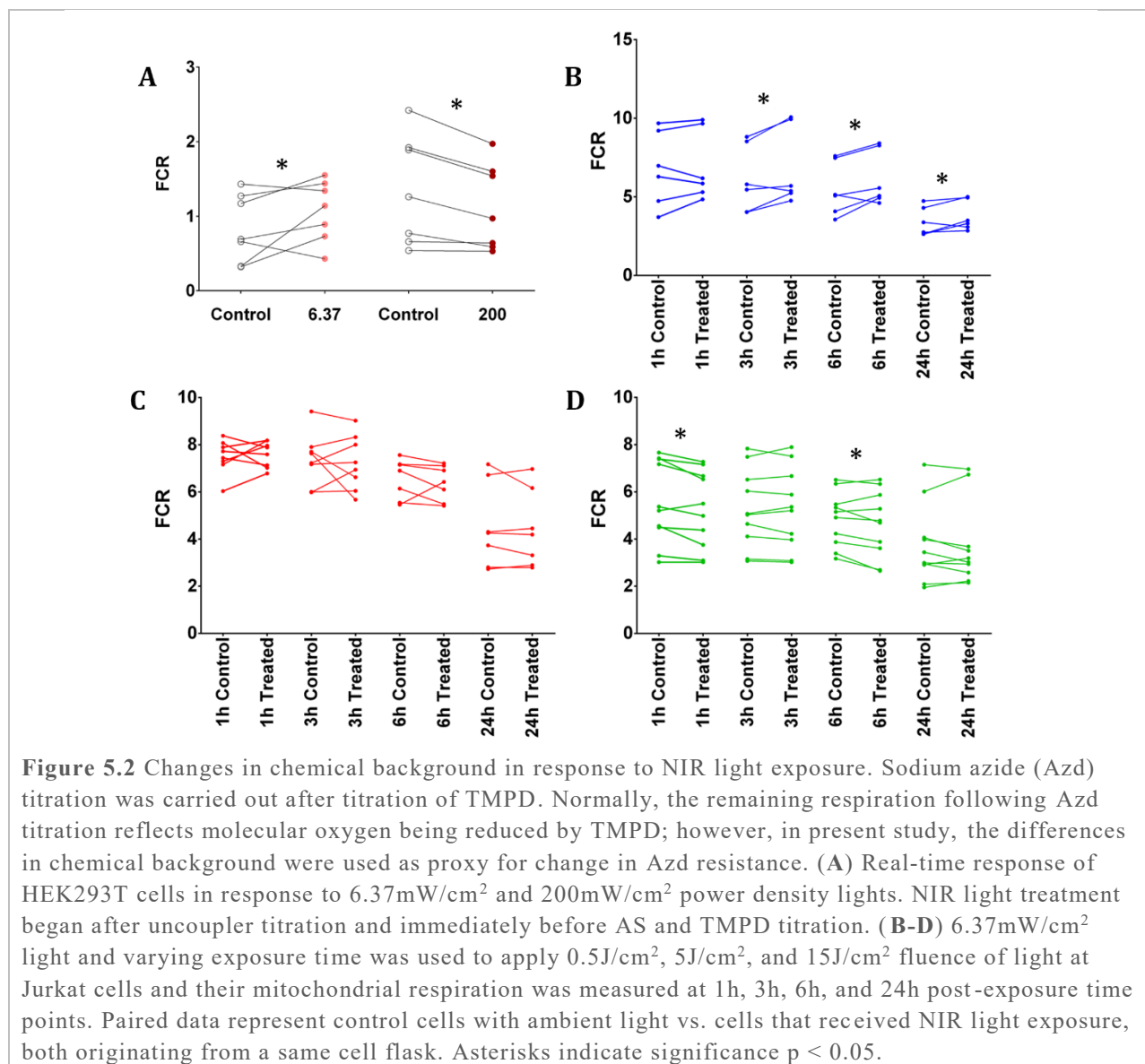


Figure 5.1 Changes in CIV single step respiration in response to NIR light exposure. Change in mitochondrial function was assessed using O2k respirometer. (A) Real-time response of HEK293T cells in response to 6.37mW/cm² and 200mW/cm² power density lights. NIR light treatment began after uncoupler titration and immediately before AS and TMPD titration. (B-D) 6.37mW/cm² light and varying exposure time was used to apply 0.5J/cm², 5J/cm², and 15J/cm² fluence of light at Jurkat cells and their mitochondrial respiration was measured at 1h, 3h, 6h, and 24h post-exposure time points. Paired data represent control cells with ambient light vs. cells that received NIR light exposure, both originating from a same cell flask. Asterisks indicate significance $p < 0.05$.

5.3.3 PBM increased chemical background

Chemical background oxygen consumption is oxygen consumed by non-mitochondrial sources such as oxygen consumed in chemical reaction with TMPD, as well as non-mitochondrial biological consumers of oxygen such as NADPH oxidase (NOX)²⁸⁴. TMPD will readily reduce molecular oxygen and therefore, without appropriate correction, the respiration reported by titration of TMPD will be a lot higher than the oxygen used by CIV alone.

The NIR light exposure increased chemical background respiration immediately (*Figure 5.2A*) following the 6.37mW/cm² (0.838±0.170 vs. 1.075±0.155; $p=0.0492$). In contrast, the 200mW/cm² exposure decreased the chemical background (0.1351±0.278 vs. 1.120±0; $p=0.00372$). Similarly in post-exposure experiments, the lower fluence increases the chemical background and higher fluence decreased it. 0.5J fluence treated cells' chemical backgrounds were increased at 3h (6.111±0.863 vs. 6.849±1.005; $p=0.0266$), 6h (5.491±0.693 vs. 6.142±0.707; $p=0.0288$), and 24h (3.409±0.373 vs. 3.781±0.388; $p=0.0482$; *Figure 5.2B*). On the other hand, the chemical backgrounds in 15J fluence treated cells were decreased in 1h (5.555±1.756 vs. 5.234±1.639; $p=0.00957$) and 6h post-exposure time points (4.836±1.155 vs. 4.629±1.404; $p=0.0500$; *Figure 5.2C*).



In the CIV function without the chemical background correction, most of the differences reported with the corrections were no longer significant. CIV function without correction was greater in 6.57mW/cm² power density light exposed real-time cells (2.435 ± 0.189 vs. 2.727 ± 0.166) and lower in 200mW/cm² power density light exposed cell (3.161 ± 0.244 vs.

2.817±0.222). In post-exposure settings, 0.5J fluence treated cells at 1h post exposure had lower CIV function without chemical background correction (9.648±0.979 vs. 9.290±0.936) as well as 5J fluence treated cells at 24h time (7.077±0.828 vs. 6.713±0.747).

5.4 DISCUSSION

In present study, we provide detailed account of (1) CIV response immediately after 670nm 6.37mW/cm² or 200mW/cm² power density lights, and (2) mitochondrial functional response to a single exposure of 670nm light with 6.37mW/cm² power density at 0.5J, 5J, 15J fluence at 1h, 3h, 6h, and 24h post-exposure using O2k respirometry.

With many of the PBM studies focusing on its clinical benefits and mechanisms directly related to them, there are surprisingly little studies that investigate the mitochondrial functional changes in response to NIR light exposure. This is especially worrying considering the recent studies demonstrate a lack of CIV functional increase^{150,282,283}, which contradicts the conventional notion that the increased CIV function in response to NIR light exposure^{134,136,280,281} instigates other downstream effects.

Almost all of the studies looking into direct functional changes in CIV in PBM are done polarographically, using traditional Clark-type electrodes^{135,136,280-282}. While O2k also utilizes Clark-type electrode, it is equipped with sophisticated measures for precise temperature control in the experimental chamber, calibration for oxygen consumption by electrodes, oxygen back-

diffusion from the chamber wall material, and sufficiently large experimental chamber that support long titration protocol for experimental flexibility²⁸⁵, which are lacking in previously mentioned studies using the traditional Clark-electrodes. Furthermore, the term “mitochondrial function” is used ambiguously across different studies – one study report increased *state 4* respiration (roughly equivalent to the LEAK respiration in the present study) with succinate as a substrate²⁸² while another use increased ROUTINE respiration²⁸¹ as evidence of increased mitochondrial function in PBM. Indeed, both of these parameters are components of mitochondrial function, but are not an assessment of CIV function and should be discussed in more specific terms. The O2k data demonstrated in the present study represent more comprehensive and more reliable report of mitochondrial changes in response to PBM.

In contrast with the conventional PBM mechanism, we observed decreased CIV function in cells exposed to 670nm light with a fluence of 0.5J/cm². One possible explanation of this decrease is PBM-induced increase in NO availability and subsequent inhibition of CIV. Our speculation may be unintuitive since the conventional mechanism attributed the increase in CIV function in PBM to photo-dissociation of NO from CIV^{121,277}; however, series of recent studies reported that the PBM induces an increase in NO availability through activation of inducible nitric oxide synthase (iNOS)^{286,287} and photolysis from nitrosyl complexes^{288–290}. Both HEK293 and Jurkat cells demonstrate a capacity for iNOS activity^{291–293} and possess heme groups and iron-sulfur groups²⁹² that can be targets of nitrosylation. Therefore, it is possible to imagine that the observed decrease in CIV function may reflect increased NO availability due to increased dissociation of NO from nitrosyl complexes in the cell. Upregulation of iNOS gene in PBM has

been reported also¹⁵⁵, further supporting our proposed explanation. In this context, the reason why decrease in CIV function was observed 1h after the exposure and not immediately as light was being applied may be that the initial increase in NO by photo-dissociation of nitrosyl complexes were not enough to cause inhibition of CIV function; however, when iNOS activity increases by gene regulation, the NO concentration increased enough to trigger measurable functional inhibition.

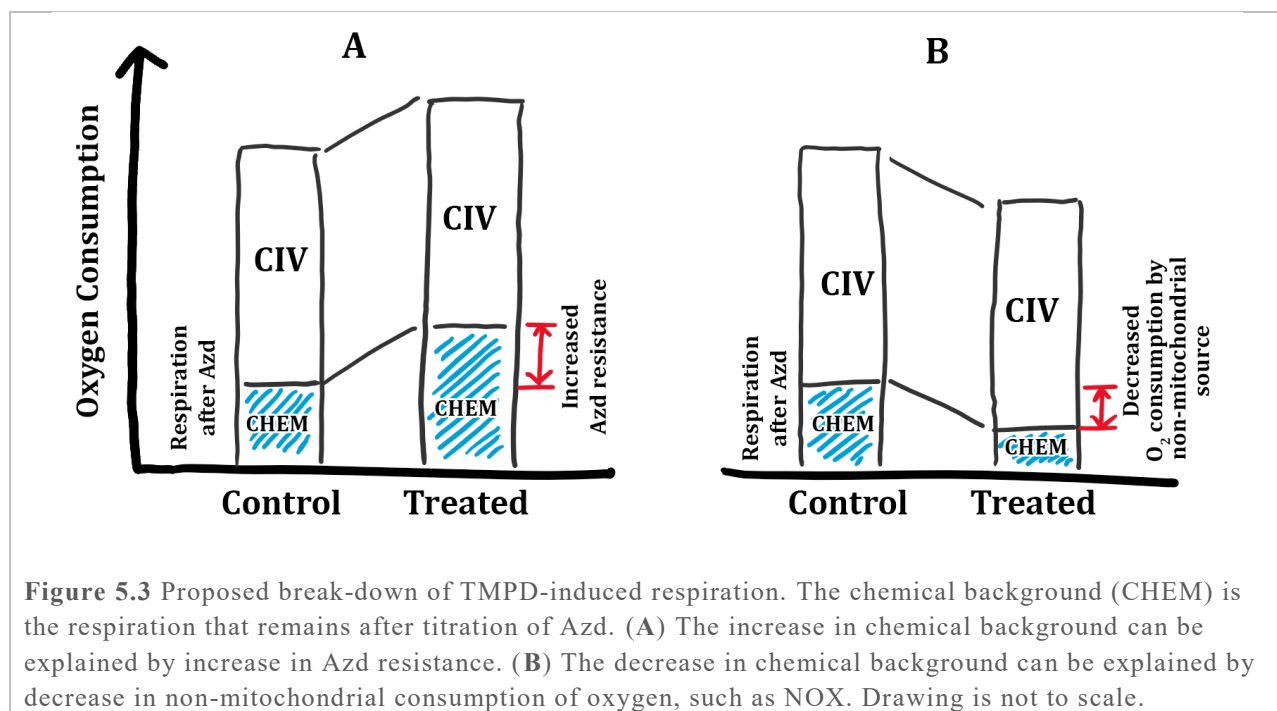
It is crucial to note that a conclusive interpretation of CIV function is difficult since PBM seems to modify both CIV function as well as CIV's resistance to toxins^{128,129}. The change in toxin resistance introduces unaccountable variable to CIV function due to the titration protocol O2k uses to study CIV function. In this study, a combination of TMPD and Azd is used to calculate CIV function. TMPD is a potent oxidizing agent and will reduce molecular water as well as its intended target (cytochrome *c*)²⁹⁴. Therefore, CIV inhibitor, Azd, is titrated after TMPD to monitor the oxygen consumption from non-mitochondrial sources – this is called the chemical background since the majority of it arises from chemical consumption of molecular oxygen by TMPD. Though there are some non-mitochondrial biological sources of oxygen consumption such as NADPH Oxidase (NOX)^{27,284,295}. The chemical background is subtracted from total TMPD-induced respiration to calculate CIV function. Out of the two studies that utilized TMPD titration performed the chemical background correction^{136,280}, while both studies report increased TMPD-induced respiration following NIR light exposure, none of them performed chemical background correction. However, when our CIV functional data are expressed without chemical background correction, most of the differences seen in corrected

data disappeared. Real-time data, which were not different in chemical background-corrected data, were statistically different when expressed in uncorrected-form. The cells exposed with 6.37mW/cm² light had higher respiration, and the cells treated with 200mW/cm² light had lower respiration compared to their respective control. The chemical background themselves were decreased in cells with 6.37mW/cm² light and increased in cells with 200mW/cm².

The increase in uncorrected CIV function and chemical background with no change in corrected CIV function in real-time 6.37mW/cm² light treated cells may be explained by increased Azd resistance. The PBM's effect of increasing the resistance against CIV-specific inhibitors such as cyanide have been reported^{128,129}. If the light-treated CIV becomes more resistant to Azd, there would be more uninhibited respiration following Azd titration which would over-report the chemical background (*Figure 5.3A*). That is, higher the chemical background, higher the increase in Azd resistance. A similar explanation could be applied to other sites where an increase in chemical backgrounds was observed such as 0.5J fluence treated cells at 3h, 6h, and 24h time points.

On the other hand, decrease in chemical background observed in cells exposed to 200mW/cm² light and 15J fluence treated cells at 6h post-exposure cannot be explained through a change in Azd resistance. Indeed, the PBM reportedly produce biphasic responses, where therapeutic effect observed at an optimal dose of light disappears and even cause negative effects when the dose is too great¹²¹. However, as the titration of sodium Azd at saturating concentration already inhibit all oxygen consumption by CIV²⁹⁴. Therefore, a decreased chemical background (i.e. increased amount of oxygen consumption being inhibited by Azd titration) cannot be

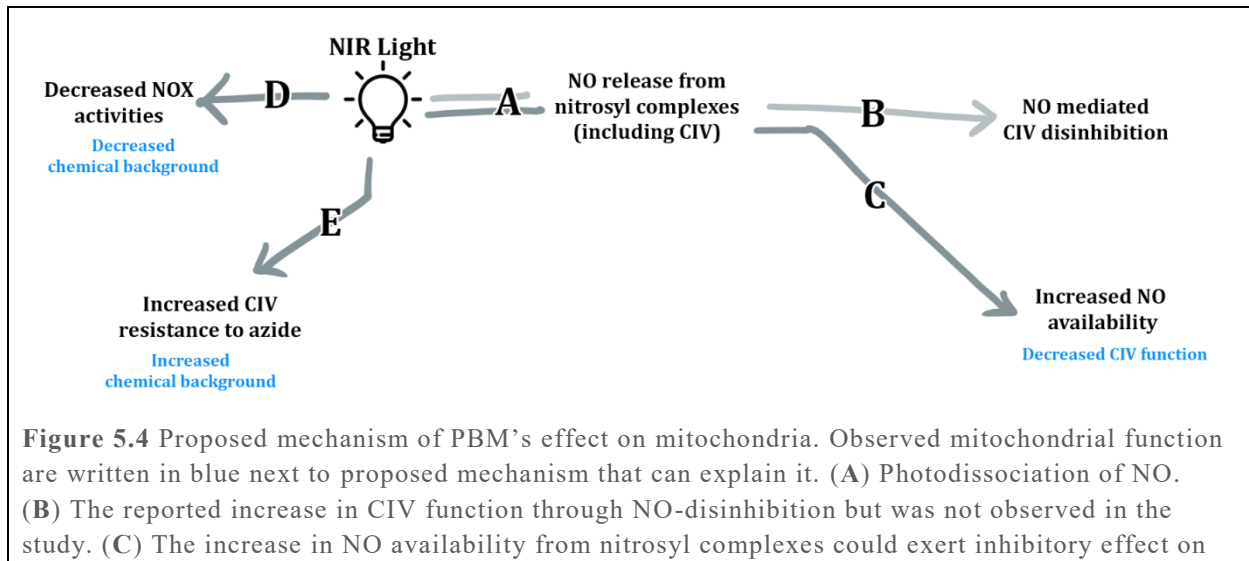
explained by “over-inhibition” of CIV function (**Figure 5.3B**). Perhaps NIR light also modulates oxygen consumption by non-mitochondrial sources of oxygen consumption such as NOX2 and NOX4²⁹⁵ which are present in HEK293 and Jurkat cells^{284,296}. Given the antioxidative effects of PBM¹²¹, the superoxide-producing NOX may play a significant role in the PBM mechanism. In fact, NO-mediated inhibition of NOX have been reported, though how or whether this fits into PBM is unclear²⁹⁷.



The toxin-resistant effect of PBM has been described as a secondary effect of PBM that gets activated after an increase in CIV function through mechanisms such as neuroprotective effect from a surplus of ATP²⁷⁸ and activation of antioxidative pathways^{140,144}. However, since we did not detect an immediate increase in CIV function, the increased Azd resistance observed cannot

be the product of the change in CIV function. Based on this temporal characteristic of response, we speculate that the change in Azd resistance occurs independently of CIV functional changes. The same logic can be applied to increase in biological non-mitochondrial oxygen consumption (that we attributed to the decreased chemical background). Of course, further investigations focusing on PBM's effect on the CIV inhibitor resistance and NOX activity should be conducted before we are sure of their involvement in PBM.

As stated before, a conclusive interpretation of CIV function data is difficult since more than one factors may contribute to observed changes/lack of changes. For example, no observed changes in corrected CIV respiration in real-time cells exposed to 6.37mW/cm² light may be a net result of changes in (1) CIV function (2) Azd resistance and (3) non-mitochondrial oxygen consumption by PBM. Admittedly, we cannot comment on the degree of contributions from each of the mechanisms; nonetheless, the identification of their simultaneous involvement in PBM is a novel information in itself.



CIV. (D) Decreased chemical background observed with high light dose could be explained by increased oxygen consumption from non-mitochondrial consumers of oxygen, such as NOX. (E) Increased chemical background observed with low light dose could be explained by increased Azd resistance. Note that (A-E) are not mutually exclusive.

5.5 CONCLUSION

While mitochondrial involvement in PBM is frequently mentioned in literature and implicitly assumed in most of the recent studies focusing on clinical benefits of PBM, the evidence studying mitochondrial function in PBM are relatively inadequate; there are conflicting reports in even one of the most basic mitochondrial effect (change in CIV function) and many of the studies were using traditional Clark-type electrodes without properly addressing the inherent shortcomings of the technique. Here, we demonstrated a detailed account of mitochondrial changes in response to a single 670nm light exposure immediately after the light exposure to 24h after the exposure.

We report PBM's ability to change two observable parameters of mitochondrial function as measured by O2k respirometry: the TMPD-induced respiration and chemical background measured after Azd titration. We propose a mechanism of PBM that can accommodate our observation. A single 670nm light exposure causes (1) photodissociation of NO from nitrosyl complexes and upregulation of iNOS activities that results in decreased CIV function, (2) CIV-independent increase in Azd resistance at CIV that results in increase in chemical background, and (3) increased oxygen consumption from biological and non-mitochondrial sources that results in decreased chemical background. As this is a preliminary study, a future study that

looks to acquire a comprehensive picture of change in NO level, light-induced Azd resistance, and non-mitochondrial targets should be carried out before producing a convincing conclusion regarding the role of mitochondria in PBM.

6 DISCUSSION

6.1 VIABILITY OF RESPIROMETER FOR OCULAR TISSUES

Despite the rising popularity of mitochondria as a research target in ocular diseases, very small number of studies has investigated the retinal mitochondrial function – due, in part, to lack of adequate research methods. Traditional Clark-type electrode setups require a relatively large amount of tissue for analysis, which has been difficult to accomplish with rodent models' retinae. Furthermore, authors of the studies using traditional Clark-type electrodes and similar oxygen-sensitive electrode^{298,299} failed to discuss key experimental shortcomings such as inherent oxygen consumption by the electrode, temperature control, or oxygen back-diffusion in the experimental chamber³⁴. Recently, studies have instead used the Seahorse XF Analyzer by Agilent Technology^{187,300} which uses phosphorescent oxygen-probe and an optical sensor for oxygen detection. Compared to conventional Clark-type electrodes, XF Analyzer allow higher-throughput method to assess relative differences between samples studied but are limited by small and not well-defined chamber volume, high oxygen back-diffusion through chamber material (plastic), and relatively crude temperature and oxygen control. This problem is compounded by flawed titration protocol often used with XF Analyzer, such as large one-step titration of uncoupler¹⁸⁷.

The O2k circumvents most of these limitations in addition to yielding high-precision of temporal and spatial resolutions of oxygen flux with extensive experimental flexibility. Although, as is the case with other variants of Clark-type electrodes, the O2k still does require a relatively

large amount of sample compared to XF Analyzer. For successful assessment of mitochondrial function with oxygraph, a sample tissue must be able to: (1) have oxygen flux above the detection limit of the polarographic sensors, (2) have a permeabilized membrane to allow access of substrates and inhibitor to mitochondria while (3) still maintaining enough mitochondrial integrity. In this thesis, we demonstrate, for the first time, that O2k can be utilized to functionally assess the specific mitochondrial respiratory system complexes in the retina as well as in RPE cells.

The Nile rat retina studied in **Chapter 3** were mechanically permeabilized and suspended in MiR05 medium for O2k investigation. Firstly, the coupling was such that even the smallest respiration states produced signal well above the detection limit of the machine (~ 1.00 pmol/s·mL where the detection limit was 0.01 pmol/s·mL). Secondly, addition of substrates that are normally impermeable to the cell membrane (such as succinate) elicited a response in mitochondrial respiration; demonstrating that the cell membranes have been permeabilized. Lastly, the preserved mitochondrial integrity supported by the: minimal control of respiration by titration of exogenous cytochrome *c* and high-level of coupling between ETS and phosphorylation system. The coupling is demonstrated by two parameters: low LEAK respiration and readily response to ADP titration. LEAK respiration refers to the respiration associated with ETS activity that are needed to compensate for intrinsic leak of protons from intermembrane space back into the mitochondrial matrix, also known as the intrinsic *uncoupling* of mitochondria. Low LEAK respiration indicates that the majority of the proton gradient created by ETS activity is able to be utilized by the phosphorylation system (i.e. ATP synthesis). Finally, cytochrome *c*, a

mobile electron transporter in ETS that carries electrons between CIII and CIV are peripheral protein in the inner mitochondrial membrane. The outer mitochondrial membrane is normally impermeable to cytochrome *c*. Therefore, a marked increase in respiration after exogenous cytochrome *c* implies mechanical damage²⁸⁵. We did not observe such responses, which further validates the O2k as a tool to assess mitochondrial function in the Nile rat retina.

Along with the retina, mitochondrial activity of Nile rat RPE cells was studied with O2k (*SI 8.1*). In agreement with the lower number of mitochondria present in the eyecup (RPE and sclera), compared to the neural retina⁴⁹, the oxygen consumption was lower for the same respiratory states. In a subset of experiments, the LEAK respiration was below O2k detection threshold. However, the other respiration capacities could be measured reliably while satisfying other parameters mentioned above.

The process of isolating RPE cell monolayer from the eyecup (the structural part of the eye without cornea, lens, aqueous humor, and retina) was impractical given the restricted time available to preserve tissue viability for functional assessment. Therefore, RPEs were studied while still attached to eyecup. Hence, the wet weight of the sample was overestimated. This bias from tissue weight is removed by normalizing the data; for instance, with mitochondrial content (citrate synthase activity) or flux control ratio (FCR). FCR normalization expresses the respiration states as the ratio of the N/Succinate-pathway respiration state (ETS respiration). The number of titrations required to obtain N/Succinate-pathway respiration cannot be achieved with the XF analyzer or traditional Clark-type electrodes. In this sense, O2k represents an invaluable approach for functional study of RPE mitochondria.

In *Chapter 4*, RPE from the ELOVL4 mouse model of STGD3 and their WT littermates was studied. During the preliminary experiments, the respiration data (especially the RPE) was consistently contaminated by residual inhibitor from previous experiments. It is likely that the small number of mitochondria present in the O2k chamber made them more susceptible to contamination. Illustrating this, retina tissues (richer in mitochondria than RPE) were typically free of such contamination issue. Furthermore, experiments undertaken with the same cleaning protocol did not display any contamination issues in 12mo C57 animals (*SI 8.2*) or Nile rats; presumably due to more tissue (and thus mitochondria) available for study. To overcome this issue, we opted to pool two animals of the same genotype from the same litter, but it should be noted that the contamination issues are independent of the O2k sensors' sensitivity; with extensive day-long cleaning protocol, the respiration of RPE collected from a single 1mo C57 animal could reliably be measured. Otherwise, the readings of RPE and retina mitochondria of 1mo, and 12mo C57 mice (*SI 8.2*) met the parameters mentioned above.

6.2 TISSUE-SPECIFIC MITOCHONDRIAL RESPONSES

Eye's mitochondrial populations are strategically concentrated in the areas of high energy demand, such as inner segment of photoreceptors, corneal endothelium, and RPE^{47,49}. The function of cells in these areas are quite distinct from one another (respectively, maintenance of dark current, maintenance of corneal fluid level, and multitude of activities such as regulation of subretinal space and supporting the photoreceptor); therefore, it is reasonable to expect their mitochondria to have different respiratory capacity and biochemical properties from one another,

as well. The differences in mitochondrial characteristics among tissues in the same organs have been reported in different areas of liver³⁰¹, cardiac fibers³⁰², and brain³⁰³. However, such differences within the eye have not been investigated. In this thesis, we report marked differences in the retina and RPE mitochondrial respiratory capacities in animal models – both in their function under physiological conditions, as well as how they respond to disruptions such as hyperglycemic stress and aging.

The respiration capacities expressed in flux per mass (pmol/s·mg) were lower in RPE compared to the retina in all types of respiration capacities examined (*SI 8.1-2*). This is expected since the mitochondria concentration in RPE is smaller than that of PIS^{49,55}. However, the lower respiration reported was exaggerated to a certain extent by the tissue preparation process, also. During the dissection of the enucleated eye, isolating the RPE cell monolayer from the ‘eyecup’ (the structural part of the eye following removal of the cornea, lens, aqueous humor, and retina), while possible³⁰⁴, was impractical given the time limitation imposed to study fresh mitochondria. Therefore, the RPE were studied while still attached to the rest of the eyecup and wet weight of the sample was much higher than the isolated RPE alone would have been. To address this bias, the respiration data were expressed in a normalized form that is independent of tissue weight and mitochondrial content prior to the analysis.

However, even after the data was expressed in FCR (method of internal normalization by expressing respiration in ratio to ETS respiration), the respiration capacities were different between the tissues. That is, the mitochondria at these two sites differ at a more fundamental level than just the number of them present. Most notably, Succinate-pathway respiration in RPE

was higher compared to that of retina (for all groups in both animal models). The ratio of Succinate-pathway to NADH-pathway respiration. This may be related to the concept of *FADH2 and NADH ratio (F/N ratio)* proposed by Speijer³⁰⁵ that proposes a theoretical framework where a large electron flow to ETS from Succinate-pathway could cause congestion at Q-junction and constrains electron flow from CI and ultimately increases the ROS production at CI. While the data here cannot produce any conclusive statements regarding the net amount of ROS production in retina versus RPE in disease states, it suggests that individual RPE mitochondria may have a higher ROS production at CI due to congested flow through the ETS compared to retina.

In addition to displaying different respiratory capacities in physiological conditions, the ways the mitochondria of each tissue respond to disease conditions were also different. The diabetic Nile rats' retinal mitochondrial function underwent a number of modifications, as discussed in Chapter 3. In contrast, the respiratory capacities of RPE remained unchanged between diet groups. The more pronounced changes in retina compared to RPE fit the convention that DR is a disease of inner retinal vasculature¹⁶⁹. However, the age-related changes in mitochondrial function were more pronounced in RPE compared to retina. The only age-related changes seen in retina were in NADH-pathway of diabetic animals; whereas in RPE, LEAK capacity, NADH-pathway, and Succinate-pathway showed differences at various age points of diabetic animals. The differences between age points were seemingly random and it is difficult to speculate their significances or causes. Nonetheless, the marked difference in the responses of mitochondria of two neighboring tissues may indicate a large difference between the outer and inner retinal environments as diabetic animals experience systemic disturbances.

The photoreceptor mitochondria are located away from their soma, as described by Stone et al⁴⁹. This may explain the higher susceptibility of the retina to systemic hyperglycemic insults compare to RPE cells. The 50-100µm distance between the nuclear genome and mitochondria in photoreceptors, might impede the nuclear-originating mechanisms of mitochondrial repair⁶¹, and thus explain the higher susceptibility of mitochondria to homeostatic insults such as oxidative stress. Another contributing factor to this susceptibility may be simply the high density of mitochondria¹⁷² present in retina, where ROS production could easily be amplified to neighboring mitochondria, as critical mass of uranium would in a nuclear chain-reaction.

The retina and RPE from ELOVL4 TG mice also displayed difference in how their function changed during the disease progression, though the interpretation of the difference is not analogous to the Nile rat's. In ELOVL4 TG animals, the only change observed in the mitochondrial function was at 12mo, well-past the onset of photoreceptor cell death at 2mo²³³, where Succinate-pathway respiration increased in RPE mitochondria while retina mitochondria remained the same. In Nile rats, the differences in retina and RPE mitochondrial responses were attributed to the differences in the environment each tissue reside in and the arrangement of the mitochondria in the tissue since the principal cause of cellular damages, hyperglycemia, is present systemically.

6.3 MITOCHONDRIAL INVOLVEMENT IN OCULAR DISEASES

Mitochondrial generation of ROS and its overall contribution to the oxidative stress are a feature commonly reported in wide range of diseases. Examples include diabetes¹⁶, diabetes-

induced complications¹⁷, neurodegenerative diseases such as Parkinson's¹⁸ and Alzheimer's¹⁹ as well as non-pathological aging²⁰. When in excess, ROS can overwhelm the cellular anti-oxidant system and cause biochemical damages on lipids, protein, and DNA, and so on. One notable feature of mitochondria is that while they are important sources of cellular ROS, they are also a prominent target. That is, ROS can cause damages in mitochondrial ETS machinery and mtDNA and exacerbate the ROS production and vice versa. This leads to the *vicious cycle* model of mitochondrial ROS production. In this model, once a threshold level of mitochondrial oxidative damage has occurred, a positive feedback loop of ROS production and mitochondrial damage occurs, leading to a progressive increase in oxidative stress and the eventual cell death.

Despite the frequent mention of the vicious cycle of mitochondrial ROS generation in the literatures^{25,67}, the fact that the presence of mitochondrial dysfunction and/or increase in mitochondrial ROS production do not guarantee the mitochondria as a significant contributor of disease pathogenesis is often overlooked. In other words, the mitochondria's dual role as both the target and source of ROS does not necessarily translate to mean that the mitochondria are both the target and trigger of the disease. In the current project, we examined the mitochondria of DR and STGD3 animal models, with the goals of studying the relationship of mitochondrial function changes and disease development.

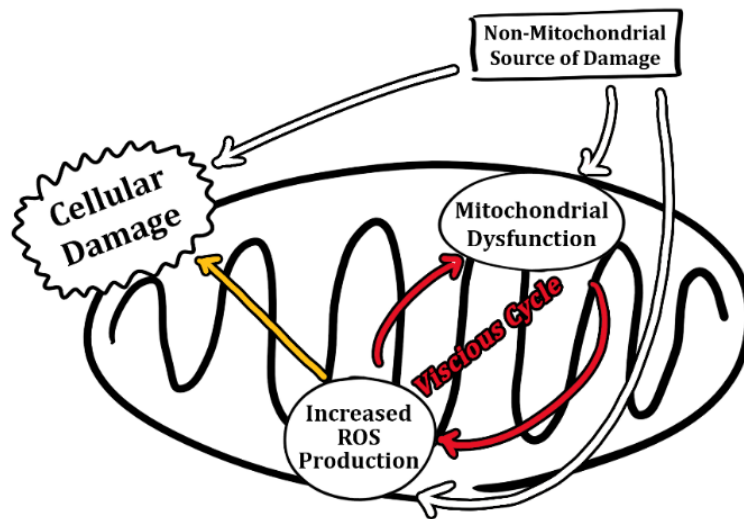


Figure 6.1 A simplified schema of mitochondrial role in non-primary mitochondrial diseases. The vicious cycle of mitochondrial ROS production is often described in various diseases. Ex-mitochondrial source of damage causes mitochondrial damage and dysfunction, which subsequently causes increased mitochondrial ROS production. Increased ROS then further exaggerates mitochondrial dysfunction and ROS production. The increased oxidative stress then attacks cellular targets.

In the study of DR in Nile rat model of retina, the mitochondrial changes in 2mo diabetic animals are reported. The novel discovery of the study was that the increased NADH-pathway respiration and decreased mitochondrial outer membrane integrity not only preceded the clinical manifestation of DR such as pericyte loss at 12mo and vascular and ERG changes in 18mo, but even the development of systemic hyperglycemia in the animals fed with diabetes-inducing diet at 6mo, also. Of course, this does not suggest that the mitochondrial function changes are the very first event of the DR development, since the 2mo animals on a diabetic diet having normoglycemic fasting blood glucose (i.e. below 5.6 mmol/L) does not exclude the possibility of hyperglycemic biochemical pathways activation⁷⁵. Still, such early disturbances in mitochondria

that persists and progressively develops in the later stages of the disease strongly suggest the mitochondria as a causal agent in DR development. Furthermore, the result agreed with the conventional mitochondria-centric mechanism of DR where hyperglycemia-induced damages cause inhibition of mitochondrial antioxidative capabilities and this in turn leads to increased mitochondrial damage, dysfunction, and ROS production⁶⁷.

In contrast, the RPE mitochondrial functions were intact in the ELOVL4 transgenic model of STGD3. Earlier study by our lab reported a normal lipofuscin level at 1mo increasing at 3mo to 10% higher²³⁶. Lipofuscin accumulation and mitochondrial dysfunctions are often described as linked to each other, with implicit understanding that lipofuscin accumulation causes significant increase in oxidative stress which then damages the mitochondria²³⁷. Accordingly, our earlier studies observed abnormal morphology of RPE mitochondria with the increased lipofuscin^{233,236}, but we failed to see any changes in mitochondrial function. The mitochondrial function remained unchanged until 12mo, long after the onset of photoreceptor cell death, with increased Succinate-pathway respiration, that may indicate enhanced ROS production^{305,306}. Since mitochondrial dysfunction lagged behind signs of cellular damage, it is unlikely that the mitochondria played a significant causal role as they seemingly do in DR. That is, the role of mitochondria in STGD3 is likely as a target rather than the trigger.

6.4 COMMENTING ON THE EFFICACY OF PBM

As the last part of this thesis, we examined the changes in mitochondrial function in PBM. We presented a preliminary evidence suggesting that NIR light exposure induces three distinct

changes in mitochondrial function. While the purpose of the study was to investigate the mechanistical changes in mitochondrial function, we provide a conceptual rationale regarding potential benefits of PBM in the treatment of DR and STGD3.

The high interest in mitochondria as a therapeutic target arose based on observations that the mitochondrial dysfunction and mitochondrial generation of ROS are commonly seen in wide range of diseases. Targeting mitochondrial function makes sense if doing so can address the causal element in the disease development. In our study of DR, the retinal mitochondrial changes were remarkably early and preceded even the onset of systemic hyperglycemia. Such early changes in mitochondria fits the well-subscribed narrative³⁰⁷ of vicious cycle of perpetual ROS production, mitochondrial damage, and dysfunction.

Mitochondrial OXPHOS activity entails an inevitable production of ROS^{13,21}, therefore, increased mitochondrial activity is associated with increased mitochondrial ROS generation³⁰⁸. Especially in hyperglycemic environment, mitochondrial ROS generation reportedly is a significant component of net oxidative stress^{28,75}. Therefore, reducing mitochondrial CIV function through PBM could result in decreased oxidative stress, and subsequently alleviate the cellular damages vascular dysfunctions observed in DR. Decreased CIV function, reportedly mediated via NO-mediated mechanism²⁸⁶⁻²⁸⁹ would lead to following sequence of events:

- (1) Mitochondrial activity is reduced,
- (2) Increased inherent ROS production, often seen in hyperglycemic conditions, is avoided,
- (3) Further mitochondrial damages by ROS does not occur,

(4) The vicious cycle of exaggerated ROS production and mitochondrial damage is not activated, and,

(5) The chronic production of oxidative stress that results in vascular damage is averted.

This CIV-related effect may exist independently of other reported effects of PBM such as decreased ICAM-1 expression^{157,158} and HO-1 expression³⁰⁹. We proposed that a reduced activity of NOX, a non-mitochondrial consumer of oxygen²⁹⁵, may explain the observed decreased chemical background following NIR light exposure. NOX activities have been implicated in diabetes-induced cellular damages³¹⁰ and DR pathogenesis^{311,312}. To sum up, PBM could be beneficial to DR by reducing CIV function and reducing NOX activities and ultimately decrease the oxidative stress.

In contrast, the rationale for applying PBM in STGD3 is less explicit. Mitochondrial function was not affected in RPEs of animal model until they have reached the terminal stage of the disease development. Previous experiments by our lab showed increased lipofuscin level after the onset of photoreceptor cell death and histological changes in mitochondria^{233,236}. However, this evidently was not enough to induce detectable mitochondrial dysfunction. It is, therefore, unlikely that mitochondria-targeting therapy will be effective in treatment of STGD3.

One scenario that PBM may attenuate symptoms of STGD3 is if PBM could increase ATP availability. Many studies, especially those that focus on clinical efficacy of PBM, report that ATP content is increased in response to NIR light exposure¹²¹. The magnitude of ATP increase elicited by PBM ranges from 20% to even 3-fold compared to appropriate control^{278,279}. Such a

large increase is hard to believe and our observed decrease in CIV function does not support these reports. Perhaps the increased ATP content occurs independently of changes in CIV or reflection of higher cell survival. Regardless, if true, the PBM-induced increase in ATP can activate numerous neuroprotective effects such as increase in glutamate reuptake³¹³, activation of P2X7 channels (normally associated with apoptosis pathway³¹⁴, but can have neuroprotective effect³¹⁵), and activation of ATP-sensitive K⁺ (K_{ATP}) channels³¹⁶. The last point is especially interesting, since K_{ATP} channels seem to be positively modulated by NO-signaling³¹⁷ and is being investigated in context of PBM already^{318,319}. Additionally, it is possible that excess of ATP may facilitate ATP-dependent steps of POS phagocytosis by RPE such as acidification of phagosomes and transport of phagosome from apical to basal membrane of RPE³²⁰. In summary, PBM may still be a viable therapeutic option for treatment of STGD3 despite the fact that the mitochondrial dysfunction does not seem to play a causal role in the disease pathogenesis.

7 CONCLUSION

7.1 SIGNIFICANCE

We present pioneering accounts of utilization of O2k respirometers in the study of the ocular mitochondria collected from the rodent models. Even though mitochondrial involvement is suggested in many prominent ocular diseases, thus far, we lacked a reliable method that can provide detailed functional assessment of ocular mitochondria. Therefore, the protocol demonstrated in this thesis is highly valuable – even without the novel findings we report.

In our study of DR, we report early mitochondrial functional changes that preceded clinical signs of DR as well as the onset of hyperglycemia in retina. Retinal functional changes continued to develop as diet-induced diabetes progressed, while RPE mitochondria remained functionally unchanged. Our findings corroborate a conventional notion that the mitochondria of photoreceptors play a causal role in DR pathogenesis and demonstrate that *A. niloticus* may serve as a viable model of DR. In our study of STGD3, the functional aspects of retina and RPE mitochondria were preserved even long after the onset of photoreceptor cell death. Therefore, we propose that the ocular mitochondria in STGD3 do not directly contribute to the cellular damages; but rather are victims of other sources of damage such as dysfunctional phagocytosis process. The contrasting roles of mitochondria in two disease models suggests that even when oxidative stress is implicated in the disease pathogenesis, mitochondrial involvement cannot be implicitly assumed.

As the last segment of this thesis, we investigated PBM as a potential treatment for mitochondrial dysfunction. We present a detailed report of NIR light-induced mitochondrial functional changes using O2k. The observed functional changes could not be adequately explained by the currently accepted mechanism of PBM. Hence, we propose an alternate mechanism that can explain our findings. Lastly, we present possible rationales for applying PBM in treatment of DR and STGD3.

7.2 LIMITATIONS

1. Our Nile rat colony originated from 29 animals. We were not able to introduce outside animals to our colony during the multi-year period of colony operation. Therefore, some of the phenotype observed may have been influenced by inbreeding and unintentional selection bias for animals that resisted diabetes development even when in captivity and exposed to high-fat diet.
2. Due to the limited time available to study mitochondrial function from freshly dissected tissues, the enucleated eyes were not dissected to individual cell types. Therefore, the retina and RPE studied contained heterogeneous cell types (retina - bipolar cells, Muller cells, retinal ganglion cells, photoreceptor cells, as well as central retinal arteries; eyecup - RPE and sclera).

3. A single rodent could not provide adequate amount of tissue to allow further biochemical analysis and O2k respirometry. Coupled with the limited time-frame of the study, we could not perform extensive examinations of oxidative stress.
4. The CIV function was assessed using titrations of As, TMPD, and Azd. Unexpectedly, PBM could modulate Azd resistance and non-mitochondrial oxygen consumption, which interfered with a precise assessment of CIV function during the PBM study.

7.3 FUTURE DIRECTIONS

More in-depth investigation of oxidative stress will be highly valuable complement to the data present in this thesis. Given the limited amount of tissue that can be obtained from each animal, a larger study with more animals may be needed. Alternatively, an add-on equipment to the O2k respirometer that allows simultaneous measurement of mitochondrial superoxide production using optical measurement³²¹ could allow efficient use of the ocular tissues.

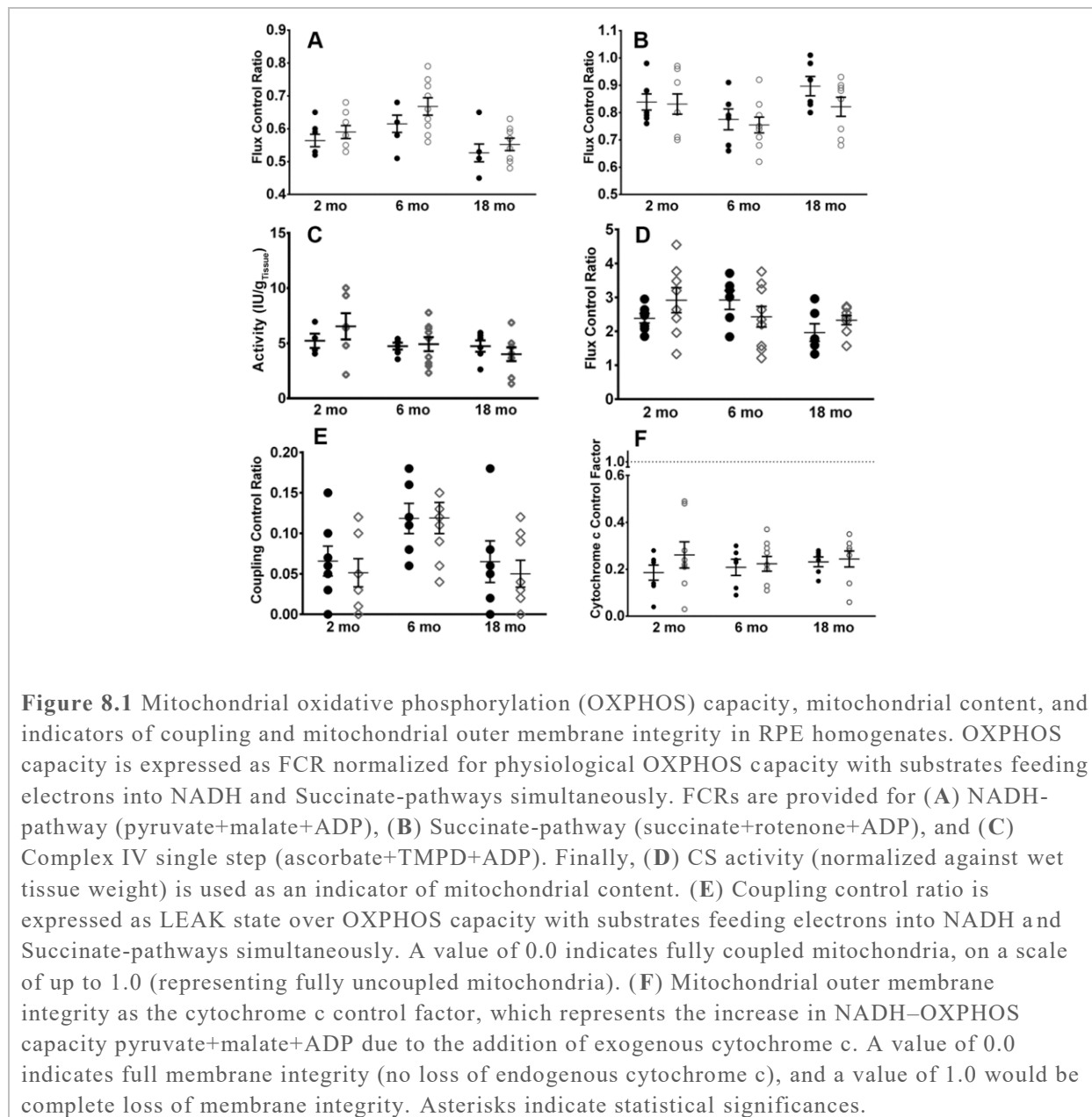
Further investigation of PBM as mitochondria-targeting treatment option is a reasonable next step for this thesis. We suggest that future research should focus on two large aspects of PBM: (1) A further investigation of the biochemical mechanism of PBM, including changes in NO, changes in CIV's Azd resistance, and changes in activities of non-mitochondrial oxygen consumption would. (2) A study that focuses on if/how the biochemical changes translate to therapeutic improvements in DR and STGD3 animal models. Doing so, we will be able to

evaluate the therapeutic potentials of PBM more effectively, compared to the inductive approach seen in contemporary PBM studies.

8 SUPPORTING INFORMATION

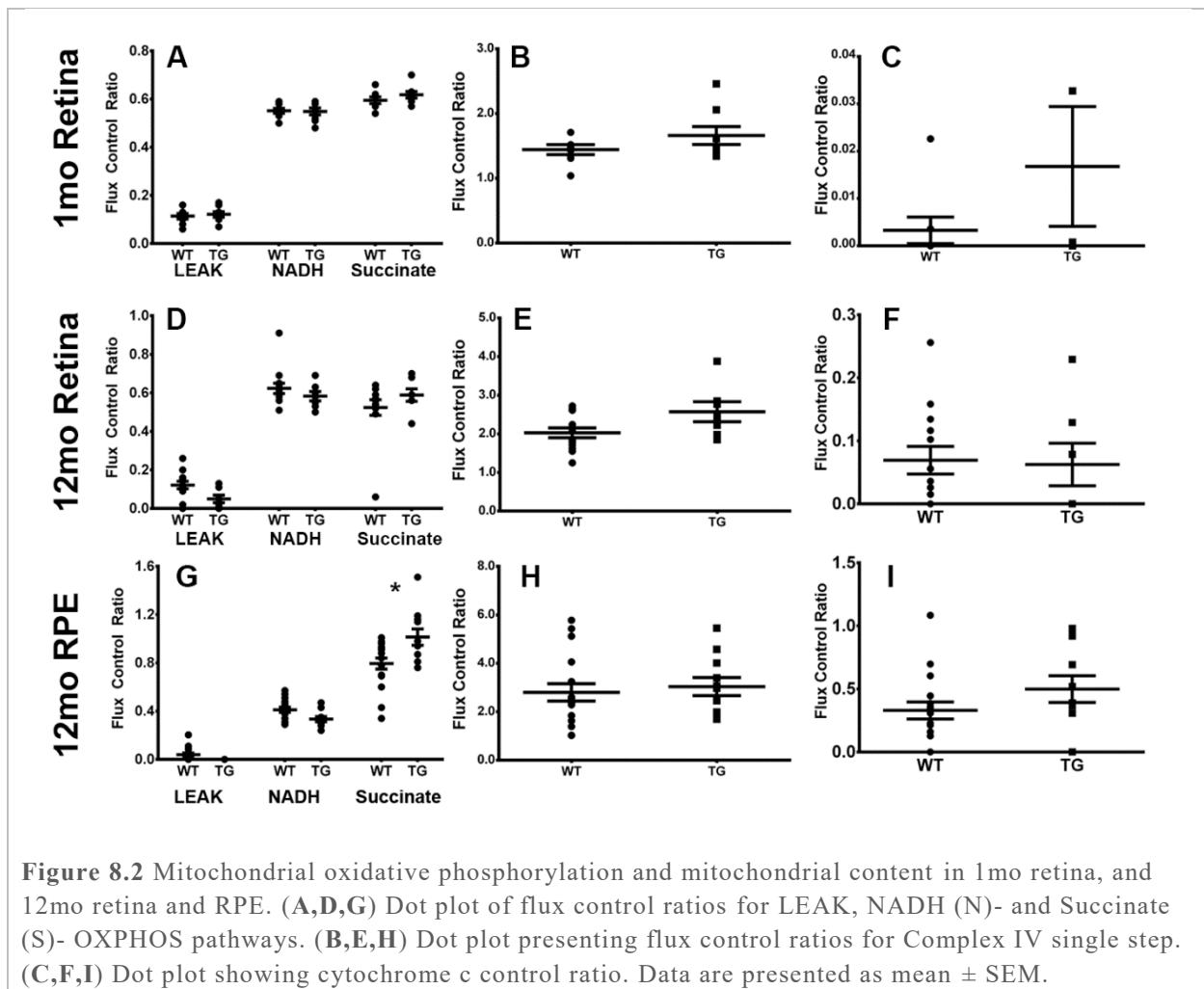
Additional data not included in the published articles^{1,2} are shown below.

8.1 ADDITIONAL NILE RAT MITOCHONDRIAL DATA



No differences between RPE mitochondrial function between control and diabetic diet animals were observed at any of the parameters investigated. However, when compared to the same animals' retina, the Succinate-pathway respiration was always higher in the RPE (retina vs. RPE of 2mo Maz/Pro, 6mo Maz/Pro, and 18mo Maz/Pro; 0.542 ± 0.00956 vs. 0.823 ± 0.0348 , 0.498 ± 0.0102 vs. 0.830 ± 0.0369 , 0.479 ± 0.0112 vs. 0.776 ± 0.0376 , 0.477 ± 0.00996 vs. 0.756 ± 0.0295 , 0.498 ± 0.0102 vs. 0.897 ± 0.0350 , 0.524 ± 0.00956 vs. 0.823 ± 0.0348).

8.2 ADDITIONAL ELOVL4 MICE MITOCHONDRIAL DATA



The 12mo RPE's Succinate-pathway respiration showed increased respiration in TG animals (0.835 ± 0.0357 in WT vs. 0.953 ± 0.0557 in TG). Additionally, consistently higher Succinate-pathway respirations were observed in RPE compared to retina (retina vs. eyecup of 1mo WT/TG, 12 WT/TG; 0.0597 ± 0.0220 vs. 0.859 ± 0.0220 , 0.618 ± 0.0142 vs. 0.795 ± 0.0352 , 0.523 ± 0.0406 vs. 0.823 ± 0.0463 , and 0.591 ± 0.0318 vs. 0.979 ± 0.0612).

REFERENCES

1. Han WH, Gotzmann J, Kuny S, et al. Modifications in Retinal Mitochondrial Respiration Precede Type 2 Diabetes and Protracted Microvascular Retinopathy. *Investig Ophthalmology Vis Sci*. 2017;58(10):3826. doi:10.1167/iovs.17-21929
2. Dejos C, Kuny S, Han WH, Capel H, Lemieux H, Sauvé Y. Photoreceptor-induced RPE phagolysosomal maturation defects in Stargardt-like Maculopathy (STGD3). *Sci Rep*. 2018;8(1):5944. doi:10.1038/s41598-018-24357-4
3. Hockenbery D, Nuñez G, Milliman C, Schreiber RD, Korsmeyer SJ. Bcl-2 is an inner mitochondrial membrane protein that blocks programmed cell death. *Nature*. 1990;348(6299):334-336. doi:10.1038/348334a0
4. Dada L a, Chandel NS, Ridge KM, Pedemonte C, Bertorello AM, Sznajder JI. Hypoxia-induced endocytosis of Na⁺, K-ATPase in alveolar epithelial cells is mediated by mitochondrial reactive oxygen species and PKC- ζ . *Cell*. 2003;111(7):1057-1064. doi:10.1172/JCI200316826.Introduction
5. Severance S, Hamza I. Trafficking of Heme and Porphyrins in Metazoa. *Chem Rev*. 2009;109(10):4596-4616. doi:10.1021/cr9001116
6. Chung J, Chen C, Paw BH. Heme metabolism and erythropoiesis. *Curr Opin Hematol*. 2012;19(3):156-162. doi:10.1097/MOH.0b013e328351c48b
7. Velarde MC. Mitochondrial and sex steroid hormone crosstalk during aging. *Longev Heal*. 2014;3(1):2. doi:10.1186/2046-2395-3-2
8. Contreras L, Drago I, Zampese E, Pozzan T. Mitochondria: The calcium connection. *Biochim Biophys Acta - Bioenerg*. 2010;1797(6-7):607-618. doi:10.1016/j.bbabi.2010.05.005
9. Kalyanaraman B, Cheng G, Hardy M, et al. A review of the basics of mitochondrial bioenergetics, metabolism, and related signaling pathways in cancer cells: Therapeutic targeting of tumor mitochondria with lipophilic cationic compounds. *Redox Biol*. 2018;14:316-327. doi:10.1016/j.redox.2017.09.020
10. Beckner ME, Gobbel GT, Abounader R, et al. Glycolytic glioma cells with active glycogen synthase are sensitive to PTEN and inhibitors of PI3K and gluconeogenesis. *Lab Invest*. 2005;85(12):1457-1470. doi:10.1038/labinvest.3700355
11. Hackenbrock CR. Lateral diffusion and electron transfer in the mitochondrial inner membrane. *Trends Biochem Sci*. 1981;6:151-154. doi:10.1016/0968-0004(81)90056-6
12. Dudkina N V., Kouřil R, Peters K, Braun HP, Boekema EJ. Structure and function of mitochondrial supercomplexes. *Biochim Biophys Acta - Bioenerg*. 2010;1797(6-7):664-670. doi:10.1016/j.bbabi.2009.12.013
13. Dröse S, Brandt U. Molecular Mechanisms of Superoxide Production by the Mitochondrial

- Respiratory Chain. In: Vol 748. ; 2012:145-169. doi:10.1007/978-1-4614-3573-0_6
14. Birben E, Murat U, Md S, Sackesen C, Erzurum S, Kalayci O. Oxidative Stress and Antioxidant Defense. *WAO J.* 2012;5(January):9-19. doi:10.1097/WOX.0b013e3182439613
 15. Gandhi S, Abramov AY. Mechanism of oxidative stress in neurodegeneration. *Oxid Med Cell Longev.* 2012;2012. doi:10.1155/2012/428010
 16. Martin SD, McGee SL. The role of mitochondria in the aetiology of insulin resistance and type 2 diabetes. *Biochim Biophys Acta.* 2014;1840(4):1303-1312. doi:10.1016/j.bbagen.2013.09.019
 17. Lee KU, Harris RA. Mitochondria and endoplasmic reticulum in diabetes and its complications. *Exp Diabetes Res.* 2012;2012:2012-2014. doi:10.1155/2012/985075
 18. Kumar MJ, Nicholls DG, Andersen JK. Oxidative α -Ketoglutarate Dehydrogenase Inhibition via Subtle Elevations in Monoamine Oxidase B Levels Results in Loss of Spare Respiratory Capacity. *J Biol Chem.* 2003;278(47):46432-46439. doi:10.1074/jbc.M306378200
 19. Aslan M, Ozben T. Reactive Oxygen and Nitrogen Species in Alzheimers Disease. *Curr Alzheimer Res.* 2004;1(2):111-119. doi:10.2174/1567205043332162
 20. Balaban RS, Nemoto S, Finkel T. Mitochondria, oxidants, and aging. *Cell.* 2005;120(4):483-495. doi:10.1016/j.cell.2005.02.001
 21. Korshunov SS, Skulachev VP, Starkov AA. High protonic potential actuates a mechanism of production of reactive oxygen species in mitochondria. *FEBS Lett.* 1997;416(1):15-18. doi:10.1016/S0014-5793(97)01159-9
 22. Schapira AH. Mitochondria in the aetiology and pathogenesis of Parkinson's disease. *Lancet Neurol.* 2008;7(1):97-109. doi:10.1016/S1474-4422(07)70327-7
 23. Quinlan CL, Orr AL, Perevoshchikova I V., Treberg JR, Ackrell BA, Brand MD. Mitochondrial Complex II Can Generate Reactive Oxygen Species at High Rates in Both the Forward and Reverse Reactions. *J Biol Chem.* 2012;287(32):27255-27264. doi:10.1074/jbc.M112.374629
 24. Starkov AA, Andreyev AY, Zhang SF, et al. Scavenging of H₂O₂ by mouse brain mitochondria. *J Bioenerg Biomembr.* 2014;46(6):471-477. doi:10.1007/s10863-014-9581-9
 25. Hiona A, Leeuwenburgh C. The role of mitochondrial DNA mutations in aging and sarcopenia: Implications for the mitochondrial vicious cycle theory of aging. *Exp Gerontol.* 2008;43(1):24-33. doi:10.1016/j.exger.2007.10.001
 26. Brown GC, Borutaite V. There is no evidence that mitochondria are the main source of reactive oxygen species in mammalian cells. *Mitochondrion.* 2012;12(1):1-4. doi:10.1016/j.mito.2011.02.001
 27. Boveris A, Oshino N, Chance B. The cellular production of hydrogen peroxide. *Biochem J.* 1972;128(3):617-630. doi:10.1042/bj1280617

28. Madsen–Bouterse SA, Mohammad G, Kanwar M, Kowluru RA. Role of Mitochondrial DNA Damage in the Development of Diabetic Retinopathy, and the Metabolic Memory Phenomenon Associated with Its Progression. *Antioxid Redox Signal*. 2010;13(6):797-805. doi:10.1089/ars.2009.2932
29. Onyango I. Modulation of mitochondrial bioenergetics as a therapeutic strategy in Alzheimer’s disease. *Neural Regen Res*. 2018;13(1):19. doi:10.4103/1673-5374.224362
30. Madsen-Bouterse SA, Zhong Q, Mohammad G, Ho Y-S, Kowluru RA. Oxidative damage of mitochondrial DNA in diabetes and its protection by manganese superoxide dismutase. *Free Radic Res*. 2010;44(3):313-321. doi:10.3109/10715760903494168
31. Vásquez-Vivar J, Kalyanaraman B, Kennedy MC. Mitochondrial Aconitase Is a Source of Hydroxyl Radical. *J Biol Chem*. 2000;275(19):14064-14069. doi:10.1074/jbc.275.19.14064
32. Claus C, Schonefeld K, Hubner D, Chey S, Reibetanz U, Liebert UG. Activity Increase in Respiratory Chain Complexes by Rubella Virus with Marginal Induction of Oxidative Stress. *J Virol*. 2013;87(15):8481-8492. doi:10.1128/JVI.00533-13
33. Sen S, Kawahara B, Chaudhuri G. Mitochondrial-associated nitric oxide synthase activity inhibits cytochrome c oxidase: Implications for breast Cancer. *Free Radic Biol Med*. 2013;57:210-220. doi:10.1016/j.freeradbiomed.2012.10.545
34. Madeira VMC. *Overview of Mitochondrial Bioenergetics*. Vol 810.; 2012. doi:10.1007/978-1-61779-382-0_1
35. Willingham TB, McCully KK. In vivo assessment of mitochondrial dysfunction in clinical populations using near-infrared spectroscopy. *Front Physiol*. 2017;8(SEP). doi:10.3389/fphys.2017.00689
36. Lemieux H, Blier PU, Gnaiger E. Remodeling pathway control of mitochondrial respiratory capacity by temperature in mouse heart: electron flow through the Q-junction in permeabilized fibers. *Sci Rep*. 2017;7(1):2840. doi:10.1038/s41598-017-02789-8
37. Gnaiger E. Mitochondrial respiratory control : a conceptual perspective on coupling states in mitochondrial preparations. 2017:1-38.
38. NICHOLLS DG. The Effective Proton Conductance of the Inner Membrane of Mitochondria from Brown Adipose Tissue. Dependency on Proton Electrochemical Potential Gradient. *Eur J Biochem*. 1977;77(2):349-356. doi:10.1111/j.1432-1033.1977.tb11674.x
39. Babior BM. NADPH oxidase. *Curr Opin Immunol*. 2004;16(1):42-47. <http://www.ncbi.nlm.nih.gov/pubmed/14734109>.
40. Gnaiger E. *Mitochondrial Pathways and Respiratory Control An Introduction to OXPHOS Analysis*.; 2014. http://wiki.oroboros.at/images/f/fc/Gnaiger_2014_Mitochondr_Physiol_Network_MitoPathways.pdf.

41. Leung BK, Bonanno JA, Radke CJ. Oxygen-deficient metabolism and corneal edema. *Prog Retin Eye Res.* 2011;30(6):471-492. doi:10.1016/j.preteyeres.2011.07.001
42. Ames A, Li YY, Heher EC, Kimble CR. Energy metabolism of rabbit retina as related to function: high cost of Na⁺ transport. *J Neurosci.* 1992;12(3):840-853. doi:10.1523/JNEUROSCI.12-03-00840.1992
43. LaVail MM. Rod outer segment disk shedding in rat retina: relationship to cyclic lighting. *Science.* 1976;194(4269):1071-1074. <http://www.ncbi.nlm.nih.gov/pubmed/982063>.
44. Raichle ME, Gusnard DA. Appraising the brain's energy budget. *Proc Natl Acad Sci.* 2002;99(16):10237-10239. doi:10.1073/pnas.172399499
45. Specht SC, Sweadner KJ. Two different Na,K-ATPases in the optic nerve: cells of origin and axonal transport. *Proc Natl Acad Sci.* 1984;81(4):1234-1238. doi:10.1073/pnas.81.4.1234
46. Niven JE, Laughlin SB. Energy limitation as a selective pressure on the evolution of sensory systems. *J Exp Biol.* 2008;211(11):1792-1804. doi:10.1242/jeb.017574
47. Ng SK, Wood JPMM, Chidlow G, et al. Cancer-like metabolism of the mammalian retina. *Clin Exp Ophthalmol.* 2015;43(4):367-376. doi:10.1111/ceo.12462
48. Winkler BS, Arnold MJ, Brassell MA, Puro DG. Energy metabolism in human retinal Müller cells. *Invest Ophthalmol Vis Sci.* 2000;41(10):3183-3190. <http://www.ncbi.nlm.nih.gov/pubmed/10967082>.
49. Stone J, van Driel D, Valter K, Rees S, Provis J. The locations of mitochondria in mammalian photoreceptors: Relation to retinal vasculature. *Brain Res.* 2008;1189(1):58-69. doi:10.1016/j.brainres.2007.10.083
50. Kolb H, Nelson R, Fernandez E JB. Simple Anatomy of the Retina. *Webvision Organ Retin Vis Syst.* 2011:1-9. http://journals.lww.com/international-ophthalmology/Citation/1981/02130/Anatomy_and_Histopathology_of_the_Macular_Region.3.aspx.
51. Hurley JB, Lindsay KJ, Du J. Glucose, lactate, and shuttling of metabolites in vertebrate retinas. *J Neurosci Res.* 2015;93(7):1079-1092. doi:10.1002/jnr.23583
52. Chinchore Y, Begaj T, Wu D, Drokhlyansky E, Cepko CL. Glycolytic reliance promotes anabolism in photoreceptors. *Elife.* 2017;6:1-22. doi:10.7554/eLife.25946
53. Kumagai AK, Glasgow BJ, Pardridge WM. GLUT1 glucose transporter expression in the diabetic and nondiabetic human eye. *Invest Ophthalmol Vis Sci.* 1994;35(6):2887-2894. <http://www.ncbi.nlm.nih.gov/pubmed/8188484>.
54. Sánchez-Chávez G, Peña-Rangel MT, Riesgo-Escovar JR, Martínez-Martínez A, Salceda R. Insulin Stimulated-Glucose Transporter Glut 4 Is Expressed in the Retina. *PLoS One.* 2012;7(12):1-7. doi:10.1371/journal.pone.0052959

55. Kur J, Newman EA, Chan-Ling T. Cellular and physiological mechanisms underlying blood flow regulation in the retina and choroid in health and disease. *Prog Retin Eye Res.* 2012;31(5):377-406. doi:10.1016/j.preteyeres.2012.04.004
56. Kawamura S, Tachibanaki S. Rod and cone photoreceptors: Molecular basis of the difference in their physiology. *Comp Biochem Physiol - A Mol Integr Physiol.* 2008;150(4):369-377. doi:10.1016/j.cbpa.2008.04.600
57. Jarrett SG, Lin H, Godley BF, Boulton ME. Mitochondrial DNA damage and its potential role in retinal degeneration. *Prog Retin Eye Res.* 2008;27(6):596-607. doi:10.1016/j.preteyeres.2008.09.001
58. Gueven N, Nadikudi M, Daniel A, Chhetri J. Targeting mitochondrial function to treat optic neuropathy. *Mitochondrion.* 2017;36:7-14. doi:10.1016/j.mito.2016.07.013
59. Kanwar M, Chan P-SS, Kern TS, Kowluru RA. Oxidative damage in the retinal mitochondria of diabetic mice: Possible protection by superoxide dismutase. *Investig Ophthalmol Vis Sci.* 2007;48(8):3805-3811. doi:10.1167/iovs.06-1280
60. Youssef PN, Sheibani N, Albert DM. Retinal light toxicity. *Eye (Lond).* 2011;25(1):1-14. doi:10.1038/eye.2010.149
61. Yu Wai Man CY, Chinnery PF, Griffiths PG. Optic neuropathies--importance of spatial distribution of mitochondria as well as function. *Med Hypotheses.* 2005;65(6):1038-1042. doi:10.1016/j.mehy.2004.10.021
62. Chhetri J, Gueven N. Targeting mitochondrial function to protect against vision loss. *Expert Opin Ther Targets.* 2016;20(6):721-736. doi:10.1517/14728222.2015.1134489
63. Barot M, Gokulgandhi MR, Mitra AK. Mitochondrial Dysfunction in Retinal Diseases. *Curr Eye Res.* 2011;36(12):1069-1077. doi:10.3109/02713683.2011.607536
64. Bullon H. N.;Battino, M. P.;Newma. Obesity, diabetes mellitus, atherosclerosis and chronic periodontitis: A shared pathology via oxidative stress and mitochondrial dysfunction? *Periodontol 2000.* 2014;64(1):139-153. doi:10.1111/j.1600-0757.2012.00455.x
65. Chawla A, Chawla R, Jaggi S. Microvascular and macrovascular complications in diabetes mellitus: Distinct or continuum? *Indian J Endocrinol Metab.* 2016;20(4):546. doi:10.4103/2230-8210.183480
66. Antonetti DA, Klein R, Gardner TW. Diabetic Retinopathy. *N Engl J Med.* 2012;366(13):1227-1239. doi:10.1056/NEJMra1005073
67. Kowluru RA, Mishra M. Oxidative Stress, Mitochondrial Damage and Diabetic Retinopathy. *Biochim Biophys Acta.* 2015;1852(11):2474-2483. doi:10.1016/j.bbadis.2015.08.001
68. Klein BEK. Overview of epidemiologic studies of diabetic retinopathy. *Ophthalmic Epidemiol.* 2007;14(4):179-183. doi:10.1080/09286580701396720

69. Romero-Aroca P, Marc Baget-Bernaldiz, Angel Bautista-Perez, Teresa Basora-Gallisa, Josep Basora-Gallisa, Basora-Gallisa. Prospective comparison of two methods of screening for diabetic retinopathy by nonmydriatic fundus camera. *Clin Ophthalmol*. December 2010:1481. doi:10.2147/OPTH.S14521
70. International Diabetes Federation. *IDF Diabetes Atlas 7th Edition.*; 2015. doi:10.1289/image.ehp.v119.i03
71. Heintz E, Wiréhn A-B, Peebo BB, Rosenqvist U, Levin L-Å. Prevalence and healthcare costs of diabetic retinopathy: a population-based register study in Sweden. *Diabetologia*. 2010;53(10):2147-2154. doi:10.1007/s00125-010-1836-3
72. Horal M, Zhang Z, Stanton R, Virkamäki A, Loeken MR. Activation of the hexosamine pathway causes oxidative stress and abnormal embryo gene expression: Involvement in diabetic teratogenesis. *Birth Defects Res Part A - Clin Mol Teratol*. 2004;70(8):519-527. doi:10.1002/bdra.20056
73. Gopalakrishna R, Jaken S. Protein kinase C signaling and oxidative stress. *Free Radic Biol Med*. 2000;28(9):1349-1361. doi:16/S0891-5849(00)00221-5
74. Santos JM, Mishra M, Kowluru RA. Posttranslational modification of mitochondrial transcription factor A in impaired mitochondria biogenesis: Implications in diabetic retinopathy and metabolic memory phenomenon. *Exp Eye Res*. 2014;121:168-177. doi:10.1016/j.exer.2014.02.010
75. Zhong Q, Kowluru RA. Diabetic retinopathy and damage to mitochondrial structure and transport machinery. *Investig Ophthalmol Vis Sci*. 2011;52(12):8739-8746. doi:10.1167/iovs.11-8045
76. Tien T, Zhang J, Muto T, Kim D, Sarthy VP, Roy S. High Glucose Induces Mitochondrial Dysfunction in Retinal Müller Cells: Implications for Diabetic Retinopathy. *Investig Ophthalmology Vis Sci*. 2017;58(7):2915. doi:10.1167/iovs.16-21355
77. Santos JM, Tewari S, Goldberg AFXX, Kowluru RA. Mitochondrial biogenesis and the development of diabetic retinopathy. *Free Radic Biol Med*. 2011;51(10):1849-1860. doi:10.1016/j.freeradbiomed.2011.08.017
78. Du Y, Veenstra A, Palczewski K, Kern TS. Photoreceptor cells are major contributors to diabetes-induced oxidative stress and local inflammation in the retina. *Proc Natl Acad Sci*. 2013;110(41):16586-16591. doi:10.1073/pnas.1314575110
79. Gardiner TA, Stitt AW, Anderson HR, Archer DB. Selective loss of vascular smooth muscle cells in the retinal microcirculation of diabetic dogs. *Br J Ophthalmol*. 1994;78(1):54-60. <http://www.ncbi.nlm.nih.gov/pubmed/8110701>.
80. Tzekov R, Arden G. B. The electroretinogram in diabetic retinopathy. *Surv Ophthalmol*. 1999;44(1):53-60. doi:10.1016/S0039-6257(99)00063-6
81. Ng JS, Barse MA, Schneck ME, Barez S, Adams AJ. Local Diabetic Retinopathy Prediction by Multifocal ERG Delays over 3 Years. *Investig Ophthalmology Vis Sci*. 2008;49(4):1622. doi:10.1167/iovs.07-1157

82. Stem M, Gardner T. Neurodegeneration in the Pathogenesis of Diabetic Retinopathy: Molecular Mechanisms and Therapeutic Implications. *Curr Med Chem*. 2013;20(26):3241-3250. doi:10.2174/09298673113209990027
83. Jiang X, Yang L, Luo Y. Animal Models of Diabetic Retinopathy. *Curr Eye Res*. 2015;40(8):761-771. doi:10.3109/02713683.2014.964415
84. Robinson R, Barathi VA, Chaurasia SS, Wong TY, Kern TS. Update on animal models of diabetic retinopathy: from molecular approaches to mice and higher mammals. *Dis Model Mech*. 2012;5(4):444-456. doi:10.1242/dmm.009597
85. Rabiou S, Rose RK. A quantitative study of diet in three species of rodents in natural and irrigated savanna fields. *Acta Theriol (Warsz)*. 1997;42:55-70. doi:10.4098/AT.arch.97-7
86. Noda K, Melhorn MI, Zandi S, et al. An animal model of spontaneous metabolic syndrome: Nile grass rat. *FASEB J*. 2010;24(7):2443-2453. doi:10.1096/fj.09-152678
87. Subramaniam A, Landstrom M, Luu A, Hayes KC. The Nile Rat (*Arvicanthis niloticus*) as a Superior Carbohydrate-Sensitive Model for Type 2 Diabetes Mellitus (T2DM). *Nutrients*. 2018;10(2):235. doi:10.3390/nu10020235
88. Weir GC, Bonner-weir S. Progression to Diabetes. *Diabetes*. 2004;53(December):34-41.
89. Yang K, Gotzmann J, Kuny S, Huang H, Sauve Y, Chan CB. Five stages of progressive beta-cell dysfunction in the laboratory Nile rat model of type 2 diabetes. *J Endocrinol*. 2016;229(3):343-356. doi:10.1530/JOE-15-0517
90. Blanchong JA, McElhinny TL, Mahoney MM, Smale L. Nocturnal and Diurnal Rhythms in the Unstriped Nile Rat, *Arvicanthis niloticus*. *J Biol Rhythms*. 1999;14(5):364-377. doi:10.1177/074873099129000777
91. Gaillard F, Bonfield S, Gilmour GS, et al. Retinal anatomy and visual performance in a diurnal cone-rich laboratory rodent, the Nile grass rat (*Arvicanthis niloticus*). *J Comp Neurol*. 2008;510(5):525-538. doi:10.1002/cne.21798
92. Gilmour GS, Gaillard F, Watson J, et al. The electroretinogram (ERG) of a diurnal cone-rich laboratory rodent, the Nile grass rat (*Arvicanthis niloticus*). *Vision Res*. 2008;48(27):2723-2731. doi:10.1016/j.visres.2008.09.004
93. Perkins G a, Ellisman MH, Fox D a. Three-dimensional analysis of mouse rod and cone mitochondrial cristae architecture: bioenergetic and functional implications. *Mol Vis*. 2003;9(December 2002):60-73. doi:v9/a10 [pii]
94. Wang Q, Tikhonenko M, Bozack SN, et al. Changes in the Daily Rhythm of Lipid Metabolism in the Diabetic Retina. Tosini G, ed. *PLoS One*. 2014;9(4):e95028. doi:10.1371/journal.pone.0095028
95. Sahel J-A, Marazova K, Audo I. Clinical Characteristics and Current Therapies for Inherited Retinal Degenerations. *Cold Spring Harb Perspect Med*. 2015;5(2):a017111-a017111.

doi:10.1101/cshperspect.a017111

96. Aldahmesh MA, Mohamed JY, Alkuraya HS, et al. Recessive Mutations in ELOVL4 Cause Ichthyosis, Intellectual Disability, and Spastic Quadriplegia. *Am J Hum Genet.* 2011;89(6):745-750. doi:10.1016/j.ajhg.2011.10.011
97. Aveldano MI. Phospholipid species containing long and very long polyenoic fatty acids remain with rhodopsin after hexane extraction of photoreceptor membranes. *Biochemistry.* 1988;27(4):1229-1239. doi:10.1021/bi00404a024
98. Roe CR, Roe DS, Wallace M, Garritson B. Choice of oils for essential fat supplements can enhance production of abnormal metabolites in fat oxidation disorders. *Mol Genet Metab.* 2007;92(4):346-350. doi:10.1016/j.ymgme.2007.07.012
99. Barabas P, Liu A, Xing W, et al. Role of ELOVL4 and very long-chain polyunsaturated fatty acids in mouse models of Stargardt type 3 retinal degeneration. *Proc Natl Acad Sci.* 2013;110(13):5181-5186. doi:10.1073/pnas.1214707110
100. Logan S, Agbaga M-P, Chan MD, et al. Deciphering mutant ELOVL4 activity in autosomal-dominant Stargardt macular dystrophy. *Proc Natl Acad Sci.* 2013;110(14):5446-5451. doi:10.1073/pnas.1217251110
101. Logan S, Anderson RE. Dominant Stargardt Macular Dystrophy (STGD3) and ELOVL4. In: *Medicine.* Vol 664. ; 2014:447-453. doi:10.1007/978-1-4614-3209-8_57
102. Olszewska A, Szewczyk A. Mitochondria as a pharmacological target: Magnum overview. *IUBMB Life.* 2013;65(3):273-281. doi:10.1002/iub.1147
103. Newman NJ. Treatment of hereditary optic neuropathies. *Nat Rev Neurol.* 2012;8(10):545-556. doi:10.1038/nrneurol.2012.167
104. González-Barroso MM, Anedda A, Gallardo-Vara E, Redondo-Horcajo M, Rodríguez-Sánchez L, Rial E. Fatty acids revert the inhibition of respiration caused by the antidiabetic drug metformin to facilitate their mitochondrial β -oxidation. *Biochim Biophys Acta - Bioenerg.* 2012;1817(10):1768-1775. doi:10.1016/j.bbabi.2012.02.019
105. Parikh S, Saneto R, Falk MJ, Anselm I, Cohen BH, Haas R. A Modern Approach to the Treatment of Mitochondrial Disease Opinion statement. *Curr Treat Options Neurol.* 2009;11(6):414-430. doi:10.1038/nmeth.2250.Digestion
106. Giordano L, Deceglie S, D'Adamo P, et al. Cigarette toxicity triggers Leber's hereditary optic neuropathy by affecting mtDNA copy number, oxidative phosphorylation and ROS detoxification pathways. *Cell Death Dis.* 2015;6(12):e2021. doi:10.1038/cddis.2015.364
107. Ascensão A, Lumini-Oliveira J, Oliveira PJ, Magalhães J. Mitochondria as a target for exercise-induced cardioprotection. *Curr Drug Targets.* 2011;12(6):860-871.
108. Bishop DJ, Granata C, Eynon N. Can we optimise the exercise training prescription to maximise improvements in mitochondria function and content? *Biochim Biophys Acta.* 2014;1840(4):1266-

1275. doi:10.1016/j.bbagen.2013.10.012
109. Bhatti JS, Bhatti GK, Reddy PH. Mitochondrial dysfunction and oxidative stress in metabolic disorders - A step towards mitochondria based therapeutic strategies. *Biochim Biophys Acta*. 2016;1863(5):1066-1077. doi:10.1016/j.bbadis.2016.11.010
110. Qiu X, Brown K, Hirschey MD, Verdin E, Chen D. Calorie Restriction Reduces Oxidative Stress by SIRT3-Mediated SOD2 Activation. *Cell Metab*. 2010;12(6):662-667. doi:10.1016/j.cmet.2010.11.015
111. Bough KJ, Wetherington J, Hassel B, et al. Mitochondrial biogenesis in the anticonvulsant mechanism of the ketogenic diet. *Ann Neurol*. 2006;60(2):223-235. doi:10.1002/ana.20899
112. Kang H-C, Lee Y-M, Kim HD, Lee JS, Slama A. Safe and Effective Use of the Ketogenic Diet in Children with Epilepsy and Mitochondrial Respiratory Chain Complex Defects. *Epilepsia*. 2007;48(1). doi:10.1111/j.1528-1167.2006.00906.x
113. Garrido-Maraver J, Cordero MD, Oropesa-Ávila M, et al. Coenzyme Q10 therapy. *Mol Syndromol*. 2014;5(3-4):187-197. doi:10.1159/000360101
114. Quinzii CM, López LC, Von-Moltke J, et al. Respiratory chain dysfunction and oxidative stress correlate with severity of primary CoQ 10 deficiency. *FASEB J*. 2008;22(6):1874-1885. doi:10.1096/fj.07-100149
115. Lulli M, Witort E, Papucci L, et al. Coenzyme Q10 protects retinal cells from apoptosis induced by radiation in vitro and in vivo. *J Radiat Res*. 2012;53(5):695-703. doi:10.1093/jrr/rrs025
116. Knott A, Achterberg V, Smuda C, et al. Topical treatment with coenzyme Q10-containing formulas improves skin's Q10 level and provides antioxidative effects. *BioFactors*. 2015;41(6):383-390. doi:10.1002/biof.1239
117. Mencucci R, Favuzza E, Boccalini C, et al. CoQ10-containing eye drops prevent UVB-induced cornea cell damage and increase cornea wound healing by preserving mitochondrial function. *Investig Ophthalmol Vis Sci*. 2014;55(11):7266-7271. doi:10.1167/iovs.14-15306
118. Yue Y, Zhou H, Liu G, Li Y, Yan Z, Duan M. The advantages of a novel CoQ10 delivery system in skin photo-protection. *Int J Pharm*. 2010;392(1-2):57-63. doi:10.1016/j.ijpharm.2010.03.032
119. Powell RD, Swet JH, Kennedy KL, et al. MitoQ modulates oxidative stress and decreases inflammation following hemorrhage. *J Trauma Acute Care Surg*. 2015;78(3):573-579. doi:10.1097/TA.0000000000000533
120. Demyanenko IA, Popova EN, Zakharova V V., et al. Mitochondria-targeted antioxidant SkQ1 improves impaired dermal wound healing in old mice. *Aging (Albany NY)*. 2015;7(7):475-485. doi:10.18632/aging.100772
121. R Hamblin M. Mechanisms and applications of the anti-inflammatory effects of photobiomodulation. *AIMS Biophys*. 2017;4(3):337-361. doi:10.3934/biophys.2017.3.337

122. De Freitas LF, Hamblin MR. Proposed Mechanisms of Photobiomodulation or Low-Level Light Therapy. *IEEE J Sel Top Quantum Electron*. 2016;22(3):348-364. doi:10.1109/JSTQE.2016.2561201
123. Albarracin R, Eells J, Valter K. Photobiomodulation protects the retina from light-induced photoreceptor degeneration. *Investig Ophthalmol Vis Sci*. 2011;52(6):3582-3592. doi:10.1167/iovs.10-6664
124. Chow RT, Armati PJ. Photobiomodulation: Implications for Anesthesia and Pain Relief. *Photomed Laser Surg*. 2016;34(12):599-609. doi:10.1089/pho.2015.4048
125. Mao Z, Wu JH, Dong T, Wu MX. Additive enhancement of wound healing in diabetic mice by low level light and topical CoQ10. *Sci Rep*. 2016;6(February):1-8. doi:10.1038/srep20084
126. Mignon C, Botchkareva N V., Uzunbajakava NE, Tobin DJ. Photobiomodulation devices for hair regrowth and wound healing: a therapy full of promise but a literature full of confusion. *Exp Dermatol*. 2016;25(10):745-749. doi:10.1111/exd.13035
127. Lanzafame RJ, Stadler I, Kurtz AF, et al. Reciprocity of exposure time and irradiance on energy density during photoradiation on wound healing in a murine pressure ulcer model. *Lasers Surg Med*. 2007;39(6):534-542. doi:10.1002/lsm.20519
128. Wong-Riley MTTT, Liang HL, Eells JT, et al. Photobiomodulation directly benefits primary neurons functionally inactivated by toxins: Role of cytochrome c oxidase. *J Biol Chem*. 2005;280(6):4761-4771. doi:10.1074/jbc.M409650200
129. Eells JT, Henry MM, Summerfelt P, et al. Therapeutic photobiomodulation for methanol-induced retinal toxicity. *Proc Natl Acad Sci U S A*. 2003;100(6):3439-3444. doi:10.1073/pnas.0534746100
130. Rojas JC, Lee J, John JM, Gonzalez-Lima F. Neuroprotective Effects of Near-Infrared Light in an In Vivo Model of Mitochondrial Optic Neuropathy. *J Neurosci*. 2008;28(50):13511-13521. doi:10.1523/JNEUROSCI.3457-08.2008
131. Smith AM, Mancini MC, Nie S. Second window for in vivo imaging. *Nat Nanotechnol*. 2009;4(11):710-711. doi:10.1038/nnano.2009.326
132. Mester E, Spiry T, Szende B, Tota JG. Effect of laser rays on wound healing. *Am J Surg*. 1971;122(4):532-535. doi:10.1016/0002-9610(71)90482-X
133. Passarella S, Casamassima E, Molinari S, et al. Increase of proton electrochemical potential and ATP synthesis in rat liver mitochondria irradiated in vitro by helium-neon laser. *FEBS Lett*. 1984;175(1):95-99.
134. Karu TI. Special issue papers. photobiological fundamentals of low-power laser therapy. *IEEE J Quantum Electron*. 1987;23(10):1703-1717. doi:10.1109/JQE.1987.1073236
135. Belyanovich LM, Nikol'skaya VP, Rudenok AN, Konev S V. Spectral characteristics of cyanide-inhibited cytochrome oxidase under photoactivation and in interaction with ATP. *J Appl Spectrosc*. 1996;63(3):323-329. doi:10.1007/BF02606593

136. Yu W, Naim JO, McGowan M, Ippolito K, Lanzafame RJ. Photomodulation of Oxidative Metabolism and Electron Chain Enzymes in Rat Liver Mitochondria. *Photochem Photobiol.* 1997;66(6):866-871. doi:10.1111/j.1751-1097.1997.tb03239.x
137. Srinivasan S, Avadhani NG. Cytochrome c oxidase dysfunction in oxidative stress. *Free Radic Biol Med.* 2012;53(6):1252-1263. doi:10.1016/j.freeradbiomed.2012.07.021
138. Karu TII, Kolyakov SFF. Exact action spectra for cellular responses relevant to phototherapy. *Photomed Laser Surg.* 2005;23(4):355-361. doi:10.1089/pho.2005.23.355
139. Sarti P, Arese M, Bacchi A, et al. Nitric Oxide and Mitochondrial Complex IV. *IUBMB Life.* 2003;55(10-11):605-611. doi:10.1080/15216540310001628726
140. Chen AC-H, Arany PR, Huang Y-Y, et al. Low-level laser therapy activates NF-kB via generation of reactive oxygen species in mouse embryonic fibroblasts. *PLoS One.* 2011;6(7):e22453. doi:10.1371/journal.pone.0022453
141. Michael BP, Thomas ES, Chris H, Glen J. Improving mitochondrial function protects bumblebees from neonicotinoid pesticides. *PLoS One.* 2016;11(11):1-11. doi:10.1371/journal.pone.0166531
142. Sun H, Feng Z. Neuroprotective role of ATP-sensitive potassium channels in cerebral ischemia. *Acta Pharmacol Sin.* 2013;34(1):24-32. doi:10.1038/aps.2012.138
143. Jere SW, Abrahamse H, Houreld NN. The JAK/STAT signaling pathway and photobiomodulation in chronic wound healing. *Cytokine Growth Factor Rev.* 2017;38(September):73-79. doi:10.1016/j.cytogfr.2017.10.001
144. Curra M, Pellicoli ACA, Filho NAKNAK, et al. Photobiomodulation reduces oral mucositis by modulating NF-kB. *J Biomed Opt.* 2015;20(12):125008. doi:10.1117/1.JBO.20.12.125008
145. Jere SW, Houreld NN, Abrahamse H. Photobiomodulation at 660 nm stimulates proliferation and migration of diabetic wounded cells via the expression of epidermal growth factor and the JAK/STAT pathway. *J Photochem Photobiol B Biol.* 2018;179(October 2017):74-83. doi:10.1016/j.jphotobiol.2017.12.026
146. Karu TI. Multiple roles of cytochrome c oxidase in mammalian cells under action of red and IR-A radiation. *IUBMB Life.* 2010;62(8):607-610. doi:10.1002/iub.359
147. Song S, Zhang Y, Fong C-C, Tsang C-H, Yang Z, Yang M. cDNA Microarray Analysis of Gene Expression Profiles in Human Fibroblast Cells Irradiated with Red Light. *J Invest Dermatol.* 2003;120(5):849-857. doi:10.1046/j.1523-1747.2003.12133.x
148. Hennessy M, Hamblin MR. Photobiomodulation and the brain: a new paradigm. *J Opt.* 2017;19(1):013003. doi:10.1088/2040-8986/19/1/013003
149. Ivandic BT, Ivandic T. Effects of Photobiomodulation Therapy on Patients with Primary Open Angle Glaucoma: A Pilot Study. *Photomed Laser Surg.* December 2015;pho.2015.3944. doi:10.1089/pho.2015.3944

150. Tang J, Herda AA, Kern TS. Photobiomodulation in the treatment of patients with non-center-involving diabetic macular oedema. *Br J Ophthalmol*. 2014;98(8):1013-1015. doi:10.1136/bjophthalmol-2013-304477
151. Merry GF, Munk MR, Dotson RS, Walker MG, Devenyi RG. Photobiomodulation reduces drusen volume and improves visual acuity and contrast sensitivity in dry age-related macular degeneration. *Acta Ophthalmol*. 2016;95(4):e270-e277. doi:10.1111/aos.13354
152. Harwerth RS, Sperling HG. Effects of intense visible radiation on the increment-threshold spectral sensitivity of the rhesus monkey eye. *Vision Res*. 1975;15(11):1193-1204. doi:10.1016/0042-6989(75)90162-5
153. Liang HL, Whelan HT, Eells JT, Wong-Riley MTT. Near-infrared light via light-emitting diode treatment is therapeutic against rotenone- and 1-methyl-4-phenylpyridinium ion-induced neurotoxicity. *Neuroscience*. 2008;153(4):963-974. doi:10.1016/j.neuroscience.2008.03.042
154. Qu C, Cao W, Fan Y, Lin Y. Near-Infrared Light Protect the Photoreceptor from Light-Induced Damage in Rats. In: ; 2010:365-374. doi:10.1007/978-1-4419-1399-9_42
155. Albarracin R, Valter K. 670 nm red light preconditioning supports Müller cell function: Evidence from the white light-induced damage model in the rat retina. *Photochem Photobiol*. 2012;88(6):1418-1427. doi:10.1111/j.1751-1097.2012.01130.x
156. Albarracin R, Natoli R, Rutar M, Valter K, Provis J. 670 nm light mitigates oxygen-induced degeneration in C57BL/6J mouse retina. *BMC Neurosci*. 2013;14(1):125. doi:10.1186/1471-2202-14-125
157. Tang J, Du Y, Lee CA, Talahalli R, Eells JT, Kern TS. Low-Intensity Far-Red Light Inhibits Early Lesions That Contribute to Diabetic Retinopathy: In Vivo and In Vitro. *Investig Ophthalmology Vis Sci*. 2013;54(5):3681. doi:10.1167/iovs.12-11018
158. Saliba A, Du Y, Liu H, et al. Photobiomodulation mitigates diabetes-induced retinopathy by direct and indirect mechanisms: Evidence from intervention studies in pigmented mice. *PLoS One*. 2015;10(10):1-14. doi:10.1371/journal.pone.0139003
159. Lu Y-Z, Fernando N, Natoli R, Madigan M, Valter K. 670nm light treatment following retinal injury modulates Müller cell gliosis: Evidence from in vivo and in vitro stress models. *Exp Eye Res*. 2018;169(November 2017):1-12. doi:10.1016/j.exer.2018.01.011
160. Sivapathasuntharam C, Sivaprasad S, Hogg C, Jeffery G. Aging retinal function is improved by near infrared light (670 nm) that is associated with corrected mitochondrial decline. *Neurobiol Aging*. 2017;52:66-70. doi:10.1016/j.neurobiolaging.2017.01.001
161. Rutar M, Natoli R, Albarracin R, Valter K, Provis J. 670-Nm Light Treatment Reduces Complement Propagation Following Retinal Degeneration. *J Neuroinflammation*. 2012;9(1):1. doi:10.1186/1742-2094-9-257
162. Calaza KC, Kam JH, Hogg C, Jeffery G. Mitochondrial decline precedes phenotype development in the complement factor H mouse model of retinal degeneration but can be corrected by near

- infrared light. *Neurobiol Aging*. 2015;36(10):2869-2876. doi:10.1016/j.neurobiolaging.2015.06.010
163. Fuma S, Murase H, Kuse Y, Tsuruma K, Shimazawa M, Hara H. Photobiomodulation with 670 nm light increased phagocytosis in human retinal pigment epithelial cells. *Mol Vis*. 2015;21(August):883-892. <http://www.ncbi.nlm.nih.gov/pubmed/26321863><http://www.pubmedcentral.nih.gov/articlerender.fcgi?artid=PMC4544713>.
164. Cheng Y, Du Y, Liu H, Tang J, Veenstra A, Kern TS. Photobiomodulation Inhibits Long-term Structural and Functional Lesions of Diabetic Retinopathy. *Diabetes*. 2018;67(2):291-298. doi:10.2337/db17-0803
165. Herman WH, Zimmet P. Type 2 Diabetes: An Epidemic Requiring Global Attention and Urgent Action. *Diabetes Care*. 2012;35(5):943-944. doi:10.2337/dc12-0298
166. Zhang W, Liu H, Al-Shabrawey M, Caldwell RW, Caldwell RB. Inflammation and diabetic retinal microvascular complications. *J Cardiovasc Dis Res*. 2011;2(2):96-103. doi:10.4103/0975-3583.83035
167. Stitt AW, Curtis TM, Chen M, et al. The progress in understanding and treatment of diabetic retinopathy. *Prog Retin Eye Res*. 2016;51:156-186. doi:10.1016/j.preteyeres.2015.08.001
168. Moran EP, Wang Z, Chen J, Sapieha P, Smith LEH, Ma J-X. Neurovascular cross talk in diabetic retinopathy: Pathophysiological roles and therapeutic implications. *Am J Physiol - Hear Circ Physiol*. 2016;311(3):H738-H749. doi:10.1152/ajpheart.00005.2016
169. Tonade D, Liu H, Kern TS. Photoreceptor Cells Produce Inflammatory Mediators That Contribute to Endothelial Cell Death in Diabetes. *Investig Ophthalmology Vis Sci*. 2016;57(10):4264. doi:10.1167/iovs.16-19859
170. Okawa H, Sampath AP, Laughlin SB, Fain GL. ATP Consumption by Mammalian Rod Photoreceptors in Darkness and in Light. *Curr Biol*. 2008;18(24):1917-1921. doi:10.1016/j.cub.2008.10.029
171. Prunty MC, Aung MH, Hanif AM, et al. In Vivo Imaging of Retinal Oxidative Stress Using a Reactive Oxygen Species-Activated Fluorescent Probe. *Investig Ophthalmology Vis Sci*. 2015;56(10):5862. doi:10.1167/iovs.15-16810
172. Rueda EM, Johnson JE, Giddabasappa A, et al. The cellular and compartmental profile of mouse retinal glycolysis, tricarboxylic acid cycle, oxidative phosphorylation, and ~P transferring kinases. *Mol Vis*. 2016;22(July):847-885. <http://www.ncbi.nlm.nih.gov/pubmed/27499608>.
173. Ramos D, Carretero A, Navarro M, et al. Mimicking Microvascular Alterations of Human Diabetic Retinopathy: A Challenge for the Mouse Models. *Curr Med Chem*. 2013;20(26):3200-3217. doi:10.2174/09298673113209990028
174. Cai X, McGinnis JF. Diabetic Retinopathy: Animal Models, Therapies, and Perspectives. *J Diabetes Res*. 2016;2016. doi:10.1155/2016/3789217

175. Chaabo F, Pronczuk A, Maslova E, Hayes KCK. Nutritional correlates and dynamics of diabetes in the Nile rat (*Arvicanthis niloticus*): a novel model for diet-induced type 2 diabetes and the metabolic syndrome. *Nutr Metab (Lond)*. 2010;7(1):29. doi:10.1186/1743-7075-7-29
176. Noda K, Nakao S, Zandi S, Sun D, Hayes KC, Hafezi-Moghadam A. Retinopathy in a novel model of metabolic syndrome and type 2 diabetes: new insight on the inflammatory paradigm. *FASEB J*. 2014;28(5):2038-2046. doi:10.1096/fj.12-215715
177. Saïdi T, Mbarek S, Chaouacha-Chekir R Ben, Hicks D. Diurnal rodents as animal models of human central vision: characterisation of the retina of the sand rat *Psammomys obsesus*. *Graefes Arch Clin Exp Ophthalmol*. 2011;249(7):1029-1037. doi:10.1007/s00417-011-1641-9
178. Cheung CY, Ikram MK, Klein R, Wong TY. The clinical implications of recent studies on the structure and function of the retinal microvasculature in diabetes. *Diabetologia*. 2015;58(5):871-885. doi:10.1007/s00125-015-3511-1
179. Hajmoussa G, Elorza AA, Nies VJM, Jensen EL, Nagy RA, Harmsen MC. Hyperglycemia Induces Bioenergetic Changes in Adipose-Derived Stromal Cells While Their Pericytic Function Is Retained. *Stem Cells Dev*. 2016;25(19):1444-1453. doi:10.1089/scd.2016.0025
180. Patti M-E, Corvera S. The Role of Mitochondria in the Pathogenesis of Type 2 Diabetes. *Endocr Rev*. 2010;31(3):364-395. doi:10.1210/er.2009-0027
181. Sivitz WI, Yorek MA. Mitochondrial Dysfunction in Diabetes: From Molecular Mechanisms to Functional Significance and Therapeutic Opportunities. *Antioxid Redox Signal*. 2010;12(4):537-577. doi:10.1089/ars.2009.2531
182. Montgomery MK, Turner N. Mitochondrial dysfunction and insulin resistance: an update. *Endocr Connect*. 2015;4(1):R1-R15. doi:10.1530/EC-14-0092
183. Saudek CD, Herman WH, Sacks DB, Bergenstal RM, Edelman D, Davidson MB. A New Look at Screening and Diagnosing Diabetes Mellitus. *J Clin Endocrinol Metab*. 2008;93(7):2447-2453. doi:10.1210/jc.2007-2174
184. Dietrich N, Hammes H-P. Retinal Digest Preparation: A Method to Study Diabetic Retinopathy. In: *Animal Models in Diabetes Research*. Totowa, NJ: Humana Press; 2012:291-302. doi:10.1007/978-1-62703-068-7_19
185. Kuznetsov A V., Schneeberger S, Seiler R, et al. Mitochondrial defects and heterogeneous cytochrome c release after cardiac cold ischemia and reperfusion. *Am J Physiol Circ Physiol*. 2004;286(5):H1633-H1641. doi:10.1152/ajpheart.00701.2003
186. Kuznetsov A V., Strobl D, Ruttman E, Königsrainer A, Margreiter R, Gnaiger E. Evaluation of Mitochondrial Respiratory Function in Small Biopsies of Liver. *Anal Biochem*. 2002;305(2):186-194. doi:10.1006/abio.2002.5658
187. Kooragayala K, Gotoh N, Cogliati T, et al. Quantification of Oxygen Consumption in Retina Ex Vivo Demonstrates Limited Reserve Capacity of Photoreceptor Mitochondria. *Investig Ophthalmology Vis Sci*. 2015;56(13):8428. doi:10.1167/iovs.15-17901

188. Metea MR, Newman EA. Signalling within the neurovascular unit in the mammalian retina. *Exp Physiol*. 2007;92(4):635-640. doi:10.1113/expphysiol.2006.036376
189. Lott MEJ, Slocomb JE, Shivkumar V, et al. Comparison of retinal vasodilator and constrictor responses in type 2 diabetes. *Acta Ophthalmol*. 2012;90(6):e434-e441. doi:10.1111/j.1755-3768.2012.02445.x
190. Fort PE, Losiewicz MK, Pennathur S, et al. mTORC1-Independent Reduction of Retinal Protein Synthesis in Type 1 Diabetes. *Diabetes*. 2014;63(9):3077-3090. doi:10.2337/db14-0235
191. Harrison WW, Bearnse MA, Ng JS, et al. Multifocal Electroretinograms Predict Onset of Diabetic Retinopathy in Adult Patients with Diabetes. *Investig Ophthalmology Vis Sci*. 2011;52(2):772. doi:10.1167/iovs.10-5931
192. Gardner TW, Abcouwer SF, Losiewicz MK, Fort PE. Phosphatase control of 4E-BP1 phosphorylation state is central for glycolytic regulation of retinal protein synthesis. *Am J Physiol Metab*. 2015;309(6):E546-E556. doi:10.1152/ajpendo.00180.2015
193. Piano I, Novelli E, Della Santina L, Strettoi E, Cervetto L, Gargini C. Involvement of Autophagic Pathway in the Progression of Retinal Degeneration in a Mouse Model of Diabetes. *Front Cell Neurosci*. 2016;10. doi:10.3389/fncel.2016.00042
194. Barber AJ, Gardner TW, Abcouwer SF. The Significance of Vascular and Neural Apoptosis to the Pathology of Diabetic Retinopathy. *Investig Ophthalmology Vis Sci*. 2011;52(2):1156. doi:10.1167/iovs.10-6293
195. Toleikis A, Trumbeckaite S, Majiene D. Cytochrome c Effect on Respiration of Heart Mitochondria: Influence of Various Factors. *Biosci Rep*. 2005;25(5-6):387-397. doi:10.1007/s10540-005-2897-2
196. Lemieux H, Blier PU, Tardif J-C. Does membrane fatty acid composition modulate mitochondrial functions and their thermal sensitivities? *Comp Biochem Physiol Part A Mol Integr Physiol*. 2008;149(1):20-29. doi:10.1016/j.cbpa.2007.09.015
197. Sullivan EM, Fix A, Crouch MJ, et al. Murine diet-induced obesity remodels cardiac and liver mitochondrial phospholipid acyl chains with differential effects on respiratory enzyme activity. *J Nutr Biochem*. 2017;45:94-103. doi:10.1016/j.jnutbio.2017.04.004
198. Hoeks J, de Wilde J, Hulshof MFM, et al. High Fat Diet-Induced Changes in Mouse Muscle Mitochondrial Phospholipids Do Not Impair Mitochondrial Respiration Despite Insulin Resistance. Shirihai OS, ed. *PLoS One*. 2011;6(11):e27274. doi:10.1371/journal.pone.0027274
199. Kowluru RA, Mishra M, Kowluru A, Kumar B. Hyperlipidemia and the development of diabetic retinopathy: Comparison between type 1 and type 2 animal models. *Metabolism*. 2016;65(10):1570-1581. doi:10.1016/j.metabol.2016.07.012
200. Murrow BA, Hoehn KL. Mitochondrial regulation of insulin action. *Int J Biochem Cell Biol*. 2010;42(12):1936-1939. doi:10.1016/j.biocel.2010.08.020

201. Gupte AA, Minze LJ, Reyes M, et al. High-Fat Feeding-Induced Hyperinsulinemia Increases Cardiac Glucose Uptake and Mitochondrial Function Despite Peripheral Insulin Resistance. *Endocrinology*. 2013;154(8):2650-2662. doi:10.1210/en.2012-2272
202. Lou P-H, Lucchinetti E, Scott KY, et al. Alterations in fatty acid metabolism and sirtuin signaling characterize early type-2 diabetic hearts of fructose-fed rats. *Physiol Rep*. 2017;5(16):e13388. doi:10.14814/phy2.13388
203. Brand MD. The sites and topology of mitochondrial superoxide production. *Exp Gerontol*. 2010;45(7-8):466-472. doi:10.1016/j.exger.2010.01.003
204. Radad K, Rausch WD, Gille G. Rotenone induces cell death in primary dopaminergic culture by increasing ROS production and inhibiting mitochondrial respiration. *Neurochem Int*. 2006;49(4):379-386. doi:10.1016/j.neuint.2006.02.003
205. Raha S, Robinson BH. Mitochondria, oxygen free radicals, disease and ageing. *Trends Biochem Sci*. 2000;25(10):502-508. <http://www.ncbi.nlm.nih.gov/pubmed/11050436>.
206. Pitkanen S, Robinson BH. Mitochondrial complex I deficiency leads to increased production of superoxide radicals and induction of superoxide dismutase. *J Clin Invest*. 1996;98(2):345-351. doi:10.1172/JCI118798
207. Lesnefsky EJ, Chen Q, Hoppel CL. Mitochondrial Metabolism in Aging Heart. *Circ Res*. 2016;118(10):1593-1611. doi:10.1161/CIRCRESAHA.116.307505
208. Rosca MG, Lemieux H, Hoppel CL. Mitochondria in the elderly: Is acetylcarnitine a rejuvenator? ☆. *Adv Drug Deliv Rev*. 2009;61(14):1332-1342. doi:10.1016/j.addr.2009.06.009
209. Lamoke F, Shaw S, Yuan J, et al. Increased oxidative and nitrative stress accelerates aging of the retinal vasculature in the diabetic retina. *PLoS One*. 2015;10(10):1-19. doi:10.1371/journal.pone.0139664
210. Osorio-Paz I, Uribe-Carvajal S, Salceda R. In the early stages of diabetes, rat retinal mitochondria undergo mild uncoupling due to UCP2 activity. *PLoS One*. 2015;10(5):1-15. doi:10.1371/journal.pone.0122727
211. Pescosolido N, Barbato A, Stefanucci A, Buomprisco G. Role of Electrophysiology in the Early Diagnosis and Follow-Up of Diabetic Retinopathy. *J Diabetes Res*. 2015;2015:1-8. doi:10.1155/2015/319692
212. Shirao Y, Kawasaki K. Electrical responses from diabetic retina. *Prog Retin Eye Res*. 1998;17(1):59-76. doi:10.1016/S1350-9462(97)00005-0
213. Kizawa J, Machida S, Kobayashi T, Gotoh Y, Kurosaka D. Changes of Oscillatory Potentials and Photopic Negative Response in Patients with Early Diabetic Retinopathy. *Jpn J Ophthalmol*. 2006;50(4):367-373. doi:10.1007/s10384-006-0326-0
214. Rajagopal R, Bligard GW, Zhang S, Yin L, Lukasiewicz P, Semenkovich CF. Functional Deficits Precede Structural Lesions in Mice With High-Fat Diet-Induced Diabetic Retinopathy. *Diabetes*.

- 2016;65(4):1072-1084. doi:10.2337/db15-1255
215. Layton CJ, Safa R, Osborne NN. Oscillatory potentials and the b-Wave: Partial masking and interdependence in dark adaptation and diabetes in the rat. *Graefe's Arch Clin Exp Ophthalmol*. 2007;245(9):1335-1345. doi:10.1007/s00417-006-0506-0
216. Szél Á, Röhlich P. Two cone types of rat retina detected by anti-visual pigment antibodies. *Exp Eye Res*. 1992;55(1):47-52. doi:10.1016/0014-4835(92)90090-F
217. Szél Á, Röhlich P, Gaffé AR, Juliusson B, Aguirre G, Van Veen T. Unique topographic separation of two spectral classes of cones in the mouse retina. *J Comp Neurol*. 1992;325(3):327-342. doi:10.1002/cne.903250302
218. Petit-Jacques J, Völgyi B, Rudy B, Bloomfield S. Spontaneous Oscillatory Activity of Starburst Amacrine Cells in the Mouse Retina. *J Neurophysiol*. 2005;94(3):1770-1780. doi:10.1152/jn.00279.2005
219. Gastinger MJ, Singh RSJ, Barber AJ. Loss of Cholinergic and Dopaminergic Amacrine Cells in Streptozotocin-Diabetic Rat and Ins2 Akita -Diabetic Mouse Retinas. *Investig Ophthalmology Vis Sci*. 2006;47(7):3143. doi:10.1167/iovs.05-1376
220. Ottlecz A, Garcia CA, Eichberg J, Fox DA. Alterations in retinal Na⁺, K⁺-ATPase in diabetes: streptozotocin-induced and Zucker diabetic fatty rats. *Curr Eye Res*. 1993;12(12):1111-1121. doi:10.3109/02713689309033509
221. Park S-H, Park J-W, Park S-J, et al. Apoptotic death of photoreceptors in the streptozotocin-induced diabetic rat retina. *Diabetologia*. 2003;46(9):1260-1268. doi:10.1007/s00125-003-1177-6
222. Harris MI, Klein R, Welborn TA, Knudman MW. Onset of NIDDM occurs at Least 4-7 yr Before Clinical Diagnosis. *Diabetes Care*. 1992;15(7):815-819. doi:10.2337/diacare.15.7.815
223. Li L, Wan X, Zhao G. Meta-analysis of the risk of cataract in type 2 diabetes. *BMC Ophthalmol*. 2014;14(1):94. doi:10.1186/1471-2415-14-94
224. Pfister F, Feng Y, vom Hagen F, et al. Pericyte Migration: A Novel Mechanism of Pericyte Loss in Experimental Diabetic Retinopathy. *Diabetes*. 2008;57(9):2495-2502. doi:10.2337/db08-0325
225. Park SW, Yun J-H, Kim JH, Kim K-W, Cho C-H, Kim JH. Angiopoietin 2 Induces Pericyte Apoptosis via $\alpha_3\beta_1$ Integrin Signaling in Diabetic Retinopathy. *Diabetes*. 2014;63(9):3057-3068. doi:10.2337/db13-1942
226. Zhang L, Li Y, Payne J, et al. Presence of retinal pericyte-reactive autoantibodies in diabetic retinopathy patients. *Sci Rep*. 2016;6(1):20341. doi:10.1038/srep20341
227. Cogan DG, Kuwabara T. The Mural Cell in Perspective. *Arch Ophthalmol*. 1967;78(2):133-139. doi:10.1001/archophth.1967.00980030135005
228. Tilton RG, Miller EJ, Kilo C, Williamson JR. Pericyte form and distribution in rat retinal and uveal capillaries. *Invest Ophthalmol Vis Sci*. 1985;26(1):68-73.

<http://www.ncbi.nlm.nih.gov/pubmed/3967956>.

229. Bianchi E, Ripandelli G, Taurone S, et al. Age and diabetes related changes of the retinal capillaries: An ultrastructural and immunohistochemical study. *Int J Immunopathol Pharmacol*. 2016;29(1):40-53. doi:10.1177/0394632015615592
230. Warmke N, Griffin KJ, Cubbon RM. Pericytes in diabetes-associated vascular disease. *J Diabetes Complications*. 2016;30(8):1643-1650. doi:10.1016/j.jdiacomp.2016.08.005
231. Agbaga M-P, Brush RS, Mandal MNA, Henry K, Elliott MH, Anderson RE. Role of Stargardt-3 macular dystrophy protein (ELOVL4) in the biosynthesis of very long chain fatty acids. *Proc Natl Acad Sci U S A*. 2008;105(35):12843-12848. doi:10.1073/pnas.0802607105
232. Grayson C, Molday RS. Dominant Negative Mechanism Underlies Autosomal Dominant Stargardt-like Macular Dystrophy Linked to Mutations in ELOVL4. *J Biol Chem*. 2005;280(37):32521-32530. doi:10.1074/jbc.M503411200
233. Kuny S, Gaillard F, Sauvé Y. Differential gene expression in eyecup and retina of a mouse model of stargardt-like macular dystrophy (STGD3). *Investig Ophthalmol Vis Sci*. 2012;53(2):664-675. doi:10.1167/iovs.11-8418
234. Bennett LD, Brush RS, Chan M, et al. Effect of Reduced Retinal VLC-PUFA on Rod and Cone Photoreceptors. *Investig Ophthalmology Vis Sci*. 2014;55(5):3150. doi:10.1167/iovs.14-13995
235. Agbaga M-P, Tam BM, Wong JS, Yang LL, Anderson RE, Moritz OL. Mutant ELOVL4 That Causes Autosomal Dominant Stargardt-3 Macular Dystrophy Is Misrouted to Rod Outer Segment Disks. *Investig Ophthalmology Vis Sci*. 2014;55(6):3669. doi:10.1167/iovs.13-13099
236. Kuny S, Cho WJ, Dimopoulos IS, et al. Early onset ultrastructural and functional defects in RPE and photoreceptors of a stargardt-like macular dystrophy (STGD3) transgenic mouse model. *Investig Ophthalmol Vis Sci*. 2015;56(12):7109-7121. doi:10.1167/iovs.15-17567
237. Sparrow JR, Gregory-Roberts E, Yamamoto K, et al. The bisretinoids of retinal pigment epithelium. *Prog Retin Eye Res*. 2012;31(2):121-135. doi:10.1016/j.preteyeres.2011.12.001
238. Krock BL, Bilotta J, Perkins BD. Noncell-autonomous photoreceptor degeneration in a zebrafish model of choroideremia. *Proc Natl Acad Sci*. 2007;104(11):4600-4605. doi:10.1073/pnas.0605818104
239. Young RW, Bok D. Participation of the retinal pigment epithelium in the rod outer segment renewal process. *J Cell Biol*. 1969;42(2):392-403. <http://www.ncbi.nlm.nih.gov/pubmed/5792328>.
240. Duncan JL, LaVail MM, Yasumura D, et al. An RCS-Like Retinal Dystrophy Phenotype in Mer Knockout Mice. *Investig Ophthalmology Vis Sci*. 2003;44(2):826. doi:10.1167/iovs.02-0438
241. Picard E, Houssier M, Bujold K, et al. CD36 plays an important role in the clearance of oxLDL and associated age-dependent sub-retinal deposits. *Aging (Albany NY)*. 2010;2(12):981-989. doi:10.18632/aging.100218

242. Zhang D, Brankov M, Makhija MT, et al. Correlation between Inactive Cathepsin D Expression and Retinal Changes in *mcd2 / mcd2* Transgenic Mice. *Investig Ophthalmology Vis Sci*. 2005;46(9):3031. doi:10.1167/iovs.04-1510
243. Zigler JS, Zhang C, Grebe R, et al. Mutation in the A3/A1-crystallin gene impairs phagosome degradation in the retinal pigmented epithelium of the rat. *J Cell Sci*. 2011;124(4):523-531. doi:10.1242/jcs.078790
244. Kinnunen K, Petrovski G, Moe MC, Berta A, Kaarniranta K. Molecular mechanisms of retinal pigment epithelium damage and development of age-related macular degeneration. *Acta Ophthalmol*. 2012;90(4):299-309. doi:10.1111/j.1755-3768.2011.02179.x
245. Wong WL, Su X, Li X, et al. Global prevalence of age-related macular degeneration and disease burden projection for 2020 and 2040: a systematic review and meta-analysis. *Lancet Glob Heal*. 2014;2(2):e106-e116. doi:10.1016/S2214-109X(13)70145-1
246. Kuny S, Gaillard F, Mema SC, et al. Inner Retina Remodeling in a Mouse Model of Stargardt-like Macular Dystrophy (STGD3). *Investig Ophthalmology Vis Sci*. 2010;51(4):2248. doi:10.1167/iovs.09-4718
247. Karan G, Lillo C, Yang Z, et al. Lipofuscin accumulation, abnormal electrophysiology, and photoreceptor degeneration in mutant ELOVL4 transgenic mice: A model for macular degeneration. *Proc Natl Acad Sci*. 2005;102(11):4164-4169. doi:10.1073/pnas.0407698102
248. Samuel W, Jaworski C, Postnikova OA, et al. Appropriately differentiated ARPE-19 cells regain phenotype and gene expression profiles similar to those of native RPE cells. *Mol Vis*. 2017;23:60-89. <http://www.ncbi.nlm.nih.gov/pubmed/28356702>.
249. Mao Y, Finnemann SC. Analysis of Photoreceptor Outer Segment Phagocytosis by RPE Cells in Culture. In: ; 2012:285-295. doi:10.1007/978-1-62703-080-9_20
250. Mazzoni F, Safa H, Finnemann SC. Understanding photoreceptor outer segment phagocytosis: Use and utility of RPE cells in culture. *Exp Eye Res*. 2014;126(1-2):51-60. doi:10.1016/j.exer.2014.01.010
251. Tsang SH. Role for the Target Enzyme in Deactivation of Photoreceptor G Protein in Vivo. *Science (80-)*. 1998;282(5386):117-121. doi:10.1126/science.282.5386.117
252. Mao Y, Finnemann SC. Live Imaging of LysoTracker-Labelled Phagolysosomes Tracks Diurnal Phagocytosis of Photoreceptor Outer Segment Fragments in Rat RPE Tissue Ex Vivo. In: ; 2016:717-723. doi:10.1007/978-3-319-17121-0_95
253. Wei H, Xun Z, Granado H, Wu A, Handa JT. An easy, rapid method to isolate RPE cell protein from the mouse eye. *Exp Eye Res*. 2016;145:450-455. doi:10.1016/j.exer.2015.09.015
254. Sardiello M, Palmieri M, di Ronza A, et al. A Gene Network Regulating Lysosomal Biogenesis and Function. *Science (80-)*. June 2009. doi:10.1126/science.1174447
255. Settembre C, Zoncu R, Medina DL, et al. A lysosome-to-nucleus signalling mechanism senses and

- regulates the lysosome via mTOR and TFEB. *EMBO J.* 2012;31(5):1095-1108. doi:10.1038/emboj.2012.32
256. Settembre C, Di Malta C, Polito VA, et al. TFEB Links Autophagy to Lysosomal Biogenesis. *Science (80-)*. 2011;332(6036):1429-1433. doi:10.1126/science.1204592
257. Tian J, Ishibashi K, Ishibashi K, et al. Advanced glycation endproduct-induced aging of the retinal pigment epithelium and choroid: A comprehensive transcriptional response. *Proc Natl Acad Sci.* 2005;102(33):11846-11851. doi:10.1073/pnas.0504759102
258. Yaung J, Jin M, Barron E, et al. alpha-Crystallin distribution in retinal pigment epithelium and effect of gene knockouts on sensitivity to oxidative stress. *Mol Vis.* 2007;13:566-577. <http://www.ncbi.nlm.nih.gov/pubmed/17438522>.
259. Crabb JW, Miyagi M, Gu X, et al. Drusen proteome analysis: An approach to the etiology of age-related macular degeneration. *Proc Natl Acad Sci.* 2002;99(23):14682-14687. doi:10.1073/pnas.222551899
260. Gnaiger E, Lassnig B, Kuznetsov A, Rieger G, Margreiter R. Mitochondrial oxygen affinity, respiratory flux control and excess capacity of cytochrome c oxidase. *J Exp Biol.* 1998;201(Pt 8):1129-1139. <http://www.ncbi.nlm.nih.gov/pubmed/9510525>.
261. Langmann T. Microglia activation in retinal degeneration. *J Leukoc Biol.* 2007;81(6):1345-1351. doi:10.1189/jlb.0207114
262. Sethna S, Chamakkala T, Gu X, et al. Regulation of Phagolysosomal Digestion by Caveolin-1 of the Retinal Pigment Epithelium Is Essential for Vision. *J Biol Chem.* 2016;291(12):6494-6506. doi:10.1074/jbc.M115.687004
263. Mata NL, Tzekov RT, Liu X, Weng J, Birch DG, Travis GH. Delayed dark-adaptation and lipofuscin accumulation in *abcr*^{+/-} mice: Implications for involvement of ABCR in age-related macular degeneration. *Investig Ophthalmol Vis Sci.* 2001;42(8):1685-1690.
264. BERGMANN M, SCHÜTT F, HOLZ FG, KOPITZ J. Inhibition of the ATP-driven proton pump in RPE lysosomes by the major lipofuscin fluorophore A2-E may contribute to the pathogenesis of age-related macular degeneration. *FASEB J.* 2004;18(3):562-564. doi:10.1096/fj.03-0289fje
265. Vasireddy V, Jablonski MM, Khan NW, et al. *Elovl4* 5-bp deletion knock-in mouse model for Stargardt-like macular degeneration demonstrates accumulation of ELOVL4 and lipofuscin. *Exp Eye Res.* 2009;89(6):905-912. doi:10.1016/j.exer.2009.07.021
266. Shang P, Valapala M, Grebe R, et al. The amino acid transporter SLC36A4 regulates the amino acid pool in retinal pigmented epithelial cells and mediates the mechanistic target of rapamycin, complex 1 signaling. *Aging Cell.* 2017;16(2):349-359. doi:10.1111/acel.12561
267. Fort PE, Lampi KJ. New focus on alpha-crystallins in retinal neurodegenerative diseases. *Exp Eye Res.* 2011;92(2):98-103. doi:10.1016/j.exer.2010.11.008
268. Joly S, Francke M, Ulbricht E, et al. Cooperative Phagocytes. *Am J Pathol.* 2009;174(6):2310-

2323. doi:10.2353/ajpath.2009.090023
269. Xu H, Chen M, Forrester J V. Para-inflammation in the aging retina. *Prog Retin Eye Res.* 2009;28(5):348-368. doi:10.1016/j.preteyeres.2009.06.001
270. Ma W, Zhao L, Fontainhas AM, Fariss RN, Wong WT. Microglia in the Mouse Retina Alter the Structure and Function of Retinal Pigmented Epithelial Cells: A Potential Cellular Interaction Relevant to AMD. Koch K-W, ed. *PLoS One.* 2009;4(11):e7945. doi:10.1371/journal.pone.0007945
271. Kohno H, Chen Y, Kevany BM, et al. Photoreceptor Proteins Initiate Microglial Activation via Toll-like Receptor 4 in Retinal Degeneration Mediated by All- trans -retinal. *J Biol Chem.* 2013;288(21):15326-15341. doi:10.1074/jbc.M112.448712
272. Golpich M, Amini E, Mohamed Z, Azman Ali R, Mohamed Ibrahim N, Ahmadiani A. Mitochondrial Dysfunction and Biogenesis in Neurodegenerative diseases: Pathogenesis and Treatment. *CNS Neurosci Ther.* 2017;23(1):5-22. doi:10.1111/cns.12655
273. Feher J, Kovacs I, Artico M, et al. Mitochondrial alterations of retinal pigment epithelium in age-related macular degeneration. *Neurobiol Aging.* 2006;27(7):983-993. doi:10.1016/j.neurobiolaging.2005.05.012
274. Reyes-Reveles J, Dhingra A, Alexander D, Bragin A, Philp NJ, Boesze-Battaglia K. Phagocytosis-dependent ketogenesis in retinal pigment epithelium. *J Biol Chem.* 2017;292(19):8038-8047. doi:10.1074/jbc.M116.770784
275. Di Pierdomenico J, García-Ayuso D, Pinilla I, et al. Early Events in Retinal Degeneration Caused by Rhodopsin Mutation or Pigment Epithelium Malfunction: Differences and Similarities. *Front Neuroanat.* 2017;11(March):14. doi:10.3389/fnana.2017.00014
276. Pastore D, Greco M, Passarella S. Specific helium-neon laser sensitivity of the purified cytochrome c oxidase. *Int J Radiat Biol.* 2000;76(6):863-870. doi:10902741
277. Karu T, Technology L. Mitochondrial Signaling in Mammalian Cells Activated by Red and Near-IR Radiation. 2015;1988(December):1091-1099. doi:10.1111/j.1751-1097.2008.00394.x
278. Gkotsi D, Begum R, Salt T, et al. Recharging mitochondrial batteries in old eyes. Near infra-red increases ATP. *Exp Eye Res.* 2014;122(March):50-53. doi:10.1016/j.exer.2014.02.023
279. Begum R, Calaza K, Kam JH, et al. Near-infrared light increases ATP , extends lifespan and improves mobility in aged Drosophila melanogaster. *Biol Lett.* 2015:25-28. doi:10.1098/rsbl.2015.0073
280. Vos M, Lovisa B, Geens A, et al. Near-infrared 808 nm light boosts complex IV-dependent respiration and rescues a Parkinson-related pink1 model. *PLoS One.* 2013;8(11):1-9. doi:10.1371/journal.pone.0078562
281. Spittler R, Ho H, Norpetlian F, et al. Combination of low level light therapy and nitrosyl-cobinamide accelerates wound healing. *J Biomed Opt.* 2015;20(5):051022.

doi:10.1117/1.JBO.20.5.051022

282. Buravlev EA, Zhidkova T V., Osipov AN, Vladimirov YA. Are the mitochondrial respiratory complexes blocked by NO the targets for the laser and LED therapy? *Lasers Med Sci.* 2014;30(1):173-180. doi:10.1007/s10103-014-1639-8
283. Wigle JC, Castellanos CC. In vitro measurements of oxygen consumption rates in hTERT-RPE cells exposed to low levels of red light. In: Hamblin MR, Carroll JD, Arany P, eds. Vol 9695. ; 2016:96950A. doi:10.1117/12.2210738
284. Anilkumar N, Weber R, Zhang M, Brewer A, Shah AM. Nox4 and Nox2 NADPH Oxidases Mediate Distinct Cellular Redox Signaling Responses to Agonist Stimulation. *Arterioscler Thromb Vasc Biol.* 2008;28(7):1347-1354. doi:10.1161/ATVBAHA.108.164277
285. Gnaiger E. Polarographic Oxygen Sensors, the Oxygraph, and High-Resolution Respirometry to Assess Mitochondrial Function. In: *Drug-Induced Mitochondrial Dysfunction.* Hoboken, NJ, USA: John Wiley & Sons, Inc.; :325-352. doi:10.1002/9780470372531.ch12
286. Moriyama Y, Nguyen J, Akens M, Moriyama EH, Lilje L. In vivo effects of low level laser therapy on inducible nitric oxide synthase. *Lasers Surg Med.* 2009;41(3):227-231. doi:10.1002/lsm.20745
287. Amaroli A, Benedicenti A, Ferrando S, et al. Photobiomodulation by Infrared Diode Laser: Effects on Intracellular Calcium Concentration and Nitric Oxide Production of *Paramecium*. *Photochem Photobiol.* 2016;92(6):854-862. doi:10.1111/php.12644
288. Keszler A, Brandal G, Baumgardt S, et al. Far red/near infrared light-induced protection against cardiac ischemia and reperfusion injury remains intact under diabetic conditions and is independent of nitric oxide synthase. *Front Physiol.* 2014;5 AUG(August):1-7. doi:10.3389/fphys.2014.00305
289. Rizzi M, Migliario M, Tonello S, Rocchetti V, Renò F. Photobiomodulation induces in vitro re-epithelialization via nitric oxide production. *Lasers Med Sci.* 2018. doi:10.1007/s10103-018-2443-7
290. Shiva S, Gladwin MT. Shining a light on tissue NO stores: Near infrared release of NO from nitrite and nitrosylated hemes. *J Mol Cell Cardiol.* 2009;46(1):1-3. doi:10.1016/j.yjmcc.2008.10.005
291. Sarkar S, Korolchuk VI, Renna M, et al. Complex Inhibitory Effects of Nitric Oxide on Autophagy. *Mol Cell.* 2011;43(1):19-32. doi:10.1016/j.molcel.2011.04.029
292. Kiang JG, Krishnan S, Lu X, Li Y. Inhibition of Inducible Nitric-Oxide Synthase Protects Human T Cells from Hypoxia-Induced Apoptosis. *Mol Pharmacol.* 2007;73(3):738-747. doi:10.1124/mol.107.041079
293. Rodriguez-Melendez R, Zempleni J. Nitric Oxide Signaling Depends on Biotin in Jurkat Human Lymphoma Cells. *J Nutr.* 2009;139(3):429-433. doi:10.3945/jn.108.101840

294. Gnaiger E, Steinlechner R, Mendez G, Eberl T, Margreiter R. Control of Mitochondrial Respiration By Oxygen. *J Bioenerg Biomembr.* 1995;27(6):583-596.
295. Wagner BA, Venkataraman S, Buettner GR. The rate of oxygen utilization by cells. *Free Radic Biol Med.* 2011;51(3):700-712. doi:10.1016/j.freeradbiomed.2011.05.024
296. Emmerson A, Trevelin SC, Mongue-Din H, et al. Nox2 in regulatory T cells promotes angiotensin II-induced cardiovascular remodeling. *J Clin Invest.* 2018;128(7):3088-3101. doi:10.1172/JCI97490
297. Jiang F, Roberts SJ, Datla S r., Dusting GJ. NO Modulates NADPH Oxidase Function Via Heme Oxygenase-1 in Human Endothelial Cells. *Hypertension.* 2006;48(5):950-957. doi:10.1161/01.HYP.0000242336.58387.1f
298. Cringle SJ, Yu DY, Yu PK, Su EN. Intraretinal oxygen consumption in the rat in vivo. *Investig Ophthalmol Vis Sci.* 2002;43(6):1922-1927.
299. Medrano CJ, Fox DA. Oxygen consumption in the rat outer and inner retina: Light- and pharmacologically-induced inhibition. *Exp Eye Res.* 1995;61(3):273-284. doi:10.1016/S0014-4835(05)80122-8
300. Rohrer B, Bandyopadhyay M, Beeson C. Reduced Metabolic Capacity in Aged Primary Retinal Pigment Epithelium (RPE) is Correlated with Increased Susceptibility to Oxidative Stress. In: Bowes Rickman C, LaVail MM, Anderson RE, Grimm C, Hollyfield J, Ash J, eds. Vol 854. *Advances in Experimental Medicine and Biology.* Cham: Springer International Publishing; 2016:793-798. doi:10.1007/978-3-319-17121-0_106
301. Fernández-Vizorra E, Enríquez JA, Pérez-Martos A, Montoya J, Fernández-Silva P. Tissue-specific differences in mitochondrial activity and biogenesis. *Mitochondrion.* 2011;11(1):207-213. doi:10.1016/j.mito.2010.09.011
302. Hollander JM, Thapa D, Shepherd DL. Physiological and structural differences in spatially distinct subpopulations of cardiac mitochondria: influence of cardiac pathologies. *AJP Hear Circ Physiol.* 2014;307(1):H1-H14. doi:10.1152/ajpheart.00747.2013
303. Kann O, Kovacs R. Mitochondria and neuronal activity. *AJP Cell Physiol.* 2006;292(2):C641-C657. doi:10.1152/ajpcell.00222.2006
304. Amirpour N, Karamali F, Razavi S, Esfandiari E, Nasr-Esfahani M. A proper protocol for isolation of retinal pigment epithelium from rabbit eyes. *Adv Biomed Res.* 2014;3(1):4. doi:10.4103/2277-9175.124630
305. Speijer D. How the mitochondrion was shaped by radical differences in substrates: What carnitine shuttles and uncoupling tell us about mitochondrial evolution in response to ROS Insights & Perspectives D. Speijer. *BioEssays.* 2014;36(7):634-643. doi:10.1002/bies.201400033
306. Speijer D. Oxygen radicals shaping evolution: Why fatty acid catabolism leads to peroxisomes while neurons do without it: FADH2/NADH flux ratios determining mitochondrial radical formation were crucial for the eukaryotic invention of peroxisomes and catabolic tissue. *BioEssays.*

- 2011;33(2):88-94. doi:10.1002/bies.201000097
307. Santos JM, Mohammad G, Zhong Q, Kowluru RA. Diabetic retinopathy, superoxide damage and antioxidants. *Curr Pharm Biotechnol*. 2011;12(3):352-361. doi:10.2174/138920111794480507
 308. Zorov DB, Juhaszova M, Sollott SJ. Mitochondrial Reactive Oxygen Species (ROS) and ROS-Induced ROS Release. *Physiol Rev*. 2014;94(3):909-950. doi:10.1152/physrev.00026.2013
 309. del Olmo-Aguado S, Núñez-Álvarez C, Osborne NN, Núñez-Álvarez C, Osborne NN. Red light of the visual spectrum attenuates cell death in culture and retinal ganglion cell death in situ. *Acta Ophthalmol*. 2016;94(6):e481-e491. doi:10.1111/aos.12996
 310. Sukumar P, Viswambharan H, Imrie H, et al. Nox2 NADPH Oxidase Has a Critical Role in Insulin Resistance-Related Endothelial Cell Dysfunction. *Diabetes*. 2013;62(6):2130-2134. doi:10.2337/db12-1294
 311. Mima A, Qi W, Hiraoka-Yamamoto J, et al. Retinal not systemic oxidative and inflammatory stress correlated with VEGF expression in rodent models of insulin resistance and diabetes. *Investig Ophthalmol Vis Sci*. 2012;53(13):8424-8432. doi:10.1167/iovs.12-10207
 312. Koulis C, Watson AMD, Gray SP, Jandeleit-Dahm KA. Linking RAGE and Nox in diabetic micro- and macrovascular complications. *Diabetes Metab*. 2015;41(4):272-281. doi:10.1016/j.diabet.2015.01.006
 313. De Cristóbal J, Cárdenas A, Lizasoain I, et al. Inhibition of glutamate release via recovery of ATP levels accounts for a neuroprotective effect of aspirin in rat cortical neurons exposed to oxygen-glucose deprivation. *Stroke*. 2002;33(1):261-267. doi:10.1161/hs0102.101299
 314. Browne SE. When too much ATP is a bad thing: A pivotal role for P2X7 receptors in motor neuron degeneration. *J Neurochem*. 2013;126(3):301-304. doi:10.1111/jnc.12321
 315. Masuch A, Shieh CH, van Rooijen N, van Calker D, Biber K. Mechanism of microglia neuroprotection: Involvement of P2X7, TNF α , and valproic acid. *Glia*. 2016;64(1):76-89. doi:10.1002/glia.22904
 316. Arabian M, Aboutaleb N, Soleimani M, Ajami M, Habibey R, Pazoki-Toroudi H. Activation of mitochondrial KATP channels mediates neuroprotection induced by chronic morphine preconditioning in hippocampal CA-1 neurons following cerebral ischemia. *Adv Med Sci*. 2018;63(2):213-219. doi:10.1016/j.advms.2017.11.003
 317. Lin Y-F, Raab-Graham K, Jan YN, Jan LY. NO stimulation of ATP-sensitive potassium channels: Involvement of Ras/mitogen-activated protein kinase pathway and contribution to neuroprotection. *Proc Natl Acad Sci U S A*. 2004;101(20):7799-7804. doi:10.1073/pnas.0402496101
 318. Zhong F, Li Y, Mi X. Photobiomodulation on KATP Channels of Kir6.2-Transfected HEK-293 Cells. *Int J Photoenergy*. 2014;2014:1-7. doi:10.1155/2014/898752
 319. Ettaiche M, Heurteaux C, Blondeau N, Borsotto M, Tinel N, Lazdunski M. ATP-sensitive potassium channels (KATP) in retina: A key role for delayed ischemic tolerance. *Brain Res*.

2001;890(1):118-129. doi:10.1016/S0006-8993(00)03152-8

320. Kevany BBM, Palczewski K. Phagocytosis of retinal rod and cone photoreceptors. *Physiology (Bethesda)*. 2010;25(1):8-15. doi:10.1152/physiol.00038.2009.Phagocytosis
321. Krumschnabel G, Fontana-Ayoub M, Sumbalova Z, et al. Simultaneous High-Resolution Measurement of Mitochondrial Respiration and Hydrogen Peroxide Production. In: ; 2015:245-261. doi:10.1007/978-1-4939-2257-4_22